SCUOLA DI DOTTORATO
UNIVERSITÀ DEGLI STUDI DI MILANO-BICOCCA

Department of Biotechnology & Biosciences

PhD program in Biology and Biotechnology, Cycle XXXI

Curriculum in Synthetic and Systems Biology

Targeting cancer cell metabolism: Gateway towards personalized medicine

Surname: **BHARAT** Name: **ROHIT**

Registration number: **811103**

Tutor: **Prof. Marco Vanoni**

Supervisor: **Prof. Lilia Alberghina**

Coordinator: **Prof. Paola Branduardi**

ACADEMIC YEAR: 2017/2018

“Nothing in life is to be feared,
it is only to be understood.
Now is the time to understand more,
so that we may fear less.”

Marie Curie

ABSTRACT

In the recent decade, one of the important keynote message derived through the summation of our global efforts against cancer is the need to better understand cancer cell metabolism for the development of better and efficacious personalized therapy. Cancer cells undertake a multifaceted rewiring of metabolic pathways in order to support their proliferative and invasive nature, which requires a systems level investigation to fully comprehend the scale of metabolic deregulation.

In this study, we systematically investigated the metabolic differences using untargeted metabolomics and ^{13}C flux omics approach in oncogenic K-Ras driven tumours. We tested the effects of drug inhibitors targeting glucose and glutamine metabolism to unravel the alternative metabolic pathways required for cancer cell survival.

We further expanded our research towards understanding the role of cellular metabolism in driving resistance to endocrine therapeutic drugs in ERα positive breast cancer. We identified specific metabolic mechanisms of utilization of glutamine in resistant cells while also providing further basis for the use of metformin as an adjuvant in the treatment of endocrine therapy-resistant cancers.

Finally, we contributed to current understanding about cancer cell metabolism by exploring the role of glutamine beyond its role as a carbon and nitrogen source in driving growth and proliferation of cancer cells. Upon substitution of glutamine with appropriate

nitrogen and carbon sources, cancer cells exhibited reverse Warburg phenotype.

The findings from this thesis open up new avenues of research through the identification of new putative targets and bring us one step closer towards designing much better and efficacious therapeutic strategy for the treatment of cancer patients.

RIASSUNTO

Nell'ultimo decennio, uno dei messaggi chiave derivante dalle ricerche scientifiche sul cancro è la necessità di comprendere meglio il metabolismo delle cellule tumorali per lo sviluppo di una terapia personalizzata migliore e più efficace. Le cellule tumorali attuano un riarrangiamento metabolico che coinvolge diversi processi per supportare la loro natura proliferativa ed invasiva.

Per meglio comprendere l'entità del cambiamento metabolico, in questo studio abbiamo utilizzato un approccio *systems level* impiegando la metabolomica *untargeted* e la flussomica mediante isotopi stabili del carbonio (13C) in cellule tumorali esprimenti un K-Ras oncogenico.

Abbiamo testato gli effetti di farmaci inibitori del metabolismo di glucosio e glutammina per indagare eventuali vie metaboliche alternative attivate per la sopravvivenza delle cellule tumorali. Inoltre abbiamo investigato il ruolo del metabolismo cellulare nello sviluppo della resistenza alla terapia endocrina nel carcinoma mammario ERα positivo. I dati ottenuti hanno permesso di identificare specifici meccanismi metabolici di utilizzo della glutammina in cellule resistenti alla terapia, suggerendo l'utilizzo del farmaco metformina come adiuvante nel trattamento dei tumori resistenti alla terapia ormonale.

Infine, abbiamo contribuito alla comprensione del metabolismo delle cellule tumorali nel guidare la crescita e la proliferazione, esplorando il ruolo della glutammina oltre la nota funzione di fonte di carbonio e azoto; infatti sostituendo la glutammina con fonti

alternative di carbonio e azoto, si osserva un fenotipo *reverse Warburg.*

I risultati di questa tesi aprono strade di ricerca per l'identificazione di nuovi potenziali obiettivi terapeutici e ci portano verso la progettazione di una strategia terapeutica migliore e più efficace per il trattamento dei pazienti oncologici.

ABBREVIATIONS

AcCoA	acetyl-CoA
ACLY	ATP citrate lyase
Akg	alpha-ketoglutarate
AMP	adenosine mono phosphate
ATP	adenosine tri phosphate
CBM	constraint based modelling
DCA	dichloroacetate
DNA	deoxyribose nucleic acid
DNMTs	DNA methyl transferases
EMU	elementary metabolite unit
ETC	electron transport chain
FADH2	reduced flavin adenine dinucleotide
FBA	flux balance analysis
GC-MS	gas chromatography-mass spectrometry
GSMMs	fenome scale metabolic models
H2O2	hydrogen Peroxide
HAT	histone acetyl transferases
HMTs	histone methyl transferases
JHDMs	jumonji-C domain-containing HDMs
JMJC	jumonji-C
KAT	lysine acetyltransferases
LC-MS	liquid chromatography-mass spectrometry
MALDI	matrix assisted laser desorption ionisation.
MFA	metabolic flux analysis
MS	mass spectrometer
MYC	v-myc avian myelocytomatosis viral oncogene homolog
NADH	reduced Nicotinamide adenine dinucleotide
NMR	nuclear magnetic resonance
OCR	oxygen consumption rate
OXPHOS	oxidative phosphorylation
PDC	pyruvate decarboxylase
PET	positron emission tomography
PPP	pentose phosphate pathway
PRMT5	protein arginine N-methyltransferase 5
ROS	reactive oxygen species
SAM	s-adenosyl-methionine
TCA	tri carboxylic acid

Table of Contents

1. INTRODUCTION

1.1 CANCER

Cancer can be described as a highly complex systems disease that defies univocal definition, and one of the major obstacle in our efforts to defeat cancer has been largely due to the confusions surrounding the origin of the disease, where much of the misperception arises from an absence of a unifying theory. Absence of a clear idea about origin of cancer makes it difficult to formulate an effective and clear strategy for the prevention and management of the disease, where paradoxes and contradictions add to its ever increasing complexity (Baker and Kramer, 2007; Gibbs, 2003; Hanahan and Weinberg, 2000; Soto and Sonnenschein, 2004). Even after decades of research, this failure to clearly define the origin of disease is reflected by the consistently increasing number of cancer cases, now making cancer the second leading cause of death worldwide.

For a long time cancer has been considered as a genetic disease where damage to a cell's DNA was blamed for the transformation of a normal cell into potentially dreadful cancer cell. Discovery of oncogenes like MYC (Duesberg et al., 1977), *PI3K* (Chang, 1997), RAS (Shih et al., 1979), *ERBB* (Bister and Duesberg, 1979; Lai et al., 1979) and tumour suppressor genes like *TP53* (LANE and CRAWFORD, 1979) and *RB* (Knudson, 1971) inspired a wealth of research towards finding gene targets that could potentially drive transformation of cancer cells. These findings of innumerable number of gene changes in different cancers has led to idea that cancer is not a single disease but a collection of different diseases (Vogelstein and Kinzler, 1993), bringing forth

the notion that cancer treatment will require personalized drug therapies (Fojo and Parkinson, 2010; Rosell et al., 2009).

Riding in the wave of somatic mutation theory of cancer for over half a century, massive genome projects have been carried out in possibly all forms of cancer with an aim not only to identify gene defects that could serve as targets for treatment of cancer but also to gain a deeper understanding about the cause of the disease. But recently, increasing number of researchers have challenged the somatic mutation theory of cancer and consequently, questioning whether the data generated from these sequencing projects would likely ever provide any definite cure for the disease (Baker and Kramer, 2007; Fojo and Parkinson, 2010; Sonnenschein and Soto, 2000; Soto and Sonnenschein, 2004).

Considering the fact that mutations in cancers arise sporadically, and mutations in cells within the same tumours drastically differ from each other, (Loeb et al., 2003) let alone between different forms of cancer (Jones et al., 2015), further backs up the arguments made against somatic mutation theory, as not all the cells of the tumour would carry the same mutation for treatment to be 100% effective. Increasing number of evidence suggests that a lot of the mutations in cancer arise due to downstream epiphenomenon (Shackleton et al., 2009), hence, these gene defects may take part in the progression of the disease, but not necessarily be the cause of the disease.

Even though a large genetic heterogeneity exists among more than 100 types of cancer, Hanahan and Weinberg described six fundamental traits that were common and required by almost all

forms of cancer for their growth and survival, which today we know as the hallmarks of cancer. (Hanahan and Weinberg, 2000). This revolutionary review lead to a universal acceptance of cancer as a multifactorial disease, overtaking the somatic mutation theory, and has guided cancer research for the past decade. One widely recognized addition to cancer hallmarks recently has been the concept of metabolic reprogramming (Hanahan and Weinberg, 2000; de Mas et al., 2014) (Figure 1.1).

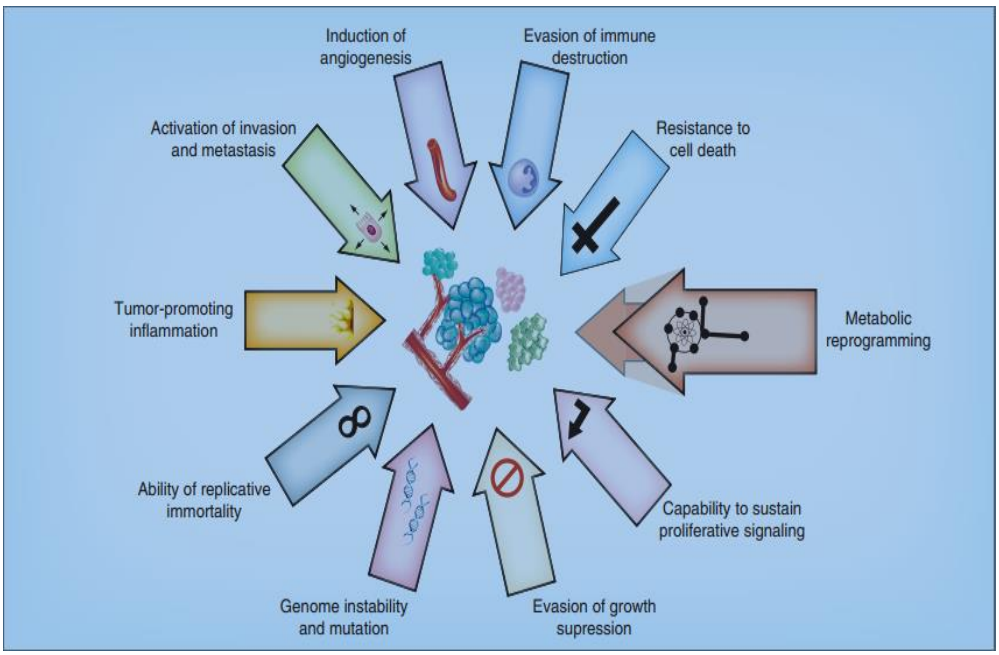

Figure 1.1 : Hallmarks of Cancer. Capabilities required by cancer cells to become tumorigenic and eventually malignant which include Evasion of growth suppression, genome instability and mutation, ability to replicate continuously, tumour promoting inflammation, ability to invade and metastize, induce angiogenesis, and ability to evade immune recognition. Metabolic reprogramming has been identified as an emerging hallmark and a promising target for treatment of cancer cells and devise new therapeutic approaches. (Adapted from (de Mas et al., 2014))

1.2 CANCER METABOLIC THEORY-THE FORGOTTEN GOSPEL

Much before the dawn of somatic mutation theory postulated by Theodor Boveri in 1914 that combination of chromosomal defects could cause cancer (Doonan et al., 2012), investigation and diagnosis of medical conditions were performed by evaluation of external phenotypical traits as well as assessment of biological fluids accessible from the patients such as urine, blood etc. First such report on different traces in urine samples of cancer patients was published by Johannes Muller in 1838 (Müller, 1838) following which metabolic traits of cancer began to play a role in determining treatment regimen for cancer patients.

One of the earliest hypothesis about deregulated respiration required by cancer cells was put forward by August von Wasserman, and he set out to show treating animal models with inhibitors of mitochondrial metabolism like selenium-eosin could reduce the growth of tumours (Wassermann et al., 1911). Human trials of this compound were discontinued after patients showed high selenium toxicity.

Few years later, German biochemist Otto Warburg went on to embark on his pioneering work towards systemic investigation of cell metabolism in several animal models and postulated his hypothesis which today we know as the Warburg effect (Warburg et al., 1924). Warburg observed presence of glucose and oxygen and increased production of lactic acid in liver carcinoma cells of rats and formulated his theory that cancer cells undergo aerobic glycolysis to ferment glucose into lactate in presence of high levels

of oxygen. His work was further validated by Cori and Cori in an *in vivo* setting (Cori and G.T.Cori, 1925).

This hypothesis has become the basis for tumour imaging in modern medicine using labelled glucose analogues via PET scan (Figure 1.2).

Figure 1.2: Whole body PET scan of a 68 year old man showing excessive skeletal metastasis and radioactive uptake of ^{18}F-FDG into multiple bone lesions. Adapted from (Iagaru et al., 2009)

Though other researchers alongside Otto Warburg, showed importance of cellular metabolism in cancer by treating children with acute lymphoblastic leukaemia via targeting nucleotide metabolism (FARBER et al., 1947), the era of cellular biochemistry in conjunction to cancer research was soon overshadowed by discovery of DNA as genetic & transferable material (Avery, 1944; Hershey, 1952), followed by discovery of molecular structure of DNA (Watson, J. D., & Crick, 1953) which guided cancer research for coming half a century and became the rationale for the massive genome projects.

Even though the key focus of researchers shifted from metabolism towards investigation of the genome, identification of mutations in many metabolic genes capable of driving tumour development kept shocking the field (Baysal, 2000; Tomlinson et al., 2002). It was surprising to note that though no specific gene mutation or genetic abnormality was common to all forms of cancer (Loeb, 2001; Nowell, 2002; Vitucci et al., 2011), nearly all forms of cancer showed similar deregulated glucose metabolism regardless of their tissue of origin (Seyfried et al., 2014). Even the founders of DNA structures asked researchers to pay special attention to cancer cell metabolism (Almac and Ince, 2007).

Now nearly after two decades of research, there has been a renewed interest in understanding cellular metabolism as nearly all cancer associated genetic mutations have been shown to alter metabolic pathways to support tumorigenesis (Boroughs and DeBerardinis, 2015; Cantor and Sabatini, 2012; Ward and

Thompson, 2012). Today a detailed understanding of metabolic reorganization in cancer stands crucial for formulating appropriate and effective therapy for treatment and management of the disease.

1.3 REWIRED METABOLIC PATHWAYS IN CANCER

Warburg argued that only the cells which have the capability to increase glycolysis followed by a damage to cellular respiration have the ability to form cancer (Warburg, 1956). This increased glycolysis allowed cells to maintain energy homeostasis required for their survival as a compensatory mechanism to its respiratory damage. In recent years scientists have identified many other alterations of metabolic pathways and expanded Warburg's concept to include energy derived from TCA cycle, amino acids, nucleotide metabolism, and fatty acid oxidation (Figure 1.3), some of which are explained below.

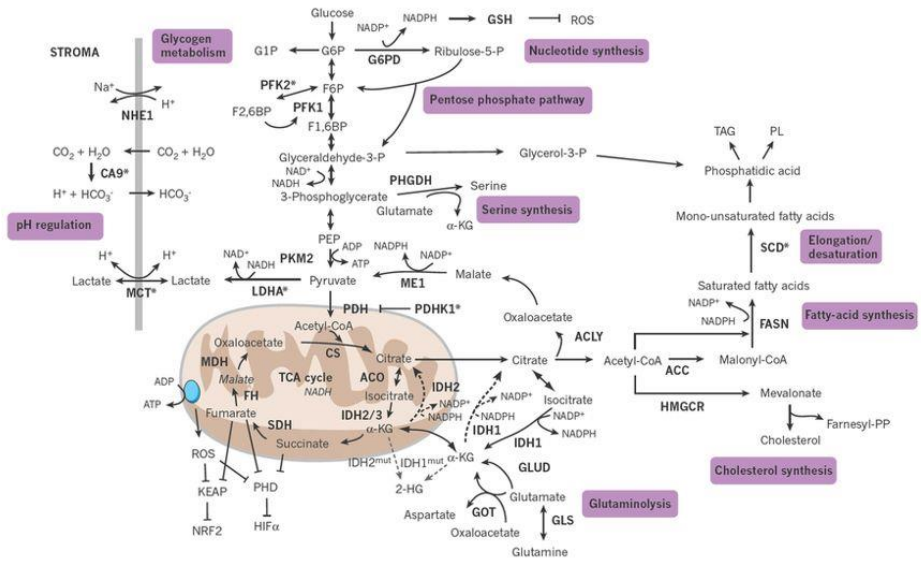

Figure 1.3: Overview of rewired metabolic pathways in cancer. The main metabolic pathways which contribute for macromolecule production as well as cellular bioenergetics to maintain sustained proliferation in cancer cells are glycolysis, TCA

cycle, pentose phosphate pathway, nucleotide synthesis, cholesterol synthesis, glutaminolysis and fatty-acid synthesis. Adapted from (Schulze and Harris, 2012)

1.3.1 Deregulated nutrient uptake

In order to maintain the energy balance and fulfil biosynthetic demands, cancer cells have to increase their import of nutrients from the environment. Among the most abundant energy sources, glucose and glutamine play the most prominent role in supporting anabolic growth. In addition, oxidation of glucose and glutamine allows generation of NADH and FADH2 which mediate the transfer of electrons in ETC to aid ATP generation.

Increased glucose consumption has been a paramount feature of cancer cells which now is being exploited as a valuable tool for detection of tumours via PET imaging.

Many cancer mutations in the signalling cascade like *PI3K*/*Akt*, *mTOR*, *PTEN* etc. have been shown to alter the activity of glucose transporters (*GLUT1*) and can be inhibited by interfering with signalling cascade (Benz et al., 2011; Makinoshima et al., 2015). Another oncogenic influence on glucose consumption is mediated by *RAS* by upregulating *GLUT1* mRNA expression as well as influencing various other metabolic pathways (Figure 1.4).

Similar to glucose, glutamine also plays a crucial role in supporting anabolic demands of cancer cells and increased glutamine uptake is now being seen as an important feature in cancer (Wise and Thompson, 2010). It has been shown that cancer cells can maintain TCA cycle by replenishing TCA cycle intermediates by a process called as anaplerosis, and glutamine is an important anaplerotic source for many proliferating cells.

Oncogenic activation of signalling pathways mediated by c-*Myc* have been shown to upregulated glutamine uptake by increased expression of glutamine transporter *ASCT2* and *SN2* as well as activation of other enzymes of glutamine metabolism (Gao et al., 2009; Mannava et al., 2008).

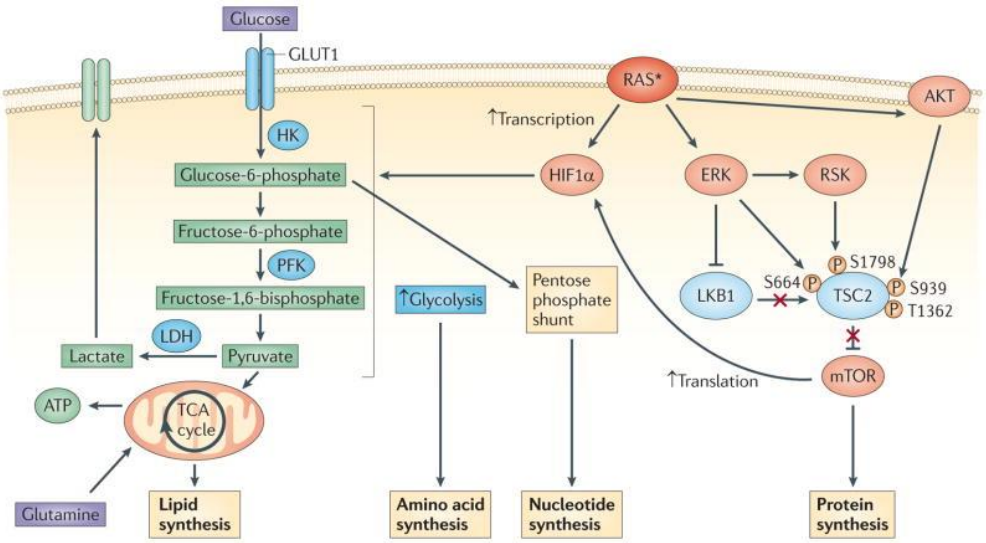

Figure 1.4: RAS effects on cell metabolism: metabolic effects of RAS on glucose uptake are mostly mediated by *HIF-1α*, either directly or via activation of *PI3K/Akt* or converging with *mTOR* activation. This activation leads to increased glycolysis and hence increased glucose uptake by upregulation of *GLUT1* activity (Pylayeva-Gupta et al., 2011).

Targeting glucose and glutamine transporters has shown to suppress tumour growth and resentitize resistant tumours to therapy (Lai et al., 2014; Wang et al., 2015).

1.3.2 Rewired Glucose metabolism and Pentose Phosphate Pathway

Glycolytic pathway helps normal cells convert the up taken mole of glucose into two moles of pyruvate resulting in a net gain of two moles of ATP and two moles of NADH. In a well oxygenated tissue this pyruvate enters mitochondria and gets completely oxidized to CO_2 via TCA cycle generating about 36 moles of ATP. As mentioned earlier as Warburg effect, cancer cells metabolize the consumed glucose into lactate as the end product instead of pyruvate to further derive energy via TCA cycle. Even though energetically inefficient, increased glycolysis allows cancer cells to potentially exceed the total cellular ATP produced via glycolysis than that can be produced by the slower oxidative phosphorylation (GUPPY et al., 1993). Another explanation for higher glycolytic rates could be because it helps cancer cells to synthesise metabolic intermediates required for biosynthetic pathways including citrate and glycerol for lipid synthesis, ribose for nucleotides, and amino acids.

It has been shown that increased lactate secretion allows acidification of extracellular environment favouring tumour invasion due to pH dependent activation of cathepsines and metalloproteases which allows degradation of extracellular

matrices and membranes of neighbouring tissues (Kroemer and Pouyssegur, 2008; Swietach et al., 2007).

Thus glycolytic pathway has emerged as an interesting potential target in cancer therapy. Inhibitors of enzymes involved in glycolytic pathway like *HK-2* (DeWaal et al., 2018), *PFK1* (Zhu et al., 2016), *LDHA* (Fantin et al., 2006) have shown promising outcome in inhibiting tumour growth and some are in clinical trials (Figure 1.5)

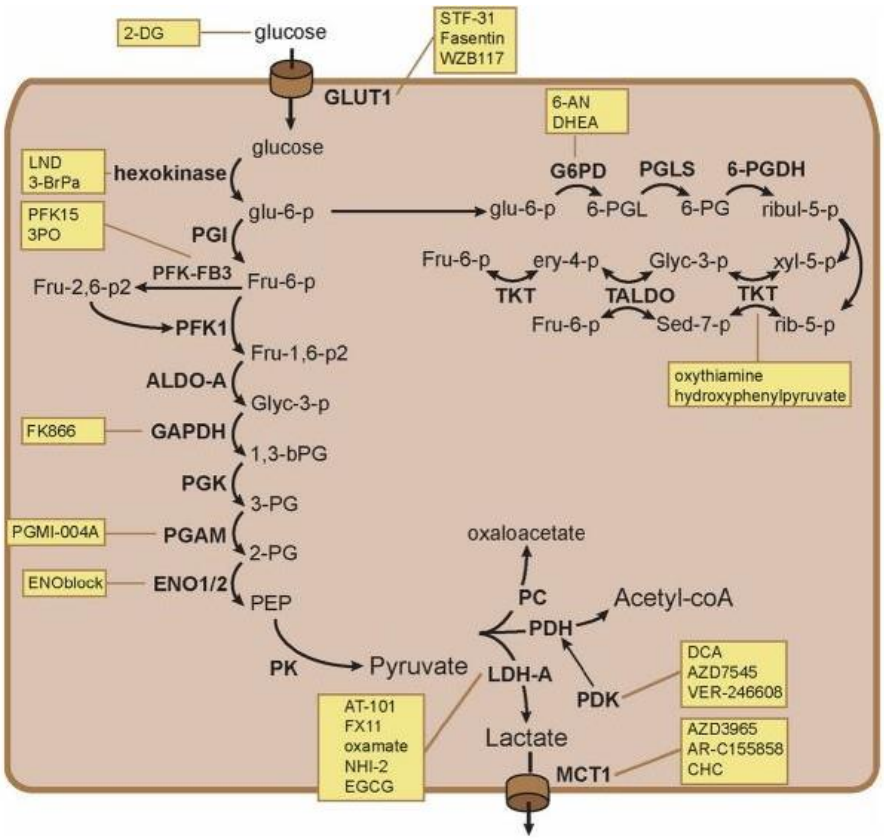

Figure 1.5: An overview of glycolytic inhibitors along with their respective targets. Adapted from (van der Mijn et al., 2016)

Cancer cells constantly need to manage their high oxidative stress as well as nucleotide synthesis to maintain their highly proliferative nature, for which they heavily rely upon pentose phosphate pathway (PPP) to meet its anabolic demands (Patra and Hay, 2014). The glucose which enters into the cells gets phosphorylated into glucose-6-phosphate and then can be destined towards glycolysis or can be shunted by glucose-6-phospate dehydrogenase (*G6PD*) towards PPP. The shunted glucose then can be utilized to produce reducing equivalents NADPH via the oxidative branch of PPP and ribose-5-phosphate via the non-oxidative branch which serves as the backbone for nucleotide synthesis, thus Targeting PPP could vastly be exploited for cancer therapy.

1.3.3 Glutaminolysis exploited

Glutamine being the most abundant amino acid in human serum plays an important role as a source of carbon for biosynthesis of macromolecules and regulation of cellular redox potential. Carbons derived from glutamine are used not only for synthesis of amino acids but also to replenish intermediates of TCA cycle (DeBerardinis et al., 2007). Glutaminolysis refers to the process where glutamine is converted to alpha-keto glutarate (aKG) via glutamate. It has been shown that cancer cells consume glutamine in larger amounts than normal cells (Eagle, 2007; Sauer et al., 1982) and the consumed glutamine can be redirected towards lactate production which can promote cancer cell growth, known

as the WarburQ effect (Damiani et al., 2017). Glutamine is shown to promote resistance to cell death in cancer (Wise et al., 2008) and could also be a potentially drive resistance to drugs against cancer treatment. The complete oxidation of glutamine requires aKG to enter TCA cycle and exit as malate. Malate subsequently gets converted to pyruvate via malic enzyme and subsequent re-entry into TCA cycle as acetyl-CoA with subsequent ATP production.

Glutamine can also be converted to citrate via a specialized mechanism known as reductive carboxylation followed by glutaminolysis. Reductive carboxylation of glutamine mediated by isocitrate dehydrogenase 1 (*IDH1*) has been shown to support tumour growth (Mullen et al., 2012) and is a major contributor for production of cytosolic Acetyl-CoA required for lipid synthesis (Metallo et al., 2012) as well as epigenetic regulation via histone acetylation mediated by the action of ATP citrate lyase (*ACLY*) (Wellen et al., 2009).

Glutamine metabolism has emerged as a promising target and glutaminase inhibitors like CB-839 are now under clinical trials for treatment of cancer patients (Xu et al., 2018).

1.3.4 *de-novo* fatty acid synthesis

Rapidly proliferating cancer cells constantly require large stocks of lipids as building blocks for assembly of biological membranes. Though majority of the cells in our body derive the required lipids from bloodstream, many cancer cells show activation of *de-novo*

lipid synthesis. This excessive lipid demand is fulfilled via transport of mitochondrial citrate into cytosol via mitochondrial citrate carrier (*SLC25A1*) followed by breakdown of citrate into oxaloacetate and Acetyl-CoA via *ACLY*. Malic enzyme further converts the formed OAA into pyruvate generating the necessary NADPH required for lipid synthesis. Biosynthesis of lipids begins with the carboxylation of cytosolic Acetyl-CoA into malonyl-CoA by acetyl-CoA carboxylase (*ACC*) which gets assembled into long chains of fatty acid chains via the action of fatty acid synthase (*FASN*) (Figure 1.6).

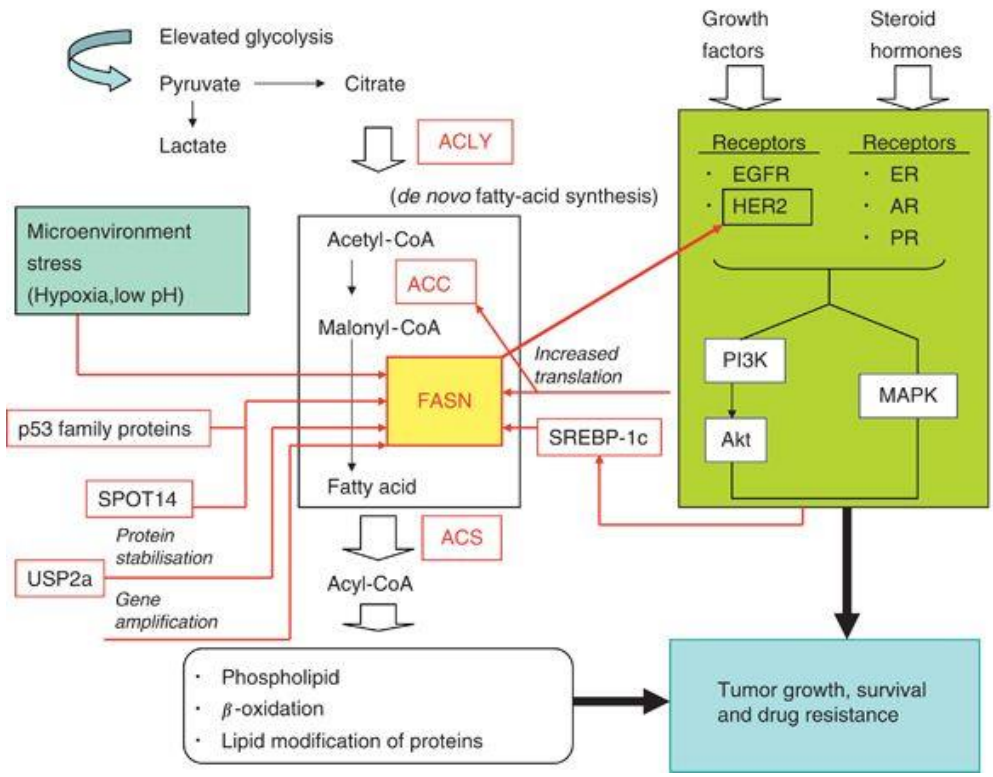

Figure 1.6: regulation of de novo lipid synthesis in cancer: Growth factors and hormone receptors play essential roles in tumour-related FASN overexpression. Tumour microenvironment stress, as well as multiple other factors are involved in FASN overexpression and elevated lipogenesis in cancer. FASN and growth factor-dependent signalling are mutually regulated in cancer cells (Mashima et al., 2009).

Lipogenesis is controlled by many signalling pathways which are often deregulated in cancer. *SREBPs* (Sterol regulatory binding proteins) greatly control synthesis of fatty acids and cholesterol. Akt is also shown to phosphorylate *ACLY* (Berwick et al., 2002) and activate expression of genes involved in cholesterol and fatty acid synthesis (Porstmann et al., 2005).

Targeting enzymes involved in fatty acid metabolism such as *ACLY* (Shah et al., 2016), *SLC25A1* (Fernandez et al., 2018), 3-hydroxy-3-methylglutaryl-CoA reductase (HMGCR) (Nguyen et al., 2015) have not only shown to restrict tumour growth but also to resensitize cancer cells to therapy. Some Inhibitors of lipid synthesis are now under clinical trials (Bjarnadottir et al., 2013).

1.3.5 Redox homeostasis and ROS detoxification

Reactive oxygen species (ROS) are by-products of glycolysis and oxidative metabolism carried out in mitochondria that must be excreted or neutralized. ROS is essential for many biological functions such as cell growth, inflammation and also acts as signalling molecule (Finkel, 2011).

ROS has been associated with a large number of diseases and also cancer. In cancer cells a disruption of redox homeostasis is observed along with high levels of ROS resulting in oxidative

stress. Oxidative stress mediated signalling events have been shown to promote phenotypical traits of cancer cells like, motility, adhesion, tumour stemness and proliferation (Figure 1.7) (Sosa et al., 2013). As mentioned moderate amounts of ROS is beneficial for cancer cells but high levels can induce cell death, thus cancer cells regulate their ROS levels by modulations of pathways producing NADPH as well as ROS scavenging pathways such as superoxide dismutases, glutathione peroxidase, peroxiredoxins, glutaredoxins, thioredoxins or catalase.

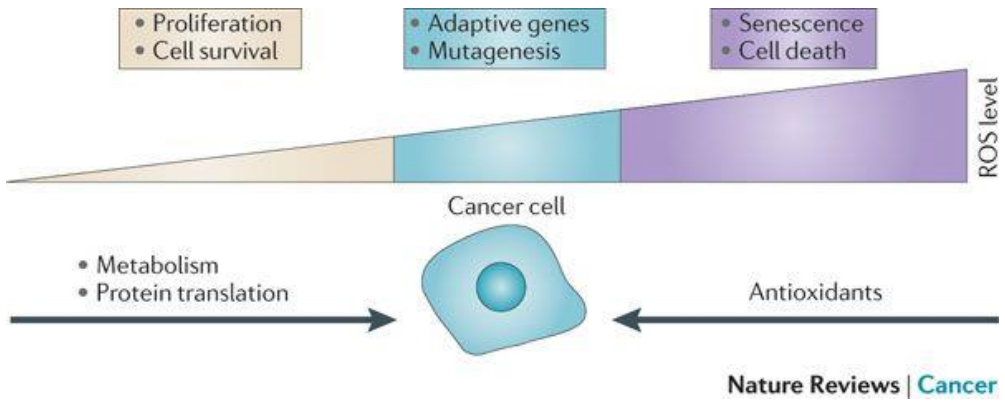

Figure 1.7: ROS levels and cancer. Low levels of ROS can promote proliferation and cell survival whereas high ROS levels can induce cell death. Cancer cells very cleverly manage their ROS levels via balancing metabolic machinery involved in ROS production as well as antioxidant mediated ROS scavenging towards their benefit (Cairns et al., 2011).

1.3.6 Altered mitochondrial metabolism

For a long time it was believed that cancer cells derive all their energy via glycolysis due to excessive damage to mitochondrial

respiration (Warburg, 1956). Even though this phenomenon is partially, observed in many cancer, complete damage of mitochondrial function is detrimental for cancer cells (Vyas et al., 2016). Mitochondria's are highly specialized organelles involved in variety of cellular functions like energy homeostasis, redox homeostasis, generation of ROS, maintenance of cytosolic calcium levels (Ca^{2+}), production of biosynthetic precursors such as Acetyl-CoA, and initiation of apoptosis.

As mentioned before that cancer cells exploit glutaminolysis to alter TCA cycle metabolism, one of the major pathways occurring inside mitochondria.

Mitochondria are also responsible for production of Acetyl-CoA which can also be generated by oxidation of fatty acids inside the mitochondria. Cancer cells are known to upregulated carnitine palmitoyltransferase (Zaugg et al., 2011), an enzyme responsible for the import of Fatty acyl-CoA into the mitochondria which can be hydrolysed to generate ATP fuelling cancer growth.

Cancer cells are also known to employ reverse Warburg effect where H_2O_2 secreted by cancer cells forces adjacent fibroblast to switch to glycolytic metabolism due to H_2O_2 mediated mitochondrial damage. The lactate and ketones secreted by fibroblasts are then used as to feed cancer cells mitochondrial energy production and produce precursors for cancer cell biogenesis (Bonuccelli et al., 2010).

Cancer cells can also regulate their intrinsic Ca^{2+} levels by phosphorylation of type 3 inositol triphosphate receptor which reduces intrinsic calcium levels (Pinton et al., 2011) and possibly

inactivation of mitochondrial apoptotic pathways thus improving cancer cell survival.

1.4 METABOLIC REGULATION OF EPIGENETICS

Cancer can be described as a culmination of different epi-phenomena resulting in a unique regulation of its gene expression favouring sustained growth, proliferation and survival of cancer cells. This complex regulation of gene expression can be controlled by various epigenetic machinery such as methylation, acetylation, GlcNAcylation and phosphorylation. Large number of global epigenetic abnormalities along with genetic alterations have been observed in a wide variety of cancers (Hatada, 2010; Jones and Baylin, 2002).

Various metabolic pathways help in synthesis of important metabolites that are essential for maintenance of cancer cell epigenetic landscape (Figure 1.8).

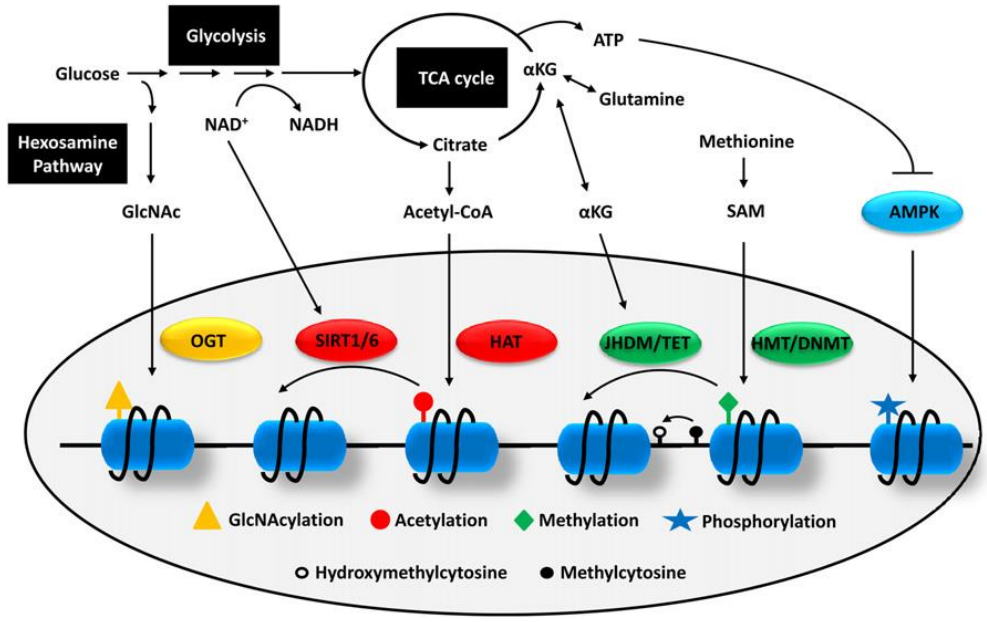

Figure 1.8: Metabolic pathways and metabolites involved in regulation of epigenetic machinery (Lu and Thompson, 2012).

1.4.1 Histone and DNA Methylation

Methylation is the process of addition of methyl group to DNA or lysine/arginine groups of histone complex. Methylation requires transfer of methyl group from S-adenosyl-methionine (SAM) to either DNA or histone by the action of DNA methyl transferases (DNMTs) or Histone methyl transferases (HMTs) respectively. SAM is derived through methionine metabolism and alteration of methionine metabolism can have direct effect on DNA/Histone methylation and consequently, alter gene expression (Mentch et al., 2015). (Figure 1.9)

Cancer cells are known to show hypermethylation in CpG islands of regions controlling expression of tumour suppressor genes such as retinoblastoma 1 or BRCA1 whereas overall all global hypomethylation of DNA (Esteller, 2000; Feinberg and Vogelstein, 1983; Greger et al., 1989). Histone methylation also plays a significant role in cancer where nearly half of all the HMTs known are associated with cancer (Albert and Helin, 2010).

TCA cycle intermediate aKG acts as a substrate for Jumonji-C (JMJC) domain-containing HDMs (JHDMs) and TET methylcytosine dioxygenases, which also take part in regulation of DNA methylation. These dioxygenases are inhibited by structurally similar metabolites such as fumarate, succinate and 2-hydroxyglutarate (Xiao et al., 2012).

Targeting methionine metabolism by regulating methylthioadenosine phosphorylase and inhibiting protein

arginine N-methyltransferase 5 (PRMT5) can be exploited for therapeutic purposes in cancer (Marjon et al., 2016).

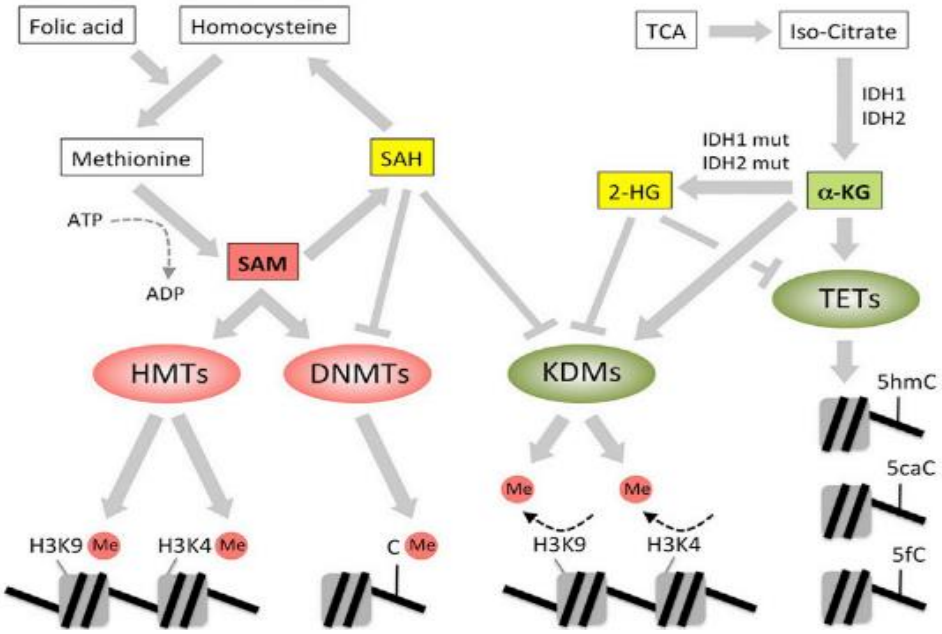

Figure 1.9: DNA and histone methylation. Schematics representing production of SAM via methionine metabolism involved in DNA and histone methylation mediated by the action of DNMTs and HMTs respectively. TCA cycle regulation of TETs and histone lysine demethylases (KDMs). Adapted from (Etchegaray and Mostoslavsky, 2016).

1.4.2 Histone acetylation

Acetyl-CoA fuels TCA cycle for generation of ATP under aerobic condition and is a crucial building block for lipids, cholesterol and other components required for cell growth. Acetyl-CoA is also a substrate for histone acetyl transferases (HATs) which mediates epigenetic control by transfer of acetyl groups onto histone tails.

Global histone acetylation levels vastly vary within the cells of tumour itself, which reflects the cellular diversity probably due to differences in tumour microenvironment (Seligson et al., 2009).

Global histone acetylation levels are greatly influenced by the activity of three enzymes *ACLY*, *PDC* and *ACSS2*. These enzymes utilize intermediates of metabolic pathways like TCA cycle or glycolysis like citrate, pyruvate and acetate to produce acetyl-CoA in the nucleus. Acetyl-CoA can also be produced locally in sub nuclear domains to specifically acetylate certain histone targets by action of lysine acetyltransferases (*KAT*) (Figure 1.10).

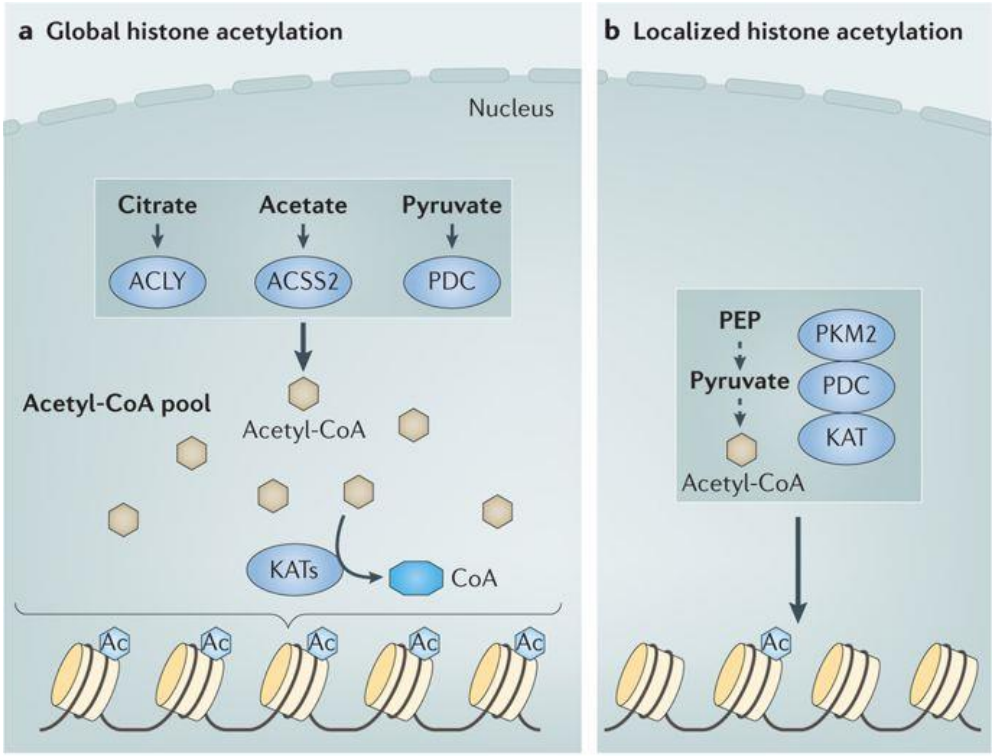

Figure 1.10: Metabolic regulation of global and local histone acetylation by conversion of metabolites like citrate, acetate and pyruvate into Aceyl-CoA.

Targeting these enzymes has emerged as a double edge sword as it allows interfering with metabolic-epigenome axis. Many of the drugs targeting these enzymes are under clinical trials treatment, such as Dichloroacetate (DCA) which activates PDC (Chu et al., 2015), N-(2,3-di-2-thienyl-6-quinoxalinyl)-N′-(2-methoxyethyl) urea which inhibits *ACSS2* activity (Comerford et al., 2014) and BMS-303141 (Li et al., 2007), ETC-1002 (Gutierrez et al., 2014) and hydroxycitrate (Ballantyne et al., 2013) inhibiting *ACLY* activity.

1.5 TOOLS TO IDENTIFY METABOLIC VULNERABILITIES

1.5.1 Enzymatic assays

Metabolic differences in cancer cells are mediated by dysregulation of various metabolic enzymes of key pathways in order to gain or lose certain metabolic functions by upregulating or downregulating important metabolites involved in cellular function. Traditionally, quantification of certain metabolites were done by introducing purified enzymes into biological system such as biological fluid or cell suspension and measuring the levels of product formed indicating the presence and abundance of metabolites under investigation. An array of different metabolic enzymes will provide an information on the levels of different metabolites present in the system which can be used to assess the biological activity happening in the cell.

Enzymatic assays can also be used to assess certain organellar information such as Citrate synthase activity can provide an information about mitochondrial activity and density of the cell (Peyrot et al., 2018). Though enzymatic assays allow to gauge into certain metabolic functions, they only allow to do so one metabolite at a time, providing a very narrow perspective of metabolism.

1.5.2 Transcriptomics

Transcriptomic refers to the study of transcriptome (complete set of RNA transcripts) of a cell. Investigation of gene expression can

highlight on the activity of key metabolic genes whose upregulation or downregulation could influence metabolic profiles in cancer cells.

Even though transcriptomic activity does not always really translate down and reflect on metabolic activity, integrated analysis of transcriptomic and metabolomics together can be utilized to uncover enhanced enzyme-metabolite coupling in cancer (Auslander et al., 2016), and can be combined with genome scale metabolic models to perform systems level analysis of cancer cell metabolism (Lewis and Abdel-Haleem, 2013).

1.5.3 Proteomics

The study of the protein composition of the cells is referred to as proteomics. Many proteomics based techniques like Reverse Phase Protein Array (RPPA), LC-MS/MALDI based proteomics, etc can give an information about the alteration of protein levels of metabolic enzymes. Even though estimation of protein levels can give an idea about the metabolic activity of the cells, we still cannot determine the exact effect of it on metabolism as protein levels does not necessarily correlate with protein activity which highly depends on many post translational modifications (Ryšlavá et al., 2013). Proteomics based analysis of metabolism has been used to elucidate the role of many metabolic enzymes of glycolysis and glutamine metabolism (Zhou et al., 2012), which can be coupled to other techniques to perform an integrative analysis of cancer metabolism.

1.5.4 Metabolomics

Metabolome refers to the complete set of small molecule metabolites (less than 1kDa) present in a system such as a cell or body fluids, and metabolomics refers to the study of metabolome by simultaneous measurement of hundreds of metabolites (Dunn et al., 2005). Metabolomics is the youngest of *–omics* technologies when compared to genomics, transcriptomics and proteomics, and provides a holistic view of metabolism telling us what is actually happening in a system (Schmidt, 2004) and can be exploited to get accurate knowledge on the biological state of a tumour.

Initial metabolomics techniques were based on use of nuclear magnetic resonance (NMR), but now they are complemented with very high throughput mass spectrometers (MS) providing much higher sensitivity and wider range of detection of metabolites (Griffiths et al., 2010).

NMR is based on analysis of certain magnetic properties of nucleus of atoms, and it identifies compounds based on the differences in atomic composition. When introduced under high magnetic field, different atoms in a compound behave differently based on how atoms are influenced by their surrounding atoms as well based on their intrinsic properties. This knowledge of differences in atomic behaviour of different compounds is used to identify as well as quantify their levels in biological systems. NMR allows quantification of metabolites in micro molar ranges and since it being non-destructive, the analytes can be further processed for other investigations, adding a great value for highly

precious samples like patient materials. Disadvantage of using NMR techniques is its low sensitivity and low range of detection of metabolites when compared to MS.

MS uses differences in masses of compounds based on their atomic composition to identify and quantify metabolites. MS techniques are coupled to separation techniques like gas or liquid chromatography which can better resolve and separate the compounds based on their physico-chemical properties. These separation techniques help separate different metabolites based on their retention time so that different metabolites reach the MS at different times. Combination of both retention time and mass provides accurate identification of metabolites and LC/GC-MS together can provide identification and quantification of a wide spectrum of metabolites (Figure 1.11).

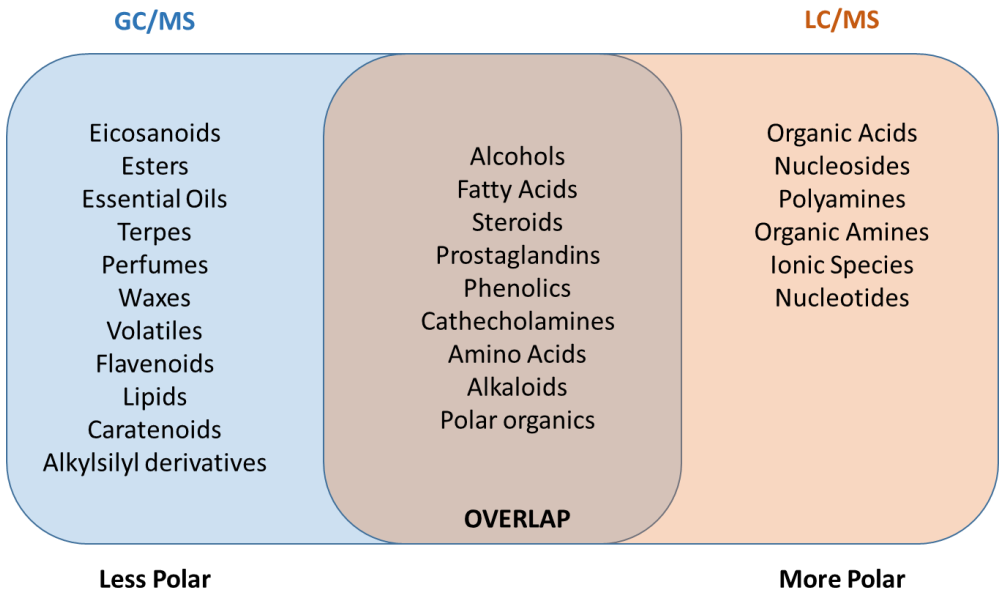

Figure 1.11: Spectrum of metabolites that can be detected using LC/GC-MS

One drawback of using MS is that the technique is disruptive and hence the samples cannot be subjected for further evaluation, but this technique is highly sensitive and allows very low detection limit (<5 ppm).

Untargeted metabolic profiling has been extensively used in cancer profiling and identification of biomarkers for the disease (Lam and Law, 2014) (López-López et al., 2018).

1.5.5 Stable isotope tracing

Measurement through metabolomics can give an information about the steady state levels of metabolites but does not provide information on specific reaction rates that generated those metabolites. Due to recent advancement in analytical techniques, stable isotope tracing approach has become widely popular to analyse specific rates of reactions and identify specific metabolic routes taken by the cells to rewire their metabolism. Analysis of metabolic fates of precursors like glucose or glutamine labelled with isotope of carbon ^{13}C provides an insight on the dynamic activity of metabolic pathways and provides mechanistic explanations for perturbations observed during steady state metabolomics analysis. Stable isotope technique has helped researchers to identify various additional metabolic pathways that are activated in cancer such as transketolase 1 (*TKTL1*) pathway (Diaz-Moralli et al., 2016), acetate metabolism (Mashimo et al., 2014), reductive metabolism of glutamine (Metallo et al., 2012), one carbon metabolism (Yang and Vousden, 2016), glycine and

serine metabolism (DeBerardinis, 2011), thus, enhancing the perspective about metabolic rewiring engaged by cancer cells in order to adapt and manipulate their microenvironment.

1.5.6 ^{13}C metabolic flux analysis (MFA)

To understand the complexities of mammalian systems we require systems level approaches to analyse the differences in metabolic network in different phenotypes (Thiele et al., 2013). The isotope distribution data obtained through tracer experiments can be combined along with the knowledge about specific growth rates as well as consumption and secretion rates of metabolites into a MFA assigns flux values to the reactions in the model network and confidence intervals for each estimated fluxes (Figure 1.12). The fluxes are resolved using an elementary metabolite unit (EMU) framework that allows efficient simulation of isotopic labelling data in a biochemical network model (Antoniewicz et al., 2007)metabolic model. The model consists of network of reactions from various different metabolic pathways which can be used to computational quantify the intracellular fluxes in cancer cells.

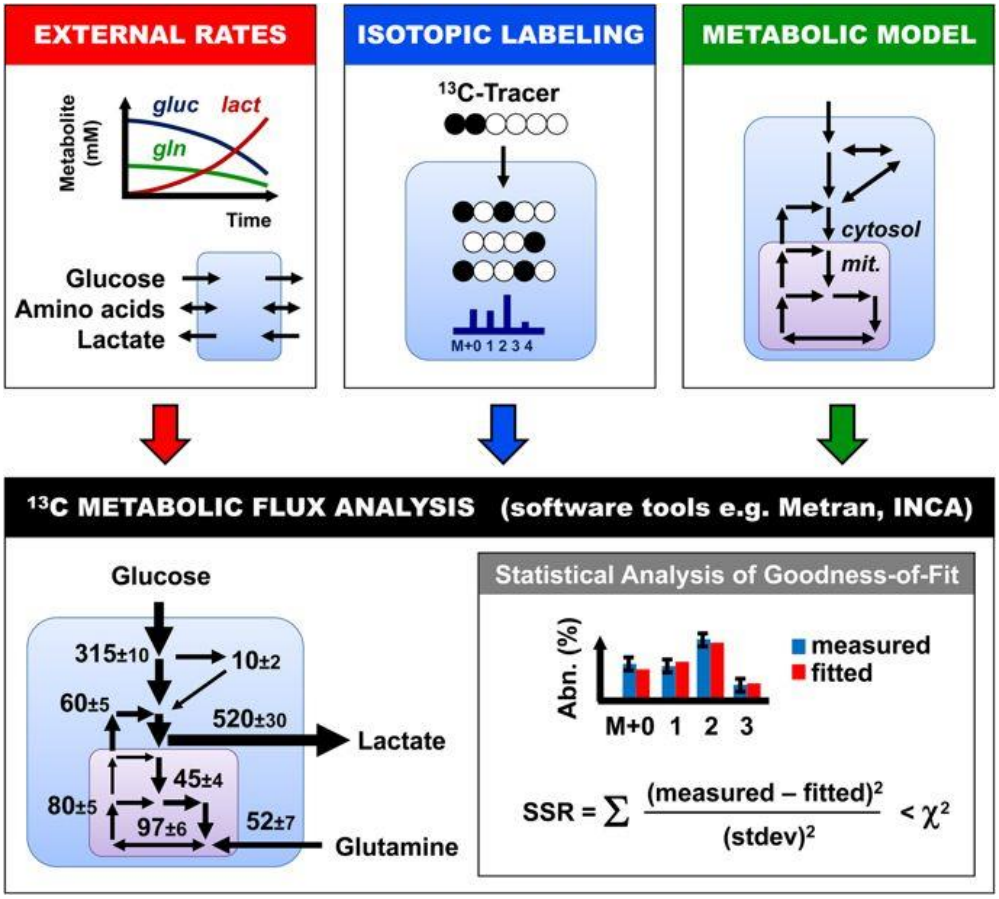

Figure 1.12: Schematics for application of ^{13}C MFA in cancer studies. Information about growth rates, metabolite consumption and secretion as well as isotope tracer data are combined into metabolic network and the intracellular fluxes can be resolved using software like INCA and metran providing a detailed understanding about the differences in flux distributions in cancer cells (Antoniewicz, 2018).

.

1.5.7 Genome scale metabolic models (GSMMs) and Flux balance analysis

Construction of the genome scale metabolic network has enabled researchers to simplify the complexity of the vast human metabolism (Brunk et al., 2018). GSMM networks consists of all known metabolic reactions of an organism and the genes that encode for each enzyme.

Flux balance analysis (FBA) is a mathematical approach to analyse the flow of metabolites through a metabolic network. FBA approach applied on GSMMs makes it possible to predict the growth rate of an organism for e.g. cancer or the rate of production of important metabolites that can drive tumour growth.

FBA can be constrained using already, known information about the organism (Constraint based modelling (CBM)) such as consumption and secretion rates of metabolites or other *–omics* data like transcriptomics data can be mapped on the models thus allowing flow metabolites through a reaction only within certain limits correlating with the gene expression level (Özcan and Çakır, 2016). This allows system level investigation about the phenotype, combining information obtained through different approaches.

FBA techniques work by finding the best solution i.e. flux distribution for a given objective function (Maximise biomass or ATP) within the given constraints (Figure 1.13).

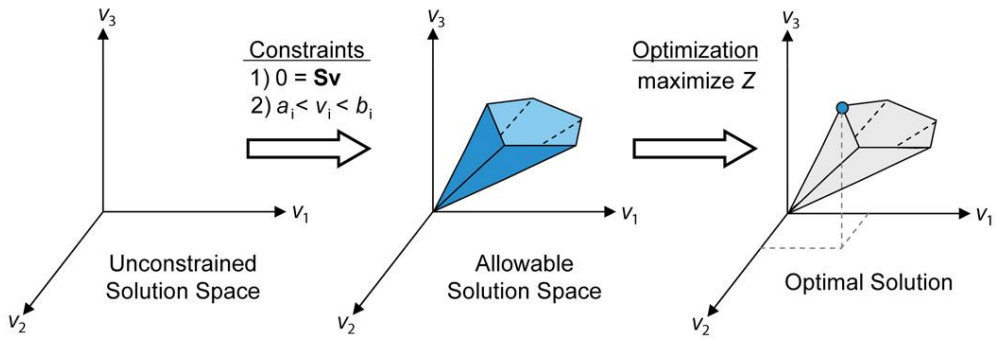

Figure 1.13: Concept of flux balance analysis. With no constraint the flux distribution may lie at any given space, but when constraints are applied it restricts the flux distribution within an allowable solution space and the network may acquire any flux distribution within this space. FBA can identify a single best optimal flux distribution for a given objective function which lies on the edge of the allowable solution space.

Usually, FBA requires a user determined objective function, but FBA can be reengineered to use flux distribution obtained through ^{13}C MFA and identify the objective function to best match the input flux distribution. This would allow researchers to better understand the cancer cell behaviours and what the cancer cells are trying to do for e.g. upon drug treatment.

2. AIM OF THE THESIS

Cancer research has seen a renewed interest in understanding cellular metabolism, which today stands crucial for the development of more efficacious and personalized treatment strategies. A detailed understanding of cancer metabolic rewiring is essential to identify the metabolic vulnerabilities of the cancer cells in order to offer new potential avenues for cancer treatment. This thesis is part of recent and promising scientific interest which aims not only to shed on the metabolic differences among various tumours, but also to dissect the metabolic reprogramming engaged by cancer cells in response to various drug treatment, thus, contributing to the combined global effort towards precision medicine. The main objectives of this thesis can be divided into three specific aims.

1. Analysis of metabolic differences in oncogenic K-Ras driven lung and colon cancer cells and test a combinatorial treatment strategy targeting glutaminolysis and aldolase activity towards restraining tumour growth and proliferation.

2. Understand metabolic rewiring driving resistance to endocrine therapeutic drugs in ERα positive breast cancer using metabolomics and systems level modelling approach.

3. Investigate the role of glutamine in promoting enhanced proliferation of K-Ras transformed NIH3T3 mouse fibroblast, by substituting it with respective nitrogen source (Non-essential amino acids) and carbon source. (alpha-ketoglutarate)

3. CHAPTER 1

Metabolomics fingerprinting for the identification of combinatorial drugs treatment able to strongly inhibit K-Ras human tumour growth

Daniela Gaglio[1,2,*], Marcella Bonanomi[2,3], Silvia Valtorta[1,2,4], Rohit Bharat[2,3], Marilena Ripamonti[1,2], Paola Paci[2,5], Federica Conte[2,5], Giulia Fiscon[2,5], Federico Papa[2,5], Isabella Raccagni[1,2,6], Seth J Parker[7], Anna Maria Colangelo[2,3], Christian M Metallo[7], Rosa Maria Moresco[1,2,4] and Lilia Alberghina[2,3]

[1]*Institute of Molecular Bioimaging and Physiology, National Research Council (IBFM-CNR), via F.lli Cervi 93, 20090 Segrate, MI, Italy.*

[2]*SYSBIO.IT, Centre of Systems Biology, Piazza della Scienza 2, Milano 20126, Italy.*

[3]*Department of Biotechnology and Biosciences, University of Milano-Bicocca, Piazza della Scienza 2, 20126 Milan, Italy.*

[4]*Department of Medicine and Surgery, University of Milano-Bicocca, Via Cadore 48, 20900 Monza, Italy;*

[5]*Institute for Systems Analysis and Computer Science "Antonio Ruberti", National Research Council, Rome, Italy*

[6]*Experimental Imaging Center, IRCCS San Raffaele Scientific Institute, Milan, Italy.*

[7] *Department of Bioengineering, University of California, San Diego, La Jolla, CA, USA; Moores Cancer Center, University of California, San Diego, La Jolla, CA, USA.*

*Corresponding authors:

Gaglio D *E-mail address:* daniela.gaglio@ibfm.cnr.it

Highlights

- Metabolic fingerprinting of tumours can identify personalized medicine
- Combinatorial glycolysis and glutamine metabolism inhibitors cooperate *in vivo* to induce tumour growth inhibition

Keywords:

Metabolic rewiring, metabolic cancer therapy, metabolic fingerprinting, glycolysis, glutamine, combinatorial drugs treatment.

(Manuscript in preparation)

3.1 ABSTRACT

Cancer cells are characterized by a metabolic rewiring using glucose and glutamine to sustain the enhanced and unrestricted growth. We experimentally detect metabolic fingerprinting to better identify effective therapies in A549-K-RasG12S lung cancer cells and HCT116-K-RasG13D colon cancer cells. Consistently with ability of tumour cells to carry out a metabolic switching from glucose to glutamine and vice versa observed, we teste isolated or combined effects of CB-839 glutaminase inhibitor and BKM120 PI3K and aldolase activity inhibitor to tear down the versatile metabolic phenotype. We show that combinatorial drug treatment both in vitro and in tumour xenografts is effective in restraining growth in both cancer cell types, with a more pronounced effect observed for A549 lung cancer cells. This study support the notion that cancer metabolic fingerprint may be useful to select combined precision treatment in a clinical trial setting

3.2 INTRODUCTION

Cancer cells are characterized by a metabolic rewiring in which glucose is converted to lactate and glutamine metabolized to α-ketogluatarate (Akg) in the tricarboxylic acid (TCA) cycle generating complex flexible metabolic pathways able to sustain the enhanced and unrestricted growth of cancer cells (Davidson et al., 2016; Gaglio et al., 2016). This basic scheme may be modified by the presence in the cellular environment (both in vivo and in vitro) of amino acids such as proline, arginine, asparagine, and lactate (Elia et al., 2017; Kremer et al., 2017; Pavlova et al., 2018; Sonveaux et al., 2008).

The kind of activated oncogenes (Hsu and Sabatini, 2008; Wolpaw and Dang, 2017), the tissue of origin of the tumours, nutrients and cytokines present in the tumour stroma have all been reported to affect cancer metabolic rewiring (CMR) (DeBerardinis and Chandel, 2016; Rahman and Hasan, 2015). CMR may be activated by oncogenic K-Ras, found mutated in approximately 35% of lung adenocarcinomas and 45% of colorectal cancers and able to increased tumourigenicity, poor prognosis, environmental adaptation and acquired drug resistance (Rahman and Hasan, 2015).

Metabolomics profiling technologies, metabolic pathway identifications and flux analysis are able to experimentally determine metabolomics fingerprinting (Nielsen, 2017) to better characterize the metabolic pathways followed in any given CMR. Although the described metabolic rewiring has already been taken to open new therapeutic windows, pursued by a number of new

inhibitors and drugs, the complexity and heterogeneity of cancer metabolism, has not allowed, so far, predictive ability and full exploitation of CMR for precision oncology. It is therefore of interest ascertain whether it would be possible to detect any correlation between metabolic fingerprinting and drug sensitivity, in order to better identify effective therapies.

CMR inhibitors like CB-839, a reversible, non-competitive allosteric glutaminase (GLS) inhibitor, has been reported to exhibit an anti-proliferative activity in triple-negative breast cancer (TNBC) cell lines and xenografts (Gross et al., 2014). CB-839 was well tolerated in preclinical studies in mice, with no weight loss or toxicity observed, reducing cancer cell growth "in vitro" but not "in vivo" (Davidson et al., 2016; Gaglio et al., 2016). Inhibitors targeting signalling steps such as pan-PI3K inhibitor NVP-BKM120 (BKM120), are known to inhibit cancer cell growth and able to decrease glucose consumption by modulating release of active aldolase from actin cytoskeleton in vitro and in vivo (Hu et al., 2016).

To get deeper insight in the many issues previously raised on the interplay of oncogenic K-Ras, origin tissue, cancer metabolic rewiring and drugs sensitivity, here we provide evidences that A549-K-RasG12S lung cancer cells and HCT116-K-RasG13D colon cancer cells present clear differences in their metabolic rewiring and in sensitivity to treatments with either BKM120 or CB-839 as detected using metabolomics-mass-spectrometry approaches.

Combinatorial drug treatment both in vitro and in tumour xenografts is effective in restraining growth in both cancer cell types, with a more pronounced effect observed for A549 lung cancer cells. Therefore, we propose that a cancer cells typing by detailed metabolic profiling and/or metabolic pathways analysis may be useful to select precision treatment performed in a clinically relevant timeframe

3.3 RESULTS

3.3.1 Differences in metabolic pathways detected in vitro in A549 lung and HCT116 colon human cancer cell lines

A detailed cellular typing of A549-K-RasG12S (A549) lung cancer cells, HCT116-K-RasG13D (HCT116) colorectal cancer cells and Ros1-driven lung cancer cells HCC78, was performed (Figure 3.S1A). Consistently with the published data (Gaglio et al., 2016), growth curves showed similar high proliferation rates in A549 and HCT116 cancer cell lines as compared to Ros1-HCC78 (Figure 3.S1A). Statistical PCA analysis of untargeted metabolomic profiling revealed a similar metabolic phenotype in A549 and HCT116 cancer cell lines as compared to Ros1-HCC78 lung cancer cells (Figure 3.1A). These data were consistent with the rates of glucose and glutamine consumption and of lactate and glutamate secretion in A549 and HCT116 as compared to HCC78 cells (Figure 3.S1B), as well as with the proliferation rates under nutrients deprivation (Figure 3.S1C and 3.S1D). As shown in Figure 3.S1C and S1D, A549 and HCT116 cancer cells exhibited reduced rate of growth both under glucose and glutamine limitation, confirming that activated K-Ras sustained enhanced growth by using both nutrients (Gaglio et al., 2011), while HCC78 cancer cells, driven by oncogenic Ros 1, cells are glutamine limitation insensitivity but showed glucose dependence in sustaining cell proliferation (Figure 3.S1C and 3.S1D).

To better profile A549 and HCT116 metabolism, we measured the relative abundance of intracellular metabolites of glycolysis and TCA cycle (Figure 3.1B).

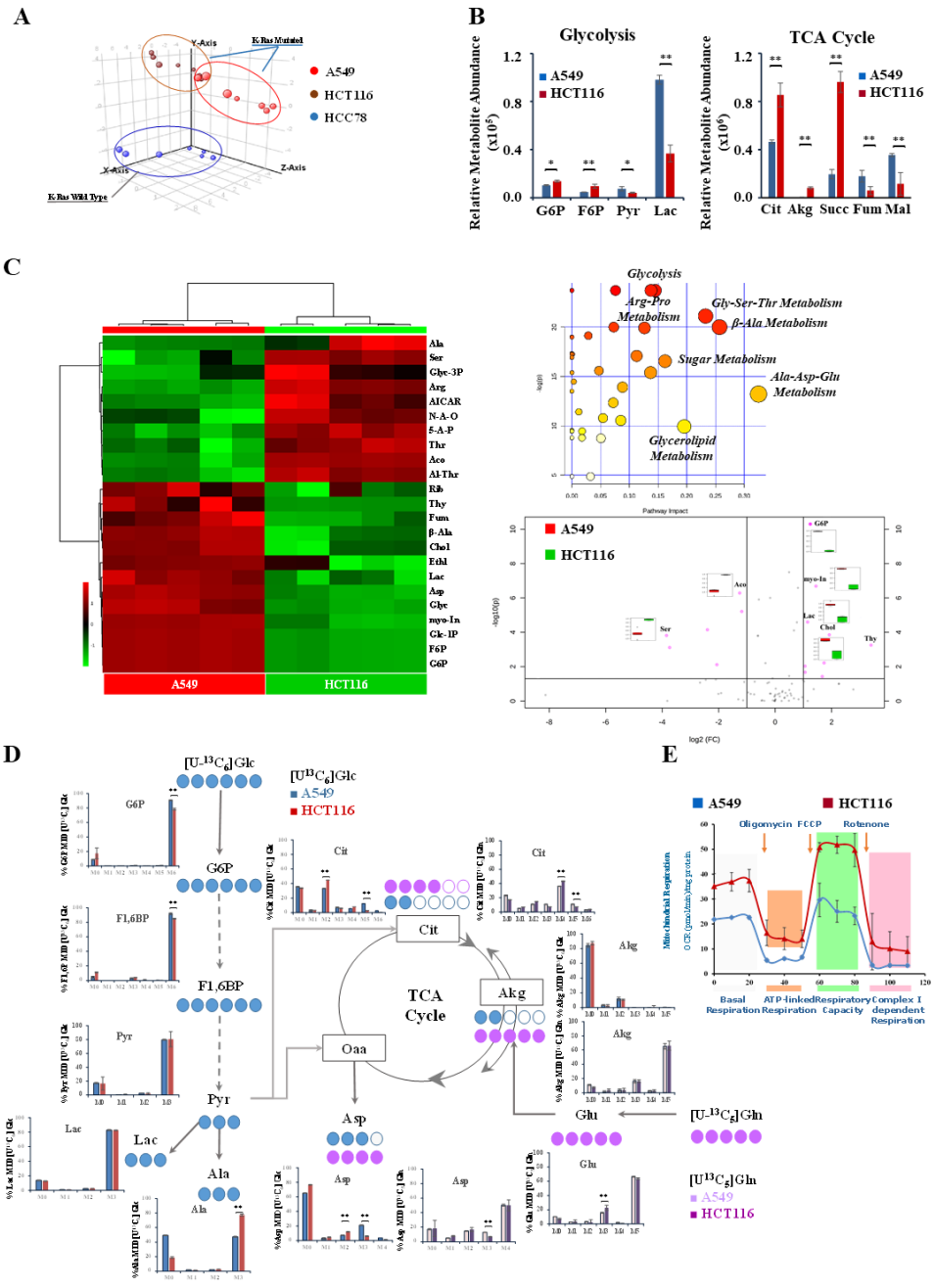

Figure 3.1. Metabolic phenotyping of A549-K-Ras^{G12S} (A549) and HCT116-K-RasG13D (HCT116) human cancer cell lines

(A) Principal component analysis (PCA) of A549 (■), HCT116 (■) and HCC78 (■), with mean centering and scaling to display the inherent variance between the metabolic phenotypes.

(B) Relative metabolite abundances in A549 (■) and HCT116 (■) cells measured by GC/MS.

(C) Untargeted metabolic profiling of A549 lung and HCT116 colon-rectal cancer cell lines. Hierarchical clustering heatmaps show significantly ($p \leq 0.05$) different intracellular metabolites by LC-MS and GC-MS (left panel). Enriched metabolic pathways were ranked according to their FDR values calculated by the MetPa method implemented in MetaboAnalyst 4.0 software (upper right panel). The most significant pathways were represented by both the bigger/red dots and by those dots with higher log p value. The pathway impact is calculated as the sum of the importance measures of the matched metabolites normalized by the sum of the importance measures of all metabolites in each pathway. Volcano plot showing metabolites with fold change (FC) > 2 and cutoff of $P < 0.005$ (lower right panel)

(D) Atom transition map of [U-$^{13}C_6$].glucose (blue circles) and [U-$^{13}C_5$]-glutamine (violet circles) used to detect metabolic changes. Filled circles indicate ^{13}C enrichment. Glycolysis and TCA cycle intermediates metabolites labelling from [U-$^{13}C_6$]-glucose and [U-$^{13}C_5$]-glutamine in A549 (■) and HCT116 (■) cancer cells.

(E) Mitochondrial respiration reflected by OCR levels was detected in A549 CTR (■) and under combinatorial treatment (■) cancer cells under basal conditions or following the addition of oligomycin (0.1 μM), the uncoupler FCCP (F, 0.5 μM) or the electron transport inhibitor Rotenone (R, 2 μM). (n=5).

Although oncogenic human K-Ras cancer cells showed a similar basic metabolic phenotype, the relative abundance of intracellular metabolites involved in glycolysis and

TCA cycle metabolism suggested a preferential glucose utilization to lactate in A549 lung cancer cells, as compared to HCT116 colon cancer cells showing increased relative abundance level of Cit and Succ (Figure 3.1B). Furthermore, statistical analysis of the

untargeted metabolic profiling performed in A549 and HCT116 cancer cells showed an enrichment of metabolites involved in glycolysis, amino acids metabolism, amino sugar metabolism, inositol phosphate metabolism (inositol signalling pathway) and glycerolipid metabolism (Figure 3.1C). Notably, metabolites associated with glycolysis including branching of glycerol phosphate shuttle (such as G6P, F6P and Lac) displayed statistically significant higher levels in A549, as compared to HCT116 cancer cell lines (Figure 3.1C). On the contrary, metabolites involved in biosynthetic processes, such as Ala, Ser, Arg, N-A-O (N-Acetylornithine), 5-A-P (5-Aminopentanoate), Thr, Aco and Al-Thr were less abundant in A549 as compared with HCT116 cells (Figure 3.1C). In addition, Volcano Plot algorithm with a cut-off of $P < 0.005$ and fold change (FC) > 2 highlighted the abundance of metabolites: G6P, myo-In, Aco and Lac significantly differed between A549 and HCT116 cancer cells (Figure 3.1C, lower right panel). Moreover, metabolic profiling comparison between lung cancer cell lines (A549-K-Ras mutated and HCC78-Ros1 mutated) identified in A549 significantly larger intracellular relative abundance of Glc, Gln, Glu and Akg, as well as metabolites involved in amino acids metabolism, such as Gly, Lys, Thr, Met, Thr, Spd, Met and Trp (Figure 3.S1E). In opposite way, decreased levels of metabolites such as: Cit, Fum, Mal and Ala (Figure 3.S1E), further suggested a higher activation of glycolysis in A549 as compared to HCC78 lung cancer cells.

These findings, indicating a more sustained glucose utilization to lactate in A549 lung cancer cells and a higher TCA cycle

intermediates levels in HCT116 colon cancer cells, prompted us to perform metabolomic pathways identification using uniformly labelled glucose ([U-$^{13}C_6$]-Glucose) and glutamine ([U-$^{13}C_5$]-Glutamine) stable isotope tracers. A high M6 labelling of G6P and F1,6BP, as well as M3 labelling of Pyr and Lac, was observed using [U-$^{13}C_6$]-Glucose (Figure 3.1D, blue dots) confirming the high glycolytic activity of both lung and colon cancer cells (Figure 3.1D, blue and red bars). At the same time, higher M3-Ala and M2-Cit labelling (using labelled Glc) indicated that HCT116 colon cancer cell line had a higher conversion rate of glucose via TCA cycle than A549 lung cancer cells (Figure 3.1D, blu dots and red bars). In addition, we found higher levels of M3/M5-Cit and M3-Asp, indicating that glucose entry into TCA cycle via pyruvate carboxylase (PC) converts M3-Pyr into M3-Oaa which either condenses with acetyl-CoA to produce M3- and M5-Cit or generates M3-Asp via transaminase (Figure 3.1D, blu dots and red bars). In parallel analysis, the glutamine contribution to TCA cycle metabolite pools was estimated using [U-$^{13}C_5$]-Glutamine isotope tracer (Figure 3.1D, violet dots) and its conversion to M5-Glu, M5-AKG, M4-Cit (Figure 3.1D, lilac and violet bars), M4-Fum and M4-Mal (Figure 3.S1F). The relative isotope abundances indicated that both human cancer cells preferentially use glutamine into TCA cycle by canonical forward oxidative reaction (Figure 3.1D, lilac and violet bars and S1F). Additionally, the higher labelling of M5-Cit, M3-Mal and M3-Asp found in A549, as compared to HCT116 cells, confirmed the glutamine reductive

carboxylation reaction, as previously reported in lung cancer cells (Metallo et al., 2011).

Taken together, A549 lung cancer cell and HCT116 colon cancer cells used nutrients in a slightly different way and suggested that A549 lung cancer cells, generating notoriously poorly vascularized tumours, displayed a perfect decoupling of nutrients in which glucose was converted to lactate and glutamine used to maintain TCA cycle metabolite pool and sustain anabolic processes. On the other hand, HCT116 colon cancer cells, known to generate more vascularized tumours, are able to use glucose and glutamine in a complementary and mutually reinforcing manner to sustain enhanced growth. Hence, to test whether differential utilization of glucose and glutamine in A549 lung cancer cells and HCT116 colon cancer cells could be the result of their different mitochondrial activity, we measured the oxygen consumption rate (OCR) (Figure 3.1E). Consistently with our hypothesis, we observed that HCT116 colon cancer cells showed higher levels of basal oxidative phosphorylation (OXPHOS, indicated by OCR) than A549 lung cancer cells (Figure 3.1E). However, the lower basal and maximal mitochondrial respiration of A549 cells was not due to mitochondrial dysfunction, as confirmed by the higher ATP production levels in lung cancer cells (Figure 3.S1G -left panel-), as compared to colon cancer cells, and unchanged ROS levels between two cell lines (Figure 3.S1G-right panel-).

Therefore these results indicate that oncogenic K-Ras mutations greatly alter glucose and glutamine utilization to support enhanced growth, but with a distinctive difference in using same nutrients.

3.3.2 Differences of in vitro sensitivity of human cancer cells to BKM120 and CB-839 drugs able to inhibit cancer metabolic rewiring

Consistently with ability of tumour cells to carry out a metabolic switching from glucose to glutamine and vice versa in accordance with the environmental context (Davidson et al., 2016), we chose BKM120 reported to inhibit PI3K and aldolase activity (Hu et al., 2016), and CB-839 as glutaminase inhibitor (Gross et al., 2014) to assess their isolated or combined effects in our cellular models (Figure 3.2A). Following dose-response curves for BKM120 (Figure 3.S1H -left panel-) and CB-839 (Figure 3.S1H –right panel-) to select appropriate concentrations, all three cancer cell lines showed significant aldolase activity reduction by BKM120 and glutamate production was strongly inhibited by CB-839, in agreement with the known mechanism of action of the two drugs (Figure 3.2B, 3.2C, S1I and S1J).

To further test the efficacy of treatments, we performed prolonged proliferation curves under either BKM120 or CB-839 in single treatments, or in combination, BKM120 plus CB-839 (Figure 3.2D, 3.2E and S1K). Specifically, A549 lung cancer cells showed a larger decrease of cell number when grown under prolonged single treatment with CB-839 than under BKM120 (Figure 3.2D, left panel, light blue and green colours, respectively). Instead, we observed an increased reduction of proliferation in HCT116 grown under prolonged single treatment with BKM120, rather than with

CB-839, which showed not significant changes as compared to CTR (Figure 3.2D, right panel). A growth behaviour similar to HCT116 was observed in HCC78-Ros1 lung cancer cells, which showed growth reduction under BKM120 treatment, but not with CB-839 (Figure 3.S1K), perhaps due to significantly higher autophagy mechanism activated in HCT116 and HCC78 under BKM120 treatment, as compared to CB-839 and control (CTR) (Figure 3.S1L). Moreover, a dramatic reduction of cell proliferation was observed in all cellular models under combinatorial BKM120 plus CB-839 treatment, as compared to CTR (Figure 3.2D, 3.2E and S1K, blue color), suggesting a synergic effect of the combined treatment in reducing cell viability. Furthermore, the merge statistical analysis of metabolic profiling in A549 cancer cells revealed similar metabolic signatures in CB-839 alone and in combinatorial BKM120 plus CB-839, as opposed to CTR and BKM120 alone (Figure 3.2 F, left upper panel). In particular, the significant higher level of metabolites such as: G6P, F6P, G1P, 6P-GL, R5P, X5P, N-A-Glc-N-1P and N-A-Glc-N-6P (Figure 3.2F, left panel, and S2A), involved in first step of glycolysis, pentose phosphate pathway (PPP) and amino sugar metabolism (Figure 3.2F, left lower panel) suggested an attempt to activate alternative glucose-dependent pathways in ROS stressed A549 (Figure 3.S2B) under combined treatment, as compared to CTR. This stress was further reinforced due to decreased levels of Gln, Glu, 5-Oxo and All-Cys involved in glutathione metabolism (Figure 3.2F, left panel).

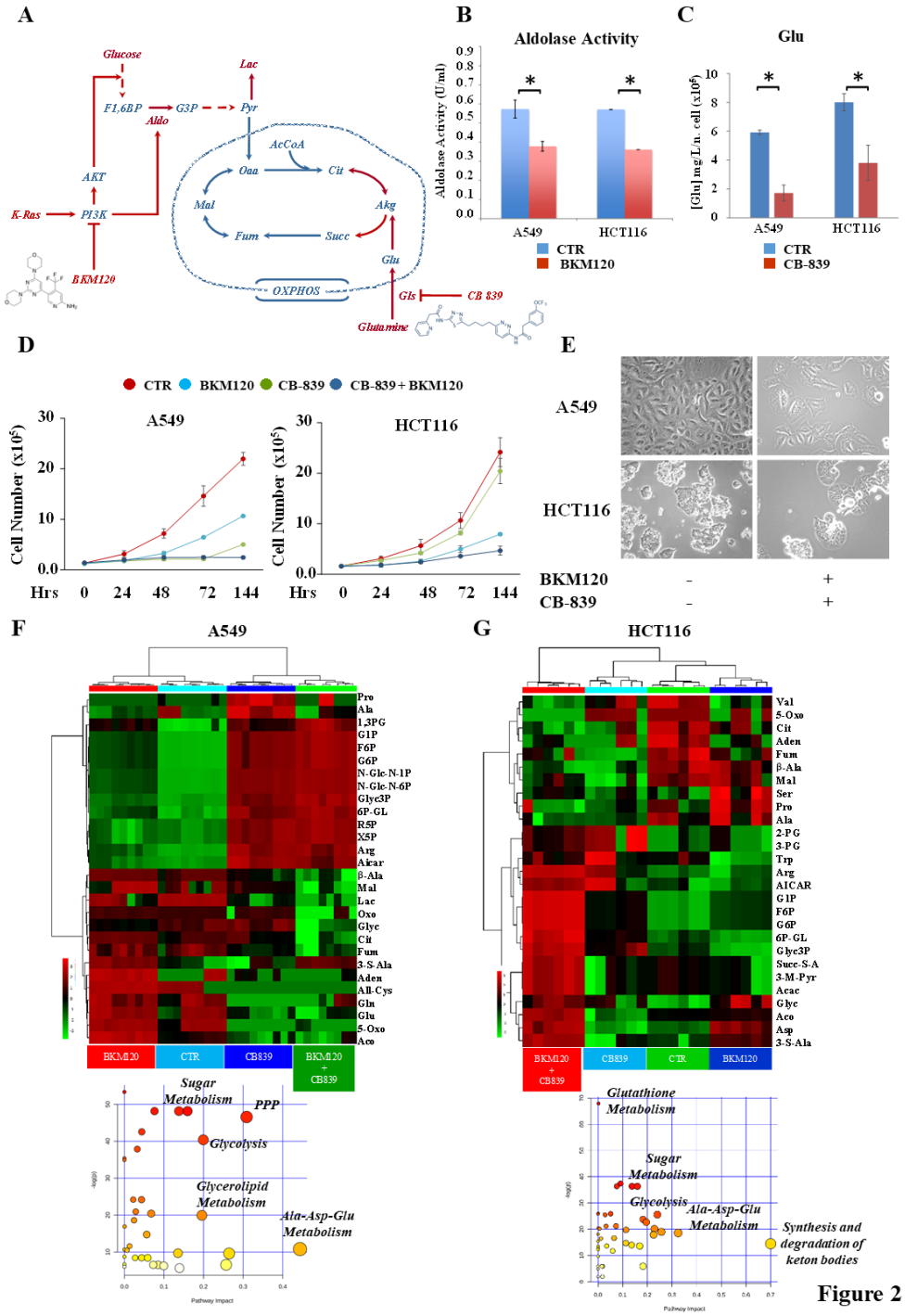
A
Glucose
F1,6BP
G3P
Pyr
Lac
Aldo
AcCoA
Oaa
Cit
AKT
Mal
Akg
K-Ras
PI3K
Fum
Succ
Glu
BKM120
OXPHOS
Gls
CB 839
Glutamine
B
Aldolase Activity
Aldolase Activity (U/ml)
A549
HCT116
CTR
BKM120
C
Glu
[Glu] mg/L.n. cell (x10⁶)
A549
HCT116
CTR
CB-839
D
CTR
BKM120
CB-839
CB-839 + BKM120
A549
HCT116
Cell Number (x10⁵)
Hrs
0
24
48
72
144
E
A549
HCT116
BKM120
CB-839
F
A549
Pro
Ala
1,3PG
G1P
F6P
G6P
N-Glc-N-1P
N-Glc-N-6P
Glyc3P
6P-GL
R5P
X5P
Arg
Aicar
β-Ala
Mal
Lac
Oxo
Glyc
Cit
Fum
3-S-Ala
Aden
All-Cys
Gln
Glu
5-Oxo
Aco
BKM120
CTR
CB839
BKM120 + CB839
Sugar Metabolism
PPP
Glycolysis
Glycerolipid Metabolism
Ala-Asp-Glu Metabolism
G
HCT116
Val
5-Oxo
Cit
Aden
Fum
β-Ala
Mal
Ser
Pro
Ala
2-P G
3-P G
Trp
Arg
AICAR
G1P
F6P
G6P
6P-GL
Glyc3P
Succ-S-A
3-M-Pyr
Acac
Glyc
Aco
Asp
3-S-Ala
BKM120 + CB839
CB839
CTR
BKM120
Glutathione Metabolism
Sugar Metabolism
Glycolysis
Ala-Asp-Glu Metabolism
Synthesis and degradation of keton bodies

Figure 2

Figure 3.2. Combinatorial glycolysis and glutamine metabolism drugs induce growth arrest in A549 and HCT116 human cancer cell lines

(A) Schematic representation indicating pharmacological targets of major substrate metabolic pathways for K-Ras cancer cells. Dashed arrows represent reactions consisting of multiple steps.

(B) Aldolase activity of A549 (■) and HCT116 (■) cancer cells under 1μM BKM120 for 48h.

(C) Glutamate production of A549 (■) and HCT116 (■) under 50nM CB-839 for 48h.

(D) Proliferation curve of A549 (left panel) and HCT116 (right panel) incubated with BKM120 (■), CB-839 (■) or BKM120 + CB-839 (■) and CTR (■) collected and counted at indicated time points.

(E) Morphological analysis of A549 and HCT116 treated with BKM120 + CB-839.

(F and G) Untargeted metabolic analysis of A549 and HCT116 cancer cell. Hierarchical clustering heatmaps show significantly ($p \leq 0.05$) different intracellular metabolites in the four experimental conditions by LC-MS and GC-MS. Enriched metabolic pathways were ranked according to their FDR values calculated by the MetPa method implemented in MetaboAnalyst 4.0 software. The most significant pathways combined treatment compared to CTR (F and G lower panel) were represented by both the bigger/red dots and by those dots with higher log p value. The pathway impact is calculated as the sum of the importance measures of the matched metabolites normalized by the sum of the importance measures of all metabolites in each pathway.

Consistently with the drop of enhanced proliferation and the results described above, we observed a significant decrease of metabolites involved in nucleotide metabolism and in the TCA cycle (Figure 3.2F and S2A). A less relevant effect of combined treatment was observed in HCT116 and HCC78 human cancer cells metabolic profiling (Figure 3.2G, S2C and S2E). Similar to A549, the merge statistical analysis of metabolomics datasets showed a significant increase of metabolites involved in glycolysis and decreased levels of metabolites involved in TCA

cycle metabolism under combined treatment and CB-839 alone as compared to BKM120 single treatment and CTR (Figure 3.2G and S2C). In addition, we observed that HCT116 treated with combined drugs showed a remarkable increase of metabolites, such as: Succ-S-A (Ala, Asp and Glu metabolism) able to generate succinate which could enter the TCA cycle, 3-M-Pyr involved in tryptophan metabolism, Acac involved in keton bodies metabolism and able to promote Mek-Erk signalling (Kang et al., 2015), and 3-S-Ala involved in taurine and hypotaurine metabolism (Figure 3.3 F, upper and lower panels). The activation of the latter unusual metabolic pathway (taurine and hypotaurine metabolism) with antioxidant action (Huang et al., 2016) could probably protect HCT116 cancer cells from the significant increased level of ROS generated by combined drugs treatment (Figure 3.S2D).

3.3.3 Metabolic pathways identification and metabolic flux analysis (MFA) to assay combinatorial drugs treatment responses in A549 and HCT116 cancer cells

To have more information on the impact of drugs treatment on A549 and HCT116 cancer cells metabolism and their ability to activate alternative metabolic pathways, we performed ^{13}C and 15N stable-isotope tracing and mass spectrometry analysis. As expected, using [U-$^{13}C_6$]-Glucose (Figure 3.S3A, blue dots) we did not observe changes between CTR and treatments with

individual and combined drugs in G6P and F1,6BP labelling, involved in the first part of glycolysis (Figure 3.S3A and S3B). We found, instead, a significant decreased labelling in metabolites such as: M3-Pyr, M3-Lac, M3-Ala and M2-Cit in the combinatorial treatment and in CB-839-treated cells as compared to BKM120 and CTR (Figure 3.S3A and S3B). In addition, this analysis identified significant increased levels of M4-Akg and M4-Asp, but not of M4-Fum and M4-Mal, obtained from second turn (dark blue dots) of TCA cycle, in A549 under combined treatment and in CB-839-treated cells (Figure 3.S3A, S3B and S3C), as opposed to M2-Akg and M3-Asp (M3-Asp was generated by glucose via PC, as described above) labelling observed in A549 CTR and under BKM120 treatment (Figure 3.S3A and S3C).

In addition, using [U-$^{13}C_5$]-Glutamine (Figure 3.3C, violet dots) we observed the significant lower levels of M5-Glu, M5-Akg, M4-M5-Cit and M3-M4-Asp labelling from [U-$^{13}C_5$]-Glutamine tracer (Figure 3.S3A -violet dots-) were indicative of decreased glutamine oxidation into TCA cycle under combined treatment and CB-839 alone, as compared to CTR and single BKM120 (Figure 3.S3A and S4B), confirming the in vitro efficacy of the inhibitors (Rahman and Hasan, 2015).

To better characterize the metabolic response to combinatorial drugs treatment effectiveness, we employed ^{13}C Metabolic Flux

Analysis (MFA) approach to quantify fluxes comparing control and combinatorial drugs treatment conditions.

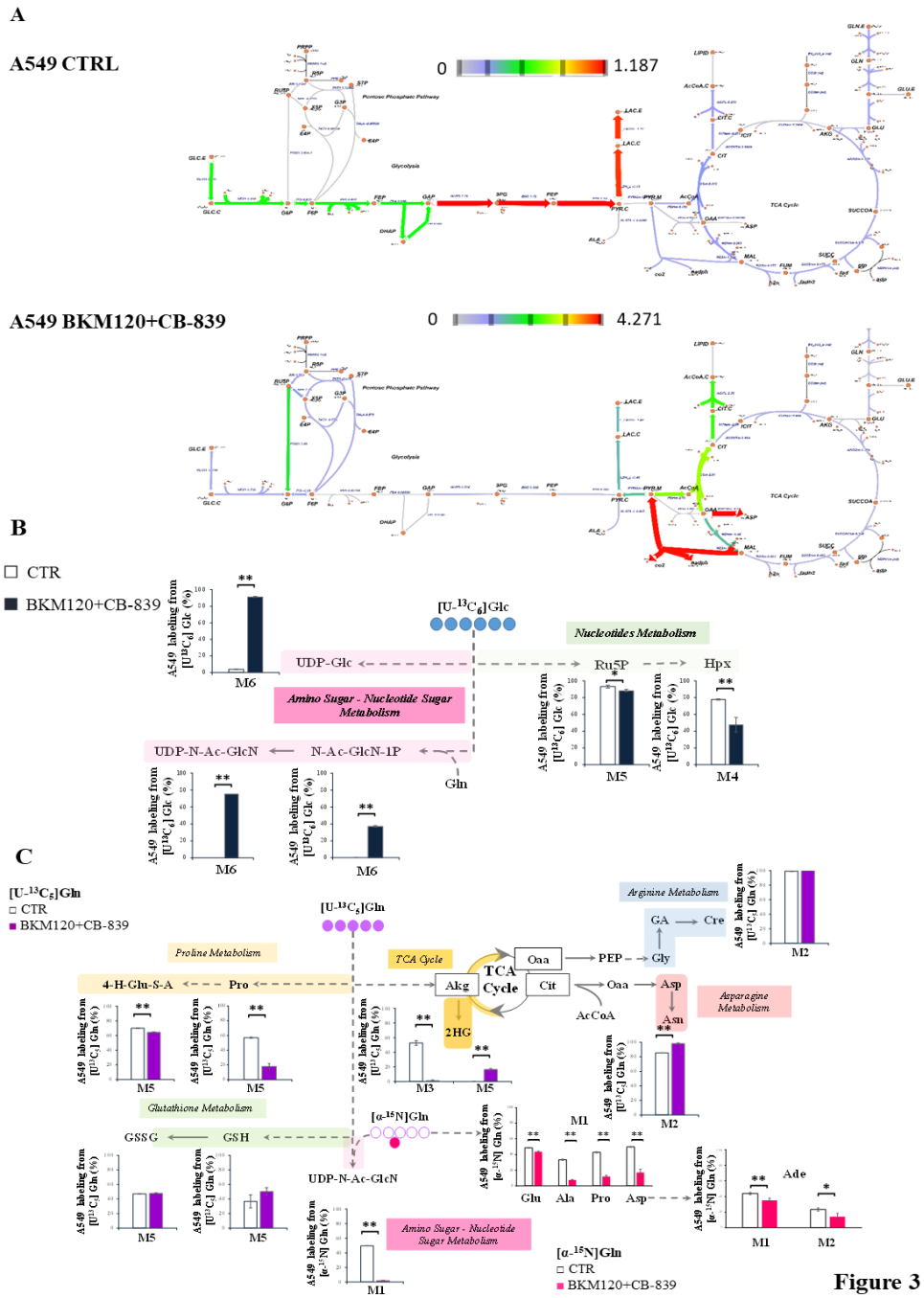

Figure 3

Figure 3.3. Metabolic flux analysis of A549 lung cancer cells under combinatorial drug treatments

(A) Schematic of central carbon metabolism with net flux values estimated by ^{13}C MFA for A549 cancer cells CTR and under BKM120 plus CB-839 treatments. Arrows colors (red color up flux and violet low flux) and the thickness represent the significantly different fluxes (based on 95% confidence intervals).

(B) Schematic representation and percentage isotope labelling enrichment of metabolites from [U-$^{13}C_6$]-Glucose in A549 cancer cells.

(C) Schematic representation and percentage isotope labelling enrichment of metabolites from [U-$^{13}C_5$]-Glutamine and [$\alpha^{15}N$]Gln in A549 cancer cells.

Flux estimations through the metabolic network was carried out using elementary metabolite unit (EMU)-based algorithm and its associated confidence intervals by assessing flux fit sensitivity to minor flux deviations listed in Supplementary Table 1, and the full dataset and model description are provided in Supplementary information and Supplementary Figures S3D.

These data indicated that combinatorial drugs treatment induced a significant decreased glycolytic flux as well as reduced flux of glutamine oxidation via TCA cycle (Figure 3.3A and S3D) confirmed by decreased basal mitochondrial respiration (Figure 3.S3E). Simultaneously, MFA analysis of A549 under combined treatment suggested an attempt to activate alternative glucose-dependent pathways by increased flux of PPP, increased flux of glucose oxidation by TCA cycle through reactions of i) PDH enzyme flux towards ACL, ii) Oaa to Asp flux and iii) Mal to Pyr through malic enzyme (Figure 3.3A).

Deeper isotope labelling analysis, confirmed this attempt of glucose metabolic reprogramming, usually activated in cancer

cells to fulfil anabolic demands (Hay, 2016), in stressed A549 under drugs treatment even through activation of amino sugar metabolism by labelling of M4 UDP-Glc, M6-N-Ac-GlcN-1P and M6-UDP-N-Ac-GlcN (Figure 3.3B pink, and S4A). Moreover, M5-Ru5P (ribulose 5 phosphate) labelling indicated an independent activation of PPP in all conditions, while the significant decrease in A549 under combined treatment and CB-839 of M4-Hpx (hypoxanthine) (Figure 3.3 B and S4A) - involved in nucleotides metabolism (Figure 3.3 B, light green) - was coherent with the reduction of enhanced proliferation as showed in Figure 3.2D.

The glucose metabolic reprogramming observed under drugs treatment prompted us to investigate also the drugs effect on glutamine alternative metabolic activation by [U-$^{13}C_5$]-Glutamine (Figure 3C, violet dots) and [^{15}N]Gln (Figure 3.3C, fuchsia dots) stable isotope tracers. The contribution of glutamine into asparagine and metabolism known to promote, respectively, cancer cell proliferation (Krall et al., 2016) and survival (Kremer et al., 2017) was shown by significant increased labelling in M2 asparagine (Asn) (Figure 3.3C red color) and lack labelling changes in M2-creatinine (Cre) (Figure 3.3C light blue color). Specifically, both metabolites were derived from forward glutamine utilization in the TCA cycle, cleavage of M4-Cit by ATP citrate lyase in M2-labelled Oaa inferred from the labelling of M2-Asn and M4-Oaa catalyzed to PEP by pyruvate carboxykinase (PCK) followed to glycine (Gly) and by glycine amidinotransferase (*AGAT*) and N-guanidinoacetate

methyltransferase (*GAMT*) synthesized in Cre (Figure 3.3C). Moreover, the unaltered glutamine contribution into glutathione metabolism by M2 GSH and GSSG (green color) (Figure 3.3C and S4C) it was also observed. Interestingly, the significant change observed in M2-Asn, M5-Pro and M5 4-hydroxy glutamate semialdehyde (4-H-Glu-S-A) labelling observed in A549 under combined BKM120 plus CB-839 and single CB-839 treatments, as compared to CTR and single BKM120, indicated the involvement of glutamine to proline metabolism (Figure 3.3C, light yellow). Moreover, we observed 2HG accumulation in A549 cells, both CTR and under all treatments, but with different labelling incorporation (Figure 3.3C and S4C). It is well known that 2HG is a typical metabolite accumulated in cancer with IDH1/2 mutations produced through glutamine reductive carboxylation (Dang et al., 2010; Metallo et al., 2011) and linked to epigenetic control because structurally similar to AKG (Ma et al., 2015). Surprisingly, we found M3-2HG labelling in the CTR, derived from forward TCA glutamine utilization, and M5-2HG labelling in A549 under combinatorial treatment (Figure 3.3C). Glutamine is also required for the amino-nucleotides sugar metabolism (pink color), where it donates an amino group to glucose-6-phosphate to produce glucosamine-6-phosphate. M1 UDP-N-Ac-GlcN labelling in A549 under combinatorial treatment and single CB-839 derived from [^{15}N]Gln labelling (Figure 3C, fuchsia dots, and S4D) showed a loss of glucose and glutamine co-ordination during hexosamine biosynthesis, which has been shown to regulate cell growth and proliferation through

glycosylation of signal transduction components (Wellen et al., 2010). We also found significantly lower labelling for some metabolites (such as Glu, Ala, Pro and Asp) in A549 exposed to combined treatment and single CB-839, as compared with CTR and single BKM120 ones (Figure 3.3C and S4D). In addition, the significantly lower labelling on M1 and M2 nucleobase adenine, generated from [α-^{15}N]Gln-derived nitrogen atoms from Asp, found in A549 under BKM120 plus CB-839 compared with CTR and single treatments was consistent with the strong effect of combined treatment on cell proliferation arrest (Figure 3.3C).

In HCT116 colon cancer cells isotope labelling experiments identified a distinctive response from those observed in A549 lung cancer cells, similar but weaker effects, (Figure 3.4 and S5). In fact, using [U-$^{13}C_6$]-Glucose (Figure 3.S5A blue circles) we did not observe changes in G6P and F1,6BP labelling between CTR and all treatments, whereas a significant decreased labelling was detected in M3-Pyr, M3-Lac, M3-Ala and M2-Cit labelling under combinatorial treatment as compared to the others (Figure 3.S5A and S5B). In contrast with A549, HCT116 under combinatorial and single CB-839 treatments displayed significantly higher labelling in M4-Asp derived from a second turn (dark blue circle) of TCA cycle (Figure 3.S5A). It is worth to note that single CB-839 treatment, through a significant M2 Cit, M4 AKG, and M4 Asp labelling, accounted for increased glucose utilization into TCA cycle in order to skip the glutaminase inhibitor effect (Figure 3.S5B).

These results were confirmed by MFA analysis (Figure 3.4A). Specifically, in opposite way to A549, these data indicated that HCT116 under combinatorial treatment showed no significant change in the first step of glycolysis but with significant reduction in the second one (Figure 3.4A). The increased flux of lactate production probably owing to increased flux of Mal to Pyr and sustained by increased glutamine oxidation via TCA cycle (Figure

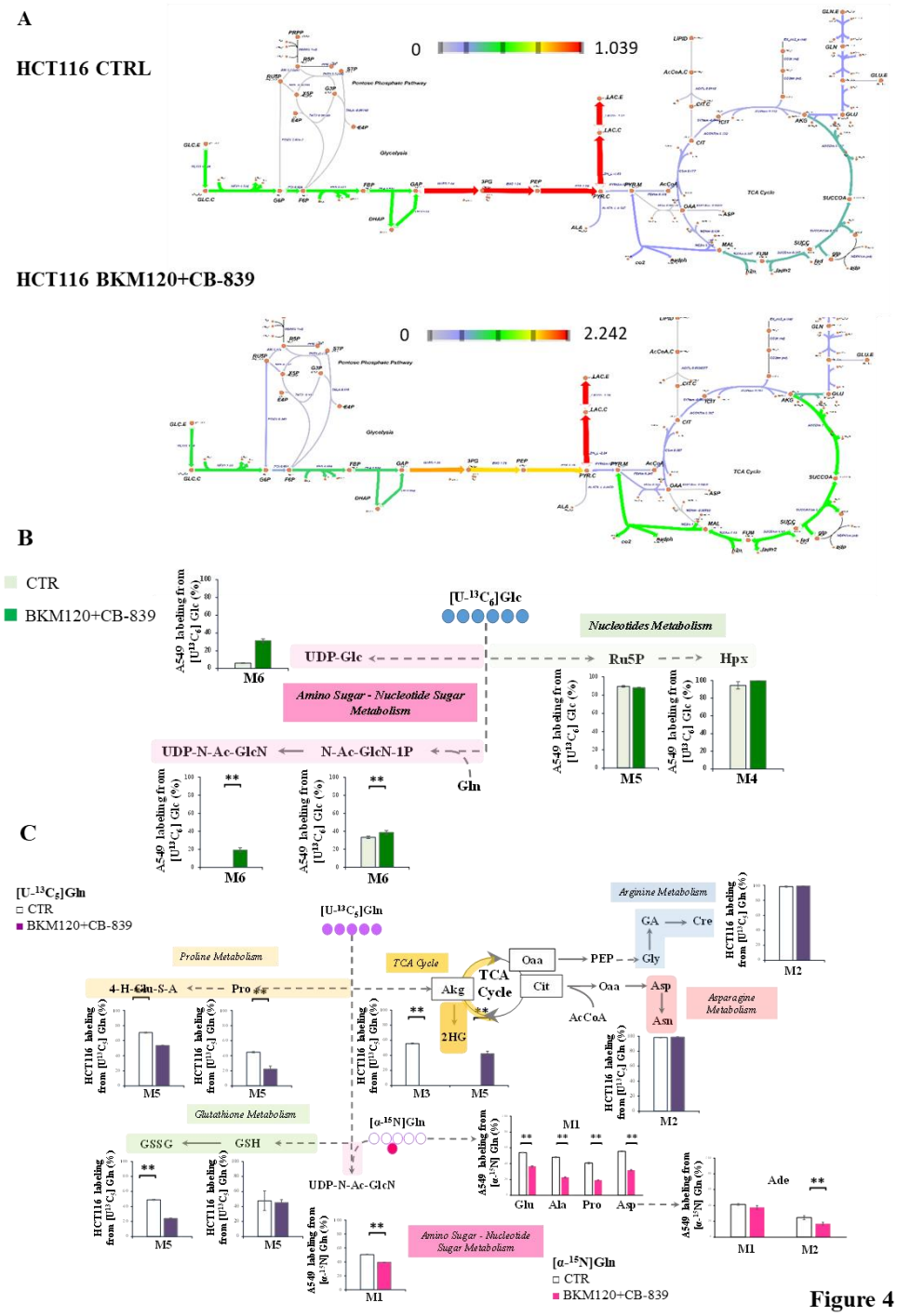
A
HCT116 CTRL
0
1.039
HCT116 BKM120+CB-839
0
2.242
B
CTR
BKM120+CB-839
[U-13C6]Glc
Nucleotides Metabolism
UDP-Glc
Ru5P
Hpx
Amino Sugar - Nucleotide Sugar Metabolism
UDP-N-Ac-GlcN
N-Ac-GlcN-1P
Gln
M6
M5
M4
C
[U-13C5]Gln
CTR
BKM120+CB-839
Arginine Metabolism
GA
Cre
Gly
Proline Metabolism
TCA Cycle
Oaa
PEP
4-H-Glu-S-A
Pro
Akg
TCA Cycle
Cit
Asp
Asn
Asparagine Metabolism
2HG
AcCoA
M2
M3
M5
Glutathione Metabolism
GSSG
GSH
[α-15N]Gln
UDP-N-Ac-GlcN
Glu
Ala
Pro
Asp
Ade
M1
Amino Sugar - Nucleotide Sugar Metabolism
[α-15N]Gln
CTR
BKM120+CB-839

Figure 4

Figure 3.4. Metabolic flux analysis of HCT116 colon rectal cancer cells under combinatorial drug treatments

(A) Schematic of central carbon metabolism with net flux values estimated by ^{13}C MFA for HCT116 cancer cells CTR and under BKM120 plus CB-839 treatments. Arrows colors (red color up flux and violet low flux) and the thickness represent the significantly different fluxes (based on 95% confidence intervals).

(B) Schematic representation and percentage isotope labelling enrichment of metabolites from [U-$^{13}C_6$]-Glucose in HCT116 cancer cells.

(C) Schematic representation and percentage isotope labelling enrichment of metabolites from [U-$^{13}C_5$]-Glutamine and [$\alpha^{15}N$]Gln in HCT116 cancer cells.

4A and S5C), although a decreased basal mitochondrial respiration (Figure 3.S5D). Flux results for HCT116 CTR and under combined BKM120 plus CB-839 treatments are listed in Supplementary Table 2.

In addition, isotope labelling analysis of the alternative glucose-dependent metabolic pathways of HCT116 cancer cells did not show any effect on nucleotides metabolism (Figure 3.4B, light green) between CTR and treatments. Rather, we observed significant lower labelling in M5 Ru5P and M4 Hpx colon cancer cells, confirming the lack of effect by CB-839 single treatment (Figure 3.S5B). In addition, the significant higher labelling M6 UDP-Glc and M6 UDP-N-Ac-GlcN in HCT116 under combined treatment compared to CTR (Figure 3.4B, pink color) confirmed amino sugar metabolism activation, as previously observed in A549 (Figure 3.3B).

Similar to A549, using [U-$^{13}C_5$]-Glutamine tracer (Figure 3.S5A, violet dots) we observed decreased glutamine utilization into TCA cycle under combined treatment, as determined by significant

lower levels of M5 Glu, M5 Akg, M4 and M5 Cit and M3 and M4 Asp labelling in HCT116 under combined treatment and CB-839 (Figure 3.S5A and S6A), and unaltered glutamine contribution into the Asn (red color) and Arg metabolism (blue color), as indicated by not significant labelling in M2 Asn and M2 Cre, (Figure 3.4C and S6B). Interestingly, the significant lower labelling in M5 Pro and 4-H-Glu-S-A and in M5 GSSG (Figure 3.4C), both involved in resistance to oxidative stress, confirmed the significant higher ROS levels detected in HCT116 under combined treatments, as compared to CTR and A549 (Figure 3.S2). Moreover, [U-$^{13}C_5$]-Glutamine C3 2HG labelling in CTR derived from forward glutamine oxidation and C5 2HG labelling (Figure 3.4C), as well as the higher [^{15}N]Gln labelling M1 UDP-N-Ac-GlcN (Figure 3.4C, fuchsia circles) in HCT116 cancer cells under combinatorial treatment, once again confirmed the similar effect of the combinatorial therapy observed in A549 (Figure 3.3), probably due to the stronger link between metabolism and epigenetic machinery used to skip therapy. This weaker but similar effect of combinatorial drugs on HCT116 was further confirmed by decreased labelling in M1 Glu, Ala, Pro and Asp metabolites, as well as by the lack of changes in M1 and M2 adenine labelling, as compared to other treatments (Figure 3.4C and S6C).

Taken together these findings demonstrate that the changes in metabolic fingerprinting observed after drug combinatorial treatment derive from both inhibitory effect specific for each cell type and each drug.

3.3.4 BKM120 and CB-839 combinatorial treatment inhibits A549 and HCT116 tumour growth in mouse xenografts

To finally demonstrate the efficacy of the BKM120 plus CB-839 combined therapy in tumour growth inhibition, we evaluated drug treatments response in a mouse xenograft model obtained with subcutaneous injection of A549 lung cancer cells and in another one obtained with HCT116 colon cancer cells injection (Figure 3.5, 3.6, 3.7 and S7). In accordance with published data, we administered mice xenografts with BKM120 (50 mg/kg) (Alagesan et al., 2015; Alikhani et al., 2013) and CB-839 (200 mg/kg) (Davidson et al., 2016; Gross et al., 2014) in combination. When tumours reached a volume of 130-150 mm3, mice were treated for 15 days with vehicle (CTR) or a combination of BKM120 plus CB-839 (Treat). Mice were monitored for tumour growth using caliper and for glucose metabolism using [^{18}F]FDG-PET scans performed before receiving the therapy (pre-treatment scan), during the therapy and at the end of therapy (Figure 3.5, 3.6 and S7). A549 tumours treated with BKM120 plus CB-839 displayed remarkable tumour growth inhibition during the entire therapeutic window, as determined by significant decreased tumour volume as compared to CTR or BKM120 or CB-839 administered alone, (Figure 3.5A, left panel and 5B) followed by significant lower levels of post mortem tumour weight (Figure 3.S7A) highlighting the synergistic effect of combinatorial treatment.

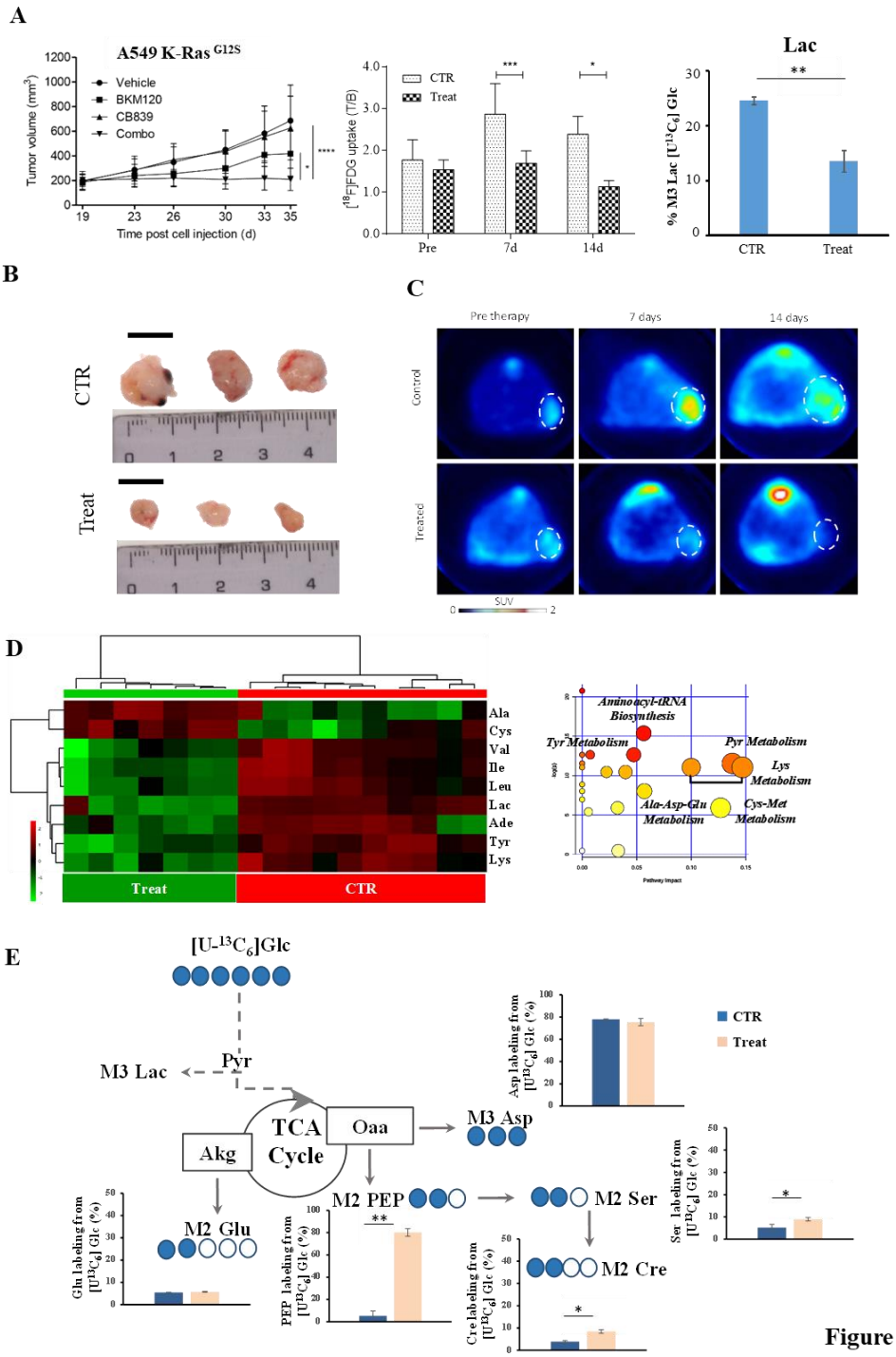
A
A549 K-Ras G12S
Vehicle
BKM120
CB839
Combo
Tumor volume (mm3)
Time post cell injection (d)
CTR
Treat
[18F]FDG uptake (T/B)
Pre
7d
14d
Lac
% M3 Lac [U13C6] Glc
CTR
Treat
B
CTR
Treat
C
Pre therapy
7 days
14 days
Control
Treated
SUV
D
Ala
Cys
Val
Ile
Leu
Lac
Ade
Tyr
Lys
Treat
CTR
Aminoacyl-tRNA Biosynthesis
Tyr Metabolism
Pyr Metabolism
Lys Metabolism
Ala-Asp-Glu Metabolism
Cys-Met Metabolism
Pathway Impact
E
[U-13C6]Glc
Pyr
M3 Lac
TCA Cycle
Oaa
Akg
M3 Asp
M2 PEP
M2 Ser
M2 Glu
M2 Cre
Asp labeling from [U13C6] Glc (%)
Glu labeling from [U13C6] Glc (%)
PEP labeling from [U13C6] Glc (%)
Ser labeling from [U13C6] Glc (%)
Cre labeling from [U13C6] Glc (%)
CTR
Treat

Figure 5

Figure 3.5. Analysis of A549 lung tumours under combinatorial treatment.

(A) Tumour size measured by caliper in mice and when tumours reached a volume of 130-150 mm^3 mice were treated for 15 days with vehicle (CTR) or a combination of BKM120 (50 mg/kg in NMP/PEG300 (10/90, v/v) o.g. daily) plus CB-839 (200 mg/kg dissolved in 25% (w/v) hydroxypropyl-b-cyclodextrin in 10 mmol/L citrate (pH 2.0) o.g. twice daily) (Treat) left panel. -Middle panel- [^{18}F]FDG uptake in A549 tumours exposed to the combinatorial treatment compared to CTR expressed as tumour to background ratio (T/B). -Right panel- Lactate labelling evaluated using [U-$^{13}C_{6.}$]-Glucose infused in A549 xenograft mice exposed to the combinatorial treatment compared to CTR and analyzed by GC-MS.

(B) Post mortem analysis of tumour volume (left panel) of A549 tumours exposed to the combinatorial treatment compared to CTR.

(C) Representative transaxial [^{18}F]FDG PET images of CTRL and combined treatment mice performed before and after drugs administration. Color scale is expressed as SUV value.

(D) Untargeted metabolic analysis of A549 lung adenocarcinoma tumours. Hierarchical clustering heatmap shows significant ($p \leq 0.05$) different intracellular metabolites. Enriched metabolic pathways were ranked according to their FDR values calculated by the MetPa method implemented in MetaboAnalyst 4.0 software. The most significant pathways combined treatment compared to CTR were represented by both the bigger/red dots and by those dots with higher log p value. The pathway impact is calculated as the sum of the importance measures of the matched metabolites normalized by the sum of the importance measures of all metabolites in each pathway.

These results were further confirmed by [^{18}F]FDG-PET scan revealing significant decreased level of [^{18}F]FDG uptake in A549 tumours exposed to the combinatorial treatment compared to CTR (Figure 3.5A, middle panel, and 5C). In addition, considering the valuable role of LDH (lactate dehydrogenase) as a marker in patients with cancer, [U-$^{13}C_6$]-Glucose was infused by repeated injections (Lane et al., 2015) in A549 xenograft mice to evaluate lactate labelling. Consistent with [^{18}F]FDG uptake, we found

decreased lactate labelling in A549 tumours treated with BKM120 plus CB-839, as compared to vehicle (Figure 3.5A, right panel). Furthermore, post mortem untargeted metabolic profiling identified a significant decreased relative abundance of metabolites involved in amino acids metabolism (Lys metabolism, Tyr metabolism, Ala-Asp-Glu metabolism, Pyr metabolism), except for Ala and Cys, that showed higher levels in A549 treated tumours, compared to vehicle (Figure 3.5D). In addition, by uniformly labelled [U-$^{13}C_6$]-Glucose administration no significant M3-Asp labelling and significant M2-Glu, M2-PEP, M2-Ser and M2-Cre was observed in A549 tumours treated and vehicle (Figure 3.5E),

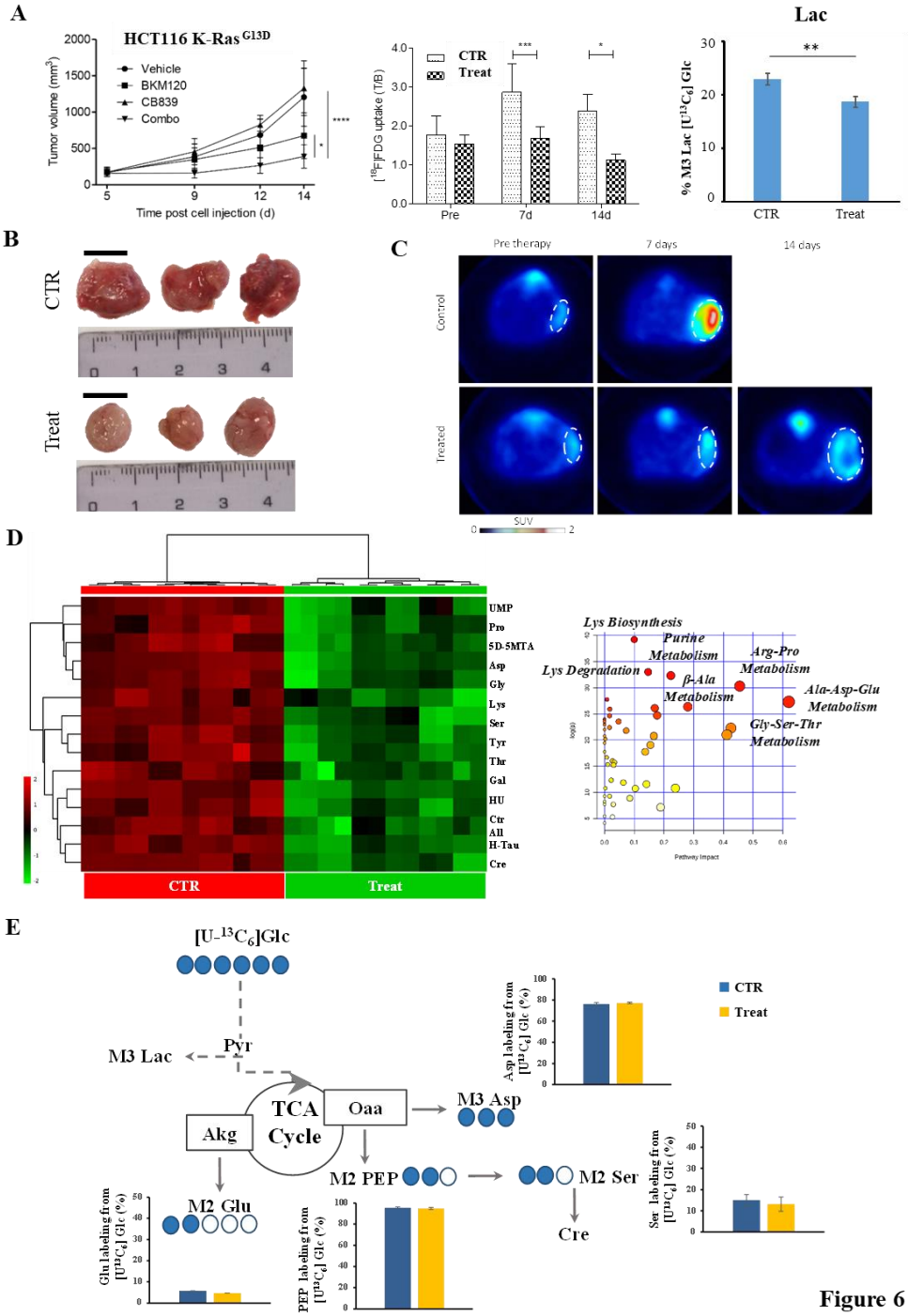
A
HCT116 K-Ras G13D
Vehicle
BKM120
CB839
Combo
Tumor volume (mm³)
Time post cell injection (d)
CTR
Treat
[18F]FDG uptake (T/B)
Pre
7d
14d
Lac
% M3 Lac [U-13C6] Glc
CTR
Treat
B
CTR
Treat
C
Pre therapy
7 days
14 days
Control
Treated
SUV
D
UMP
Pro
5D-5MTA
Asp
Gly
Lys
Ser
Tyr
Thr
Gal
HU
Ctr
All
H-Tau
Cre
CTR
Treat
Lys Biosynthesis
Purine Metabolism
Lys Degradation
Arg-Pro Metabolism
β-Ala Metabolism
Ala-Asp-Glu Metabolism
Gly-Ser-Thr Metabolism
Pathway Impact
E
[U-13C6]Glc
M3 Lac
Pyr
TCA Cycle
Oaa
M3 Asp
Akg
M2 PEP
M2 Ser
Cre
M2 Glu
CTR
Treat
Asp labeling from [U13C6] Glc (%)
Glu labeling from [U13C6] Glc (%)
PEP labeling from [U13C6] Glc (%)
Ser labeling from [U13C6] Glc (%)

Figure 6

Figure 3.6. Analysis of HCT116 colon rectal tumours under combinatorial treatment.

(A) Tumour size measured by caliper in mice and when tumours reached a volume of 130-150 mm^3, mice were treated for 15 days with vehicle (CTR) or a combination of BKM120 (50 mg/kg in NMP/PEG300 (10/90, v/v) o.g. daily) plus CB-839 (200 mg/kg dissolved in 25% (w/v) hydroxypropyl-b-cyclodextrin in 10 mmol/L citrate (pH 2.0) o.g. twice daily) (Treat) left panel. -Middle panel- [^{18}F]FDG uptake in HCT116 tumours exposed to the combinatorial treatment compared to CTR expressed as tumour to background ratio (T/B). -Right panel- Lactate labelling evaluated using [U-$^{13}C_6$]-Glucose infused in HCT116 xenograft mice exposed to the combinatorial treatment compared to CTR and analyzed by GC-MS.

(B) Post mortem analysis of tumour volume (left panel) of HCT116 tumours exposed to the combinatorial treatment compared to CTR.

(C) Representative transaxial [^{18}F]FDG PET images of CTRL and combined treatment mice performed before and after drugs administration. Color scale is expressed as SUV value.

(D) Untargeted metabolic analysis of HCT116 colon rectal tumours. Hierarchical clustering heatmap shows significantly ($p \leq 0.05$) different intracellular metabolites. Enriched metabolic pathways were ranked according to their FDR values calculated by the MetPa method implemented in MetaboAnalyst 4.0 software. The most significant pathways combined treatment compared to CTR were represented by both the bigger/red dots and by those dots with higher log p value. The pathway impact is calculated as the sum of the importance measures of the matched metabolites normalized by the sum of the importance measures of all metabolites in each pathway.

highlighting the glucose carbon contribution via TCA cycle to support cancer cell proliferation in tumour-bearing animals.

Finally, to sustain the value of the therapy, we tested the hepatotoxicity of drugs by assessing aspartate transaminase (*GOT*) and alanine transaminase (*GPT*) activity, notoriously used as indicators of healthy and diseased states in patients (Figure 3.7A). In addition to lack of significant weight changes between Treat

and CTR, we did not find significant differences in transaminases activity between A549 Treat and CTR (Figure 3.S7B and 3.7A).
A similar trend has been observed in HCT116 tumour-bearing mice that showed significant regression of tumour volume during the therapeutic window (Figure 3.6A, left panel and 3.6B) and post mortem tumour weight (Figure 3.S7C), as well as significant decreased levels of [^{18}F]FDG uptake and [U-$^{13}C_6$]-Glucose lactate labelling under combinatorial treatment, as compared to vehicle (Figure 3.6A middle and right panel, and 3.6C). Nevertheless, as we found a significant effect of the combinatorial treatments in HCT116 xenograft mice, we confirmed in vivo the lower efficacy of BKM120 plus CB-839 combinatorial therapy in HCT116 tumours, as compared to A549 (Figure 3.5 and 3.6). The similar effect has been confirmed by post mortem untargeted metabolic profiling revealing a significant decreased relative abundance of metabolites involved in amino acids and nucleotides metabolism observed in treat HCT116 tumours as compared to CTR (Figure 3.6D, left and right panels). It was also interesting to note the similar stable isotope-labelled metabolite profiling of M3-Asp, M2-Glu, M2-PEP, M2-Ser and M2-Cre labelling using [U-$^{13}C_6$]-Glucose isotope tracer in HCT116 tumours (Figure 3.6E) observed in A549 (Figure 3.5E) above described, although coming from different origin tissues. Finally, we also tested hepatotoxicity of drugs by GOT and GPT activity and we observed a slight hepatic stress, but not toxic effect in treated HCT116 tumours as compared to CTR (Figure 3.7C). Unlike to that observed in A549, we noticed a significant weight difference in treated animals compared to

CTR suggesting a possible search of treatment related-alternative sources for tumour progression (Figure 3.S7D).

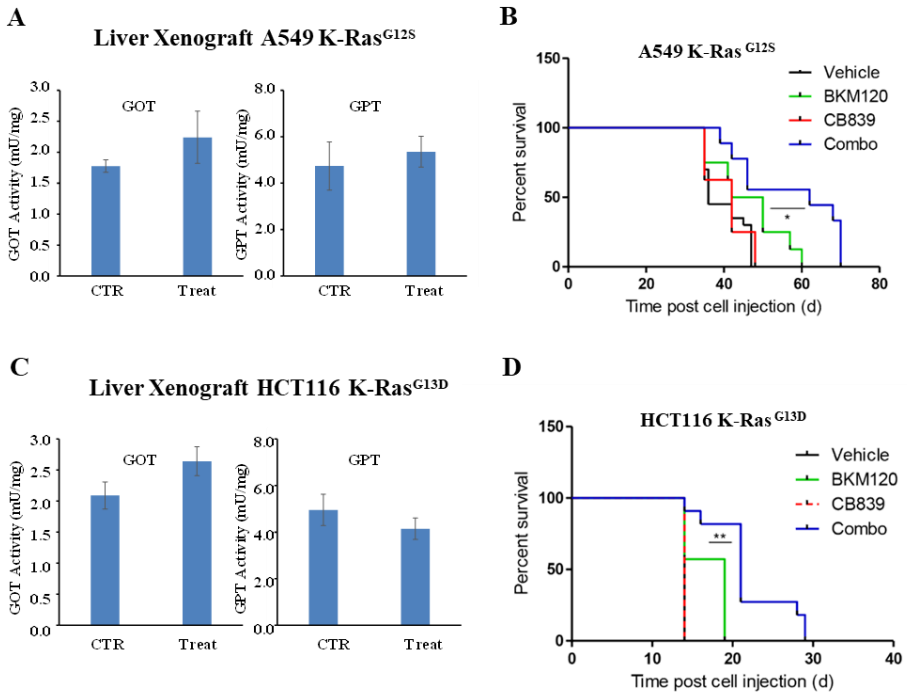

Figure 3.7. Analysis of toxicity and prolonged therapeutic responses in A549 and HCT116 tumours under combinatorial treatment.

(A) Evaluation of hepatotoxic effect of drugs by assessing aspartate transaminase (GOT) and alanine transaminase (GPT) (right panel) of A549 liver mice exposed to the combinatorial treatment compared to CTR.

(B) Kaplan–Meier survival curves of A549 lung tumour bearing mice. Combined treatment significantly increased survival compared to BKM120 alone ($p < 0.05$).

(C) Evaluation of hepatotoxic effect of drugs by assessing aspartate transaminase (GOT) and alanine transaminase (GPT) (right panel) of HCT116 liver mice exposed to the combinatorial treatment compared to CTR.

(D) Kaplan–Meier survival curves of HCT116 colon rectal tumour bearing mice. Combined treatment significantly increased survival compared to BKM120 alone ($p < 0.01$). E

Further groups of A549 and HCT116 tumours bearing mice were treated with the combination of BKM120 and CB-839 or vehicle to monitor survival. The combination of the two drugs significantly increased survival of both tumour models (Figure 3.7B
and D): in detail median survival of HCT116 tumour bearing mice raised from 14 to 21 days ($p < 0.0001$) and that of A549 tumour bearing mice from 36 to 62 days ($p < 0.01$). These data confirmed the lower efficacy of the combined treatment on HCT116 tumour than on A549 and consequently the capability of HCT116 tumour to use other sources of energy.

3.4 DISCUSSION

Herein, we demonstrate a large variability of the metabolism in A549 lung K-RasG12S and HCT116 colon K-RasG13D human cancer cells and substantial differences in metabolic profiling and flux determination after individual and combined drug treatment in vitro and in vivo. In fact, despite untargeted metabolic profiling showed similar statistical PCA analysis for A549 lung and HCT116 colon cancer cells grown in vitro, the two cell lines harboring a K-Ras activated oncogene, showed profound differences in nutrients utilization (Figure 3.1) and drugs sensitivity (Figure 3.2). In A549 lung cancer cells most of glucose was converted to lactate and alanine via PC, CB-839 strongly inhibited cell growth and profoundly affects metabolic profiling (Davidson et al., 2016) while BKM120 was almost ineffective (Figure 3.1 and 3.2). In the opposite way, HCT116 colon cancer cells showed glucose contribution both to the TCA cycle and in lactate production, CB-839 was almost ineffective on cancer cell growth but showed detectable changes in metabolic profiling and BKM120 inhibited cancer cell growth but showed lower significant changes in metabolic profiling (Figure 3.1 and 3.2). This metabolic difference can be due to the presence of a mutation (H1047R) in the catalytic domain of PIK3CA gene in HCT116 cells (Samuels et al., 2005). This mutation in catalytic domain leads to the constitutive kinase activation that induce hyperactivity

of downstream signalling related with proliferative cues. Consistently with our metabolic results, it has been observed that PIK3CA mutant cell lines showed enhanced glucose metabolism followed by higher lactate levels and mitochondrial TCA cycle enzyme 2-oxoglutarate dehydrogenase (OGDH) activity was required to ensure both enhanced cell proliferation in culture and tumour maintenance in vivo as compared to PIK3CA wild type (WT) cells (Ilic et al., 2017).

Of interest it was the identification of PPP, amino sugars and nucleotides alternative metabolic pathway activation from glucose utilization (Figure 3.3 and 3.4), possibly to residually sustain growth under combinatorial drugs treatment. Moreover, the significant increased Asp labelling, as preserving mechanism, observed using both ^{13}C stable isotope tracers in both human cancer cell lines (Figure 3.S3 and S5) could be used as asparagine substrate to sustain ASCT2 (Slc1a5) antiport with glutamine allowing the net entry of 1–2 carbon atoms into the cell and oxidized in the TCA cycle to produce ATP (Scalise et al., 2017). This glucose metabolic reprogramming, as well as the metabolic defect observed in 2HG production (Figure 3.3C and 3.4C) from glutamine observed under drugs treatments, can explain how cancer metabolic rewiring contributes to tumour epigenetic alterations, thereby affecting cancer therapeutic responses. Furthermore, lung A549 cancer cells showed increased arginine, asparagine and proline labelling from glutamine (Figure 3.3) known to be involved in survival, enhanced proliferation (Elia et al., 2017; Krall et al., 2016; Kremer et al., 2017). These findings

may shed new light on the involvement of altered metabolism of glucose and glutamine, with a variety of alternative pathways, we observed on TGCA expression data for lung and colon adenocarcinoma patients (Figure 3.S7E and F).

The interesting findings reported in this paper is the synergic antitumour effect of BKM120 and CB-839 combined treatment both in A549 lung cancer cells (Figure 3.5) and in HCT116 colon cancer cells xenografts (Figure 3.6). We observed significant tumour reduction and prolonged therapeutic responses in mice correlated with reduced 18F-FDG uptake seen in both A549 K-RasG12S lung (Figure 3.5) and HCT116 K-RasG13D colon xenografts (Figure 3.6). Noteworthy, the combination of BKM120 and CB-839 metabolic inhibitors in A549 K-RasG12S and HCT116 K-RasG13D xenografts mice induced severe energetic stress and metabolic crisis, which resulted in significant tumour growth regression (Figure 3.5, 3.6 and 3.7) without toxicities association (Figure 3.7). In addition, uniformly labelled [U-$^{13}C_6$]-Glucose in vivo administration confirmed the glucose carbon contribution via TCA cycle to support cancer cell proliferation in tumour-bearing animals (Figure 3.5 and 3.6) (Davidson et al., 2016). However, in vitro as well as in vivo findings showed a better clinical response A549 to combinatorial therapy in comparison with HCT116 suggesting that the concomitant mutation in PIK3CA gene could influence metabolic dependency and treatment sensitivity. In fact, Maira et al. (Maira et al., 2011) showed that cells expressing both *KRAS* and *PI3Kα* mutations displayed a lower sensitivity to BKM120 in comparison with

PI3Kα mut/KRAS WT. The authors suggested that the reduced effect in double mutants was related with the activation of alternate K-Ras dependent signalling pathways such as the extracellular signal-regulated kinase (*ERK*) which is not modulated by BKM120 administered alone (Hong et al., 2016). In our case the administration of a glutaminase inhibitor seems to partially overcome the activation of alternate *K-Ras* dependent signalling pathways induced by the double mutation.

Taken together the findings show that combinatorial drug treatment reduce the growth of tumour xenografts and support the notion that cancer metabolic fingerprint may be useful to select combined precision treatment in a clinical trial setting. Moreover, the utilization of predicting models of CMR (Damiani et al., 2017; Liberti et al., 2017) which have been able to shed light on the logic of metabolic rearrangement, may contribute to open the way to a systems metabolomics led drug treatment and discovery.

3.5 MATERIALS & METHODS

3.5.1 Cell culture

A549 cell line was routinely grown in Dulbecco's modified Eagle's medium (DMEM) containing 4mM L-glutamine, supplemented with 10% fetal bovine serum. HCT116 cell line was grown in DMEM containing 4mM L-glutamine, supplemented with 10% newborn calf serum. HCC78 cell line was grown in Roswell Park Memorial Institute (RPMI) 1640 medium containing 2mM L-glutamine, supplemented with 10% fetal bovine serum. All the media were supplemented with 100 U/ml penicillin and 100 mg/ml streptomycin and the cells were incubated at 37 °C in a 5% CO2 incubator. All reagents for media were purchased from Life Technologies (Carlsbad, CA, USA).

3.5.2 Mice experiments

Mice chosen for these studies are 7/8-weeks old nu/nu female mice (Envigo RMS S.r.l. Italy). Animals were kept under specific pathogen free conditions and experiments were carried out in compliance with institutional guidelines for the care and the use of experimental animals, which have been notified to the Italian Ministry of Health and approved by the Ethics Committee of the IRCCS San Raffaele Scientific Institute of Milan.

3.5.3 Method Details

Cell proliferation analysis and cell treatments
Cells were plated in 6-well plates in normal growth medium.

For the proliferation curves in nutrients deprivation conditions, culture medium was replaced after 18 hours with a normal medium, a low glutamine medium (0.5mM glutamine) or a low glucose medium (1 mM glucose). The cells were collected and counted after 24, 48, 72 and 144 hours.

For the dose-response curves, cells were treated with the indicated amounts of CB-839 (MedChem Express) and BKM120 (Selleck Chemicals) for 48 hours and then counted. Data are expressed as percentage of survival with respect to the control condition (normal growth medium).

For the proliferation curves in the presence of the drugs, cells were treated with 50nM CB-839 and/or 1 µM BKM120 for 24-48-72-144 hours and then counted.

3.5.4 Metabolites quantification in spent media samples

Absolute quantification of glucose, lactate, glutamine and glutamate in spent media was determined enzymatically using YSI2950 bioanalyzer (YSI Incorporated, Yellow Springs, OH, USA).

3.5.5 Seahorse oxygen consumption rate

Cellular oxygen consumption rate (OCR) was measured with a Seahorse XF extracellular flux analyzer (Seahorse Bioscience Inc) according to the manufacturer's instructions. Briefly, cells were seeded in a Seahorse XF 24-well assay plate at a cell density of 20000 cells per well in normal growth medium. After overnight

attachment, the medium was washed and replaced with prewarmed assay medium (non-buffered DMEM supplemented with 1mM sodium pyruvate, 25mM glucose and 4mM glutamine, pH 7.4) and incubated in a non-CO2 incubator at 37 °C for 60 min. Basal levels of OCR were recorded followed by a mitochondrial stress test (1µM oligomycin, 1µM FCCP, 0.5µM rotenone/ antimycin A).

3.5.6 Metabolites extraction from cell culture samples

For untargeted experiments, cells were plated in 6-well plates with normal growth medium. After 18 hours, cells were washed with PBS and incubated for 48 hours in fresh complete medium in the presence or the absence of treatments. For labelling experiments, cells were incubated for 48 hours in fresh media supplemented with 25mM [U-$^{13}C_6$]-Glucose or 4mM [U-$^{13}C_5$] glutamine or 4mM [alpha-^{15}N] glutamine (purchased by Cambridge Isotope Laboratories, Inc.) in the presence or the absence of treatments.

Metabolites extraction for GC-MS analysis was performed as described previously (Gaglio et al., 2016). Briefly, cells were quenched with 1:1 ice-cold methanol:water and collected by scraping. After sonication, one volume of chloroform was added, and cells were vortexed at 4°C for 20 min. Samples were centrifuged at 12000 g for 10 min, and the aqueous phase was collected in a new tube and evaporated under airflow at 37°C.

For metabolites extraction for LC-MS analysis, cells were quickly rinsed with NaCl 0.9% and quenched with 500 µl ice-cold 70:30

methanol-water. The plates were placed at -80°C for 10 minutes, then the cells were collected by scraping with a pipette tip. Cells were sonicated 5 sec for 5 pulses at 70% power twice. Samples were centrifuged at 12000g for 10 min and the supernatant was collected in a new tube and evaporated under air flow at 37°C. The samples were resuspended with 150 µl of H2O prior to analyses.

3.5.7 Metabolites extraction from tissue samples

Metabolites extraction for GC-MS analysis was performed as described previously (Gaglio et al., 2016). Briefly, 0.1 ml ice-cold methanol was added to 10mg of tissue. An equal volume of water was added and samples were sonicated, incubated at -80°C and sonicated again. One volume of chloroform was added and samples were vortexed at 4°C for 30 min and then centrifuged at 12000g for 10 min. The aqueous phase was recovered and evaporated under airflow at 37°C.

For metabolites extraction for LC-MS analysis, the protocol was adapted from Naz et al (Naz et al., 2013). Briefly, 100 µl ice-cold 50:50 methanol-water was added to 10mg of tissue and samples were sonicated 5 sec for 5 pulses at 70% power twice. After a 30 min incubation at -80°C, samples were sonicated as described above. A total of 100µL of homogenate was vortexed with 320µL of ice-cold methanol for 2 minutes. Then 80µL of methyl-tert-butyl ether (MTBE) was added and the samples were placed on a shaker for 1 h at room temperature. The extracted samples were then centrifuged at 12000g for 20 min. 400µL of supernatant was

recovered and evaporated under air flow at 37°C. The samples were resuspended with 150µl of H2O prior to analyses.

3.5.8 GC-MS metabolic profiling

Derivatization was performed using automated sample prep WorkBench instrument (Agilent Technologies). Dried polar metabolites were dissolved in 60µl of 2% methoxyamine hydrochloride in pyridine (Pierce) and held at 40°C for 6 h. After dissolution and reaction, 90µl of MSTFA (N-Methyl-N-(trimethylsilyl) trifluoroacetamid) was added and samples were incubated at 60°C for 1h. Derivatized samples were analyzed by GC-MS using a DB-35MS column (30 m x 0.25mm i.d. x 0.25 µm) installed in an Agilent 7890B gas chromatograph (GC) interfaced with an Agilent 7200 Accurate-Mass Quadrupole Time-of-Flight (QTOF) mass spectrometer (MS) operating under electron impact (EI) ionization at 70eV. Samples (1µl) were injected in a splitless mode at 250°C,using helium as the carrier gas at a flow rate of 1 ml/min. The GC oven temperature was held at 100°C for 2 min and increased to 325°C at 10°C/min. GC/MS data processing was performed using Agilent Muss Hunter software and statistical and pathway analyses were performed using Mass Profiler Professional (MPP) software and MetaboAnalyst 4.0 (Chong et al., 2014). Relative metabolites abundance was carried out after normalization to internal standard d27 Myristic acid and cell number.

For labelling experiments, dried polar metabolites were dissolved in 60µl of 2% methoxyamine hydrochloride in pyridine (Pierce) and held at 40°C for 6h. After dissolution and reaction, 90µl of MTBSTFA + 1% TBDMCS (Pierce) were added and samples were incubated at 60°C for 1h.

1µl of sample was injected in splitless mode at 270°C, using helium as the carrier gas at a flow rate of 1 ml/min. The GC oven temperature was held at 100°C for 3 min and increased to 300°C at 3.5°C/min. The data were pre-processed using the OpenChrom software package (Wenig and Odermatt, 2010). Raw intensity values across accurate masses were first binned into unit masses (i.e. 50, 51, 52, etc. ± 0.1 m/z) and exported as ".csv" files followed by conversion to NetCDF using the OpenChrom software's file converters. Mass isotopologue distributions (MIDs) were determined using Matlab by integrating metabolite ion fragments and correcting for natural abundance using in-house algorithms adapted from (Fernandez et al., 1996).

3.5.9 LC-MS metabolic profiling

LC separation was performed using an Agilent 1290 Infinity UHPLC system and an InfintyLab Poroshell 120 PFP column (2.1 x 100 mm, 2.7 µm; Agilent Technologies). Mobile phase A was water with 0.1% formic acid. Mobile phase B was acetonitrile with 0.1% formic acid. The injection volume was 15 µL and LC gradient conditions were: 0 min: 100% A; 2 min: 100% A; 4 min: 99% A; 10 min: 98% A;11 min: 70% A; 15 min: 70% A; 16 min:

100% A with 5 min of post-run. Flow rate was 0.2 mL/min and column temperature was 35°C. MS detection was performed using an Agilent 6550 iFunnel Q-TOF mass spectrometer with Dual JetStream source operating in negative ionization mode. MS parameters were: gas temp: 285°C; gas flow: 14 l/min; nebulizer pressure: 45psig; sheath gas temp: 330°C; sheath gas flow: 12 l/min; VCap: 3700 V; Fragmentor: 175 V; Skimmer: 65 V; Octopole RF: 750 V. Active reference mass correction was through a second nebulizer using masses with m/z: 112.9855 and 1033.9881. Data were acquired from m/z 60–1050. Data analysis and isotopic natural abundance correction was performed with MassHunter ProFinder and MassHunter VistaFlux software (Agilent).

3.5.10 ^{13}C Metabolic flux analysis

^{13}C MFA was carried out using INCA v1.7 based on Elementary Metabolite Unit (EMU) framework (Young, 2014; Young et al., 2008). Flux through metabolic network consisting of Glycolysis, PPP, TCA, FA, & Biomass synthesis was constructed (Antoniewicz, 2018) and was was estimated by lease squares regression of metabolite labelling pattern and measured extracellular fluxes. The flux values of the network were iteratively adjusted using a Levenberg-Marquardt (local search) algorithm to minimize the sum of squared residual (SSR) objective function. The best global fit was found after estimating at least 50 times using random initial guesses for all reactions in the

metabolic network. All the fluxes were subjected to chi-square statistical test to assess goodness of fit and 95% confidence intervals were computed (Antoniewicz et al., 2006).

3.5.11 Aldolase activity in cell samples

Aldolase activity was measured in cell samples in the presence or the absence of 1μM BKM120 using the Aldolase Activity Colorimetric Assay Kit (BioVision). 6x105 cells were homogenized in 100μl of assay buffer and then the samples were processed according to the protocol kit. Activity was read kinetically for 20 minutes at OD 450 nm using a Cary 60 UV-Vis spectrophotometer (Agilent Technologies).

3.5.12 ROS levels measurement

ROS levels were measured using the DCFDA Cellular Ros Detection Assay Kit (Abcam, Cambridge, UK). Cells were harvested and stained with 20μM dichloro-diyidro- fluoresceine-diacetate (DCFDA) for 30 min at 37°C. Thereafter, cells were washed and fluorescence was measured at excitation/emission wavelengths of 485nm/535nm respectively using Cary Eclipse Fluorescence Spectrophotometer (Agilent Technologies).

3.5.13 ATP quantification in cell samples

ATP levels were measured using ATP Colorimetric/Fluorometric Assay Kit (BioVision) according to the manufacturer's protocol. Fluorescence was measured at excitation/emission wavelengths of

535nm/587nm respectively using Cary Eclipse Fluorescence Spectrophotometer (Agilent Technologies).

3.5.14 Autophagy detection

Autophagic activity was detected by using the Cyto-ID™ Autophagy Detection Kit (ENZO Life Sciences). Cells were harvested by centrifugation and washed in assay buffer. Samples were resuspended in 250 µl of freshly diluted Cyto-ID reagent and incubated at 37 °C for 30 min, followed by two washes and resuspension in 500 µl of assay buffer. The Cyto-ID fluorescence was immediately measured at excitation/emission wavelengths of 480 nm/530 nm, respectively, using a Cary Eclipse Fluorescence Spectrophotometer (Agilent Technologies)

3.5.15 ALT and AST activity in liver tissues

Alanine Aminotransferase (ALT) Activity Fluorometric Assay Kit and Aspartate Aminotransferase (AST) Activity Colorimetric Assay Kit were purchased by Biovision. Briefly, 10 mg of mouse livers were homogenized in 200µl of appropriate assay buffer in TissueLyser II (Qiagen) for 30 seconds, 30 Hz power. The samples were then processed according to the manufacturer's protocols. For ALT activity, the fluorescence was read kinetically for 60 minutes at excitation/emission wavelengths of 535nm/587nm respectively using Cary Eclipse Fluorescence Spectrophotometer (Agilent Technologies). AST activity was assessed reading

kinetically for 60 minutes at OD 450 nm using a Cary 60 UV-Vis spectrophotometer (Agilent Technologies).

3.5.16 Animal model and pharmacological therapy

A549 K-RasG12S (5 x 106) or HCT116 K-RasG13D (2 x 106) cells in 200 ul of phosphate-buffered saline (PBS) and Matrigel mixed at 1:1 were injected subcutaneously (s.c) on the right flanks of 7/8-weeks old nu/nu female mice (Envigo RMS S.r.l. Italy). After cells injection, mice were monitored twice a week for body weight and tumour volume was measured using a digital caliper and calculated following the formula: tumour volume = (long side * (short side)2) / 2.

NVP-BKM120 was formulated in NMP/PEG300 (10/90, v/v). Solution was freshly daily prepared just before gavaging by dissolving the powder, first in N-Methyl-2-pyrrolidone (NMP, Sigma Aldrich) with sonication and then by adding the remaining volume of PEG300 (Sigma Aldrich) as previously described (Alagesan et al., 2015). The application volume was 10 mL/kg. CB-839 was dissolved in a vehicle containing 25% (w/v) hydroxypropyl-b-cyclodextrin (Cayman Chemical Company) in 10mmol/L citrate (pH 2.0). The formulation was 20 mg/mL for a final dosing volume of 10 mL/kg as previously described (Gross et al.). When a mean tumour volume reached 130-150 mm3, mice were divided into groups (n = 7-12) and orally administered with vehicles (CTR) or with a combination of CB-839 (200 mg/kg twice daily, 5 d per week) and NVP-BKM120 (50 mg/kg daily, 5

d per week) for two weeks. At the end of the study, animals were sacrificed and tumours collected for post mortem metabolomics analyses. For labelling experiments, 1M [U-$^{13}C_6$]-Glucose in sterile PBS was infused injecting 80 µl (20 mg) of solution at 15 min intervals 3 times before the sacrifice.For survival study, treatments were administered until either a tumour dimension reached 15 mm or both dimensions exceeded 10 mm or for evident signs of disease (i.e. motor difficulty). Mice were sacrificed with cervical dislocation under isoflurane anesthesia.

3.5.17 PET imaging and quantification

PET images were obtained using a YAP-(S)-PET II small animal scanner (ISE s.r.l., Pisa, Italy). Animals were acquired before therapy, after 7 days and after 15 days. Acquisitions and images analysis and quantification were performed as previously described (Gaglio et al., 2016).

Quantification and statistical analysis

Results are expressed as mean value ± SD. Experimental differences were tested for significance with the Student's t-test or, when possible, with the Two Way ANOVA test. A p-value of 0.05 or less was considered statistically significant. Statistics are included in the figure legends.

3.6 REFERENCES

Alagesan, B., Contino, G., Guimaraes, A.R., Corcoran, R.B., Deshpande, V., Wojtkiewicz, G.R., Hezel, A.F., Wong, K.K., Loda, M., Weissleder, R., Benes, C., Engelman, J.A., and Bardeesy, N. (2015). Combined MEK and PI3K inhibition in a mouse model of pancreatic cancer. Clin Cancer Res 21, 396-404.

Alikhani, N., Ferguson, R.D., Novosyadlyy, R., Gallagher, E.J., Scheinman, E.J., Yakar, S., and LeRoith, D. (2013). Mammary tumour growth and pulmonary metastasis are enhanced in a hyperlipidemic mouse model. Oncogene 32, 961-967.

Antoniewicz, M.R. (2018). A guide to ^{13}C metabolic flux analysis for the cancer biologist. Experimental & molecular medicine 50, 19.

Antoniewicz, M.R., Kelleher, J.K., and Stephanopoulos, G. (2006). Determination of confidence intervals of metabolic fluxes estimated from stable isotope measurements. Metabolic engineering 8, 324-337.

Chong, J., Soufan, O., Li, C., Caraus, I., Li, S., Bourque, G., Wishart, D.S., and Xia, J. (2014). MetaboAnalyst 4.0: towards more transparent and integrative metabolomics analysis. Nucleic acids research 46, W486-W494.

Damiani, C., Colombo, R., Gaglio, D., Mastroianni, F., Pescini, D., Westerhoff, H.V., Mauri, G., Vanoni, M., and Alberghina, L. (2017). A metabolic core model elucidates how enhanced utilization of glucose and glutamine, with enhanced glutamine-dependent lactate production, promotes cancer cell growth: The WarburQ effect. PLoS computational biology 13, e1005758.

Dang, L., White, D.W., Gross, S., Bennett, B.D., Bittinger, M.A., Driggers, E.M., Fantin, V.R., Jang, H.G., Jin, S., Keenan, M.C., Marks, K.M., Prins, R.M., Ward, P.S., Yen, K.E., Liau, L.M., Rabinowitz, J.D., Cantley, L.C., Thompson, C.B., Vander Heiden, M.G., and Su, S.M. (2010). Cancer-associated IDH1 mutations produce 2-hydroxyglutarate. Nature 465, 966.

Davidson, S.M., Papagiannakopoulos, T., Olenchock, B.A., Heyman, J.E., Keibler, M.A., Luengo, A., Bauer, M.R., Jha, A.K., O'Brien, J.P., Pierce, K.A., Gui, D.Y., Sullivan, L.B., Wasylenko, T.M., Subbaraj, L., Chin, C.R., Stephanopolous, G., Mott, B.T., Jacks, T., Clish, C.B., and Vander Heiden,

M.G. (2016). Environment Impacts the Metabolic Dependencies of Ras-Driven Non-Small Cell Lung Cancer. Cell metabolism 23, 517-528.

DeBerardinis, R.J., and Chandel, N.S. (2016). Fundamentals of cancer metabolism. Science advances 2, e1600200.

Elia, I., Broekaert, D., Christen, S., Boon, R., Radaelli, E., Orth, M.F., Verfaillie, C., Grunewald, T.G.P., and Fendt, S.M. (2017). Proline metabolism supports metastasis formation and could be inhibited to selectively target metastasizing cancer cells. Nature communications 8, 15267.

Fernandez, C.A., Des Rosiers, C., Previs, S.F., David, F., and Brunengraber, H. (1996). Correction of ^{13}C mass isotopomer distributions for natural stable isotope abundance. J Mass Spectrom 31, 255-262.

Gaglio, D., Metallo, C.M., Gameiro, P.A., Hiller, K., Danna, L.S., Balestrieri, C., Alberghina, L., Stephanopoulos, G., and Chiaradonna, F. (2011). Oncogenic K-Ras decouples glucose and glutamine metabolism to support cancer cell growth. Molecular systems biology 7, 523.

Gaglio, D., Valtorta, S., Ripamonti, M., Bonanomi, M., Damiani, C., Todde, S., Negri, A.S., Sanvito, F., Mastroianni, F., Di Campli, A., Turacchio, G., Di Grigoli, G., Belloli, S., Luini, A., Gilardi, M.C., Colangelo, A.M., Alberghina, L., and Moresco, R.M. (2016). Divergent in vitro/in vivo responses to drug treatments of highly aggressive NIH-Ras cancer cells: a PET imaging and metabolomics-mass-spectrometry study. Oncotarget 7, 52017-52031.

Gross, M.I., Demo, S.D., Dennison, J.B., Chen, L., Chernov-Rogan, T., Goyal, B., Janes, J.R., Laidig, G.J., Lewis, E.R., Li, J., Mackinnon, A.L., Parlati, F., Rodriguez, M.L., Shwonek, P.J., Sjogren, E.B., Stanton, T.F., Wang, T., Yang, J., Zhao, F., and Bennett, M.K. (2014). Antitumour activity of the glutaminase inhibitor CB-839 in triple-negative breast cancer. Molecular cancer therapeutics 13, 890-901.

Hay, N. (2016). Reprogramming glucose metabolism in cancer: can it be exploited for cancer therapy? Nature reviews 16, 635-649.

Hong, S., Kim, S., Kim, H.Y., Kang, M., Jang, H.H., and Lee, W.S. (2016). Targeting the PI3K signalling pathway in KRAS mutant colon cancer. Cancer medicine 5, 248-255.

Hsu, P.P., and Sabatini, D.M. (2008). Cancer cell metabolism: Warburg and beyond. Cell 134, 703-707.

Hu, H., Juvekar, A., Lyssiotis, C.A., Lien, E.C., Albeck, J.G., Oh, D., Varma, G., Hung, Y.P., Ullas, S., Lauring, J., Seth, P., Lundquist, M.R., Tolan, D.R., Grant, A.K., Needleman, D.J., Asara, J.M., Cantley, L.C., and Wulf, G.M. (2016). Phosphoinositide 3-Kinase Regulates Glycolysis through Mobilization of Aldolase from the Actin Cytoskeleton. Cell 164, 433-446.

Huang, S., Chong, N., Lewis, N.E., Jia, W., Xie, G., and Garmire, L.X. (2016). Novel personalized pathway-based metabolomics models reveal key metabolic pathways for breast cancer diagnosis. Genome medicine 8, 34.

Ilic, N., Birsoy, K., Aguirre, A.J., Kory, N., Pacold, M.E., Singh, S., Moody, S.E., DeAngelo, J.D., Spardy, N.A., Freinkman, E., Weir, B.A., Tsherniak, A., Cowley, G.S., Root, D.E., Asara, J.M., Vazquez, F., Widlund, H.R., Sabatini, D.M., and Hahn, W.C. (2017). PIK3CA mutant tumours depend on oxoglutarate dehydrogenase. Proceedings of the National Academy of Sciences of the United States of America 114, E3434-E3443.

Kang, H.B., Fan, J., Lin, R., Elf, S., Ji, Q., Zhao, L., Jin, L., Seo, J.H., Shan, C., Arbiser, J.L., Cohen, C., Brat, D., Miziorko, H.M., Kim, E., Abdel-Wahab, O., Merghoub, T., Frohling, S., Scholl, C., Tamayo, P., Barbie, D.A., Zhou, L., Pollack, B.P., Fisher, K., Kudchadkar, R.R., Lawson, D.H., Sica, G., Rossi, M., Lonial, S., Khoury, H.J., Khuri, F.R., Lee, B.H., Boggon, T.J., He, C., Kang, S., and Chen, J. (2015). Metabolic Rewiring by Oncogenic BRAF V600E Links Ketogenesis Pathway to BRAF-MEK1 Signalling. Molecular cell 59, 345-358.

Krall, A.S., Xu, S., Graeber, T.G., Braas, D., and Christofk, H.R. (2016). Asparagine promotes cancer cell proliferation through use as an amino acid exchange factor. Nature communications 7, 11457.

Kremer, J.C., Prudner, B.C., Lange, S.E.S., Bean, G.R., Schultze, M.B., Brashears, C.B., Radyk, M.D., Redlich, N., Tzeng, S.C., Kami, K., Shelton, L., Li, A., Morgan, Z., Bomalaski, J.S., Tsukamoto, T., McConathy, J., Michel, L.S., Held, J.M., and Van Tine, B.A. (2017). Arginine Deprivation Inhibits the Warburg Effect and Upregulates Glutamine Anaplerosis and Serine Biosynthesis in ASS1-Deficient Cancers. Cell reports 18, 991-1004.

Lane, A.N., Yan, J., and Fan, T.W. (2015). (13)C Tracer Studies of Metabolism in Mouse Tumour Xenografts. Bio-protocol 5.

Liberti, M.V., Dai, Z., Wardell, S.E., Baccile, J.A., Liu, X., Gao, X., Baldi, R., Mehrmohamadi, M., Johnson, M.O., Madhukar, N.S., Shestov, A.A., Chio, I.I.C., Elemento, O., Rathmell, J.C., Schroeder, F.C., McDonnell, D.P., and Locasale, J.W. (2017). A Predictive Model for Selective Targeting of the Warburg Effect through GAPDH Inhibition with a Natural Product. Cell metabolism 26, 648-659 e648.

Ma, S., Jiang, B., Deng, W., Gu, Z.K., Wu, F.Z., Li, T., Xia, Y., Yang, H., Ye, D., Xiong, Y., and Guan, K.L. (2015). D-2-hydroxyglutarate is essential for maintaining oncogenic property of mutant IDH-containing cancer cells but dispensable for cell growth. Oncotarget 6, 8606-8620.

Maira, S.M., Pecchi, S., Huang, A., Burger, M., Knapp, M., Sterker, D., Schnell, C., Guthy, D., Nagel, T., Wiesmann, M., Brachmann, S., Fritsch, C., Dorsch, M., Chene, P., Shoemaker, K., De Pover, A., Menezes, D., Martiny-Baron, G., Fabbro, D., Wilson, C.J., Schlegel, R., Hofmann, F., Garcia-Echeverria, C., Sellers, W.R., and Voliva, C.F. (2011). Identification and characterization of NVP-BKM120, an orally available pan-class I PI3-kinase inhibitor. Molecular cancer therapeutics 11, 317-328.

Metallo, C.M., Gameiro, P.A., Bell, E.L., Mattaini, K.R., Yang, J., Hiller, K., Jewell, C.M., Johnson, Z.R., Irvine, D.J., Guarente, L., Kelleher, J.K., Vander Heiden, M.G., Iliopoulos, O., and Stephanopoulos, G. (2011). Reductive glutamine metabolism by IDH1 mediates lipogenesis under hypoxia. Nature 481, 380-384.

Naz, S., Garcia, A., and Barbas, C. (2013). Multiplatform analytical methodology for metabolic fingerprinting of lung tissue. Analytical chemistry 85, 10941-10948.

Nielsen, J. (2017). Systems Biology of Metabolism: A Driver for Developing Personalized and Precision Medicine. Cell metabolism 25, 572-579.

Pavlova, N.N., Hui, S., Ghergurovich, J.M., Fan, J., Intlekofer, A.M., White, R.M., Rabinowitz, J.D., Thompson, C.B., and Zhang, J. (2018). As Extracellular

Glutamine Levels Decline, Asparagine Becomes an Essential Amino Acid. Cell metabolism 27, 428-438 e425.

Rahman, M., and Hasan, M.R. (2015). Cancer Metabolism and Drug Resistance. Metabolites 5, 571-600.

Samuels, Y., Diaz, L.A., Jr., Schmidt-Kittler, O., Cummins, J.M., Delong, L., Cheong, I., Rago, C., Huso, D.L., Lengauer, C., Kinzler, K.W., Vogelstein, B., and Velculescu, V.E. (2005). Mutant PIK3CA promotes cell growth and invasion of human cancer cells. Cancer cell 7, 561-573.

Scalise, M., Pochini, L., Galluccio, M., Console, L., and Indiveri, C. (2017). Glutamine Transport and Mitochondrial Metabolism in Cancer Cell Growth. Frontiers in oncology 7, 306.

Sonveaux, P., Vegran, F., Schroeder, T., Wergin, M.C., Verrax, J., Rabbani, Z.N., De Saedeleer, C.J., Kennedy, K.M., Diepart, C., Jordan, B.F., Kelley, M.J., Gallez, B., Wahl, M.L., Feron, O., and Dewhirst, M.W. (2008). Targeting lactate-fueled respiration selectively kills hypoxic tumour cells in mice. The Journal of clinical investigation 118, 3930-3942.

Wellen, K.E., Lu, C., Mancuso, A., Lemons, J.M., Ryczko, M., Dennis, J.W., Rabinowitz, J.D., Coller, H.A., and Thompson, C.B. (2010). The hexosamine biosynthetic pathway couples growth factor-induced glutamine uptake to glucose metabolism. Genes & development 24, 2784-2799.

Wenig, P., and Odermatt, J. (2010). OpenChrom: a cross-platform open source software for the mass spectrometric analysis of chromatographic data. BMC bioinformatics 11, 405.

Wolpaw, A.J., and Dang, C.V. (2017). Exploiting Metabolic Vulnerabilities of Cancer with Precision and Accuracy. Trends in cell biology 28, 201-212.

Young, J.D. (2014). INCA: a computational platform for isotopically non-stationary metabolic flux analysis. Bioinformatics (Oxford, England) 30, 1333-1335.

Young, J.D., Walther, J.L., Antoniewicz, M.R., Yoo, H., and Stephanopoulos, G. (2008). An elementary metabolite unit (EMU) based method of isotopically nonstationary flux analysis. Biotechnology and bioengineering 99, 686-699.

3.7 SUPPLEMENTARY INFORMATION

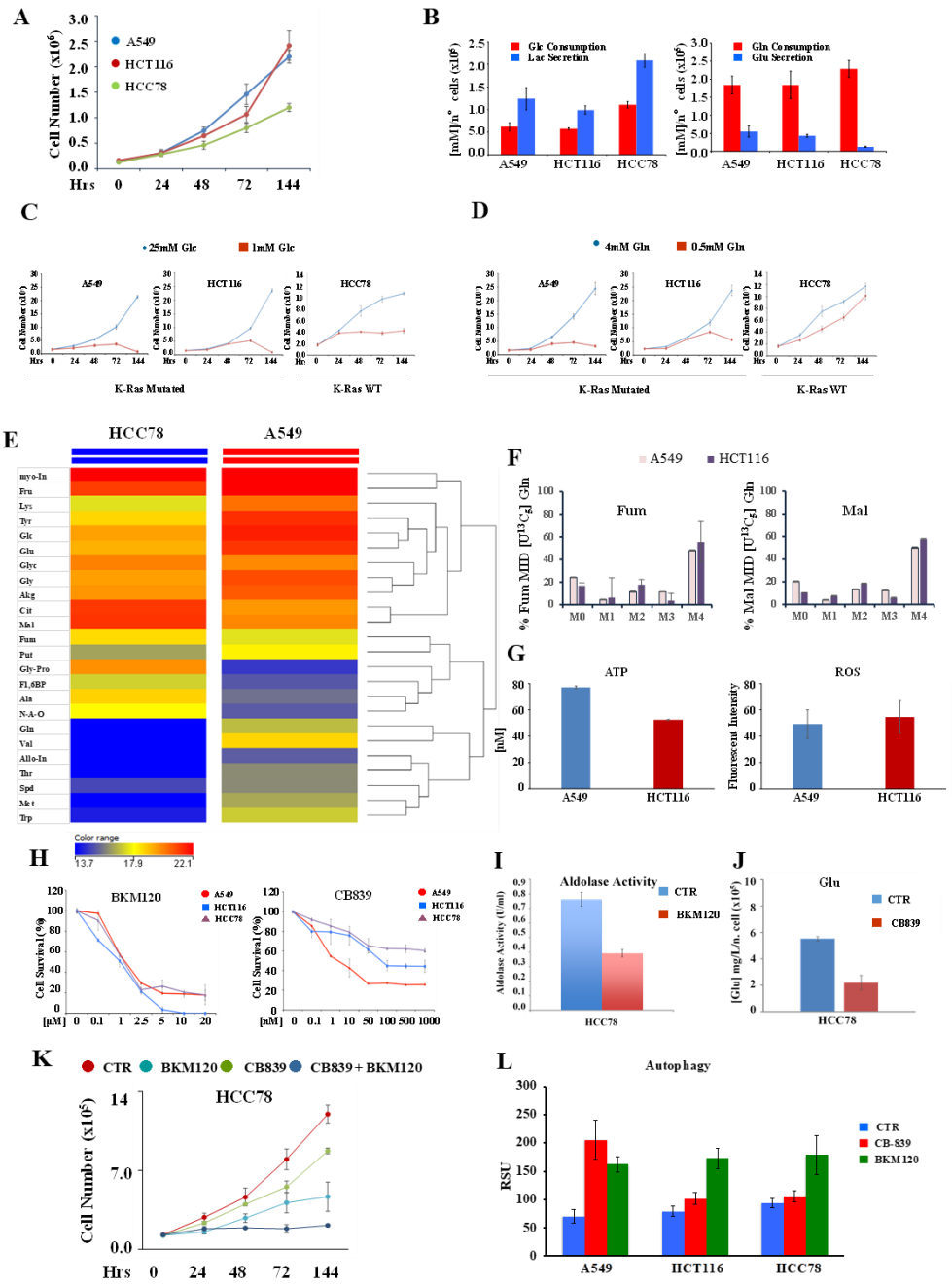

Figure S1

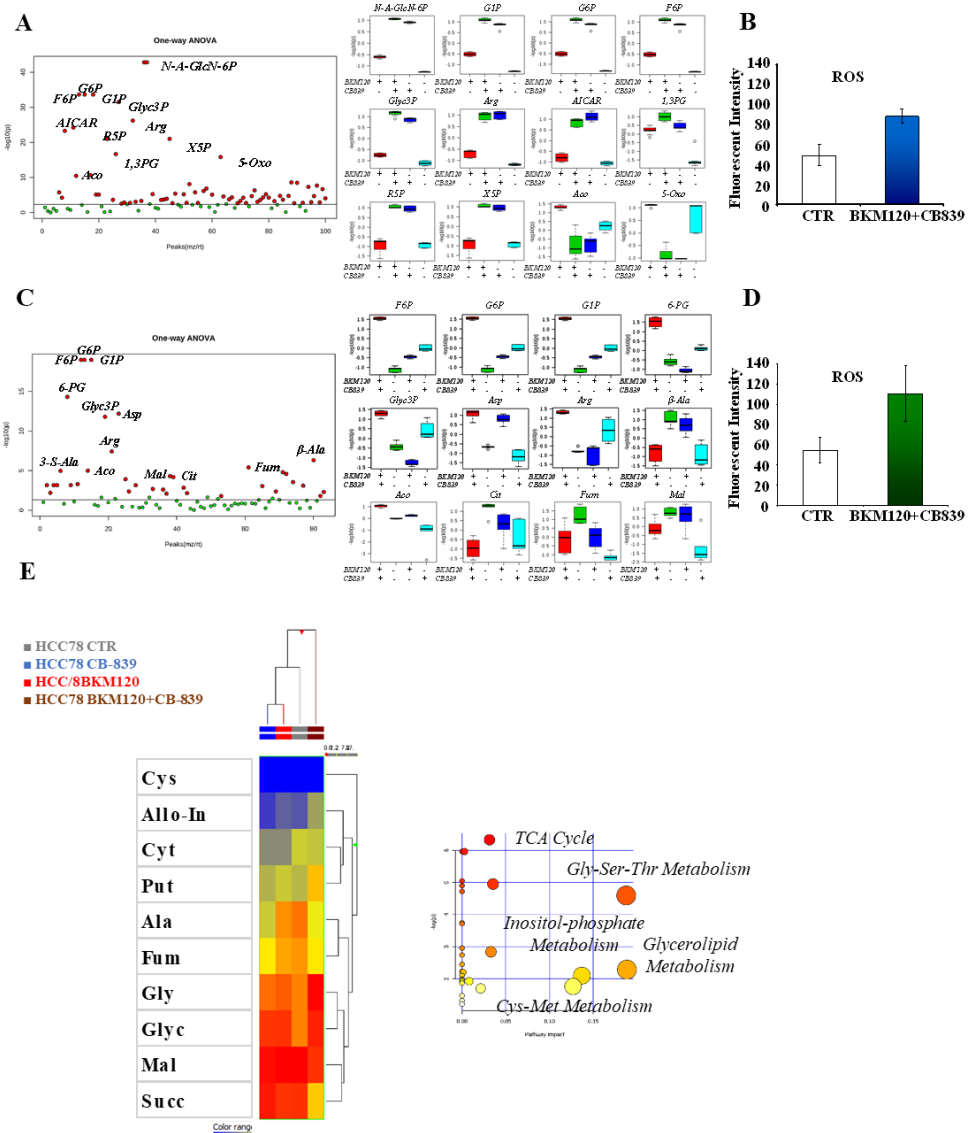
A
One-way ANOVA
N-A-GlcN-6P
G6P
F6P
G1P
Glyc3P
AICAR
Arg
R5P
X5P
1,3PG
5-Oxo
Aco
B
ROS
Fluorescent Intensity
CTR
BKM120+CB839
C
One-way ANOVA
G6P
F6P
G1P
6-PG
Glyc3P
Asp
Arg
3-S-Ala
Aco
Mal
Cit
Fum
β-Ala
D
ROS
Fluorescent Intensity
CTR
BKM120+CB839
E
HCC78 CTR
HCC78 CB-839
HCC/8BKM120
HCC78 BKM120+CB-839
Cys
Allo-In
Cyt
Put
Ala
Fum
Gly
Glyc
Mal
Succ
Color rang
12
16.5
21
TCA Cycle
Gly-Ser-Thr Metabolism
Inositol-phosphate Metabolism
Glycerolipid Metabolism
Cys-Met Metabolism

Figure S2

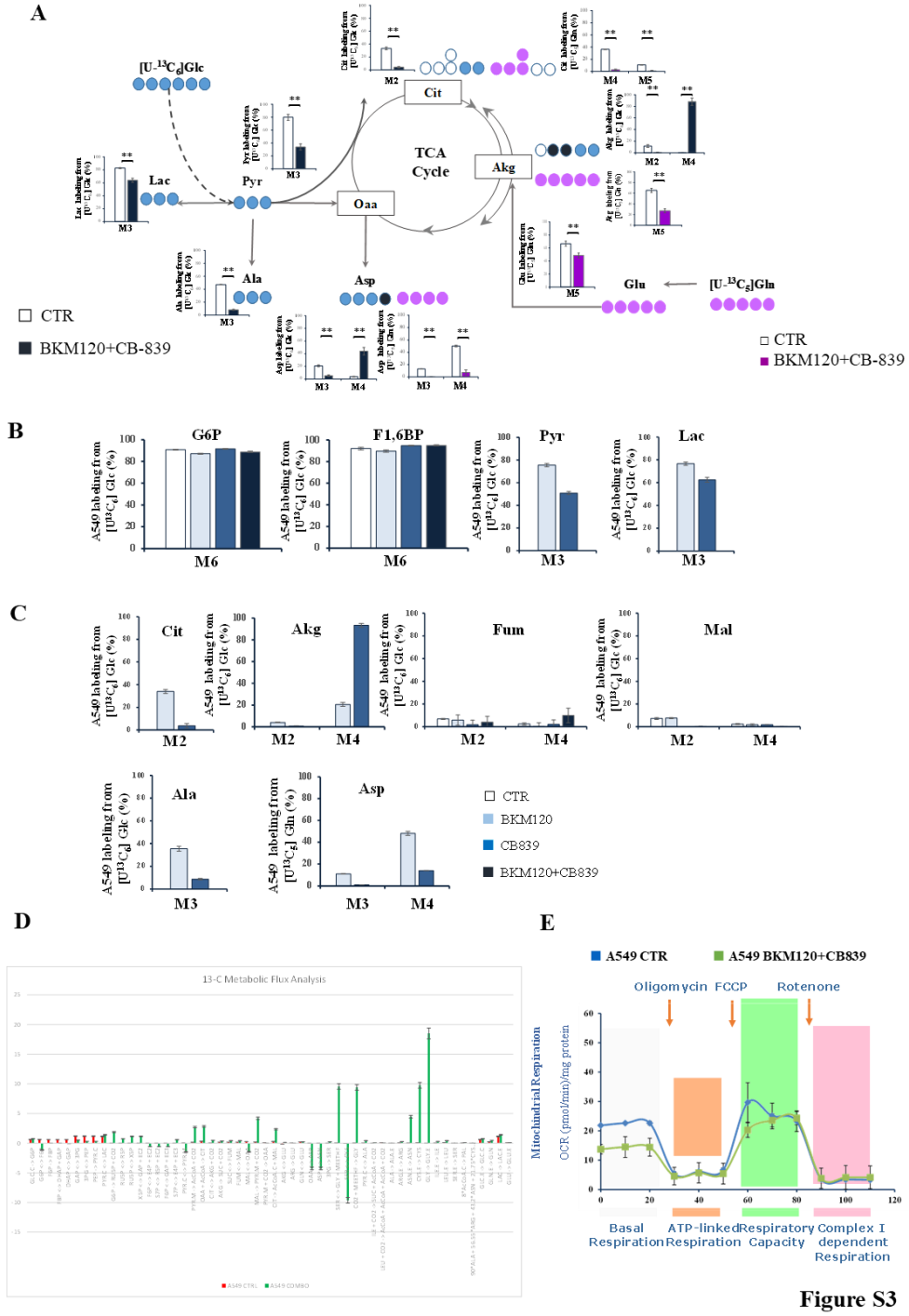
A
[U-13C6]Glc
Lac
Pyr
TCA Cycle
Cit
Akg
Oaa
Ala
Asp
Glu
[U-13C5]Gln
CTR
BKM120+CB-839
B
G6P
F1,6BP
Pyr
Lac
M6
M3
C
Cit
Akg
Fum
Mal
Ala
Asp
M2
M4
M3
CTR
BKM120
CB839
BKM120+CB839
D
13-C Metabolic Flux Analysis
E
A549 CTR
A549 BKM120+CB839
Oligomycin
FCCP
Rotenone
Mitochondrial Respiration
OCR, (pmol/min)/mg protein
Basal Respiration
ATP-linked Respiration
Respiratory Capacity
Complex I dependent Respiration

Figure S3

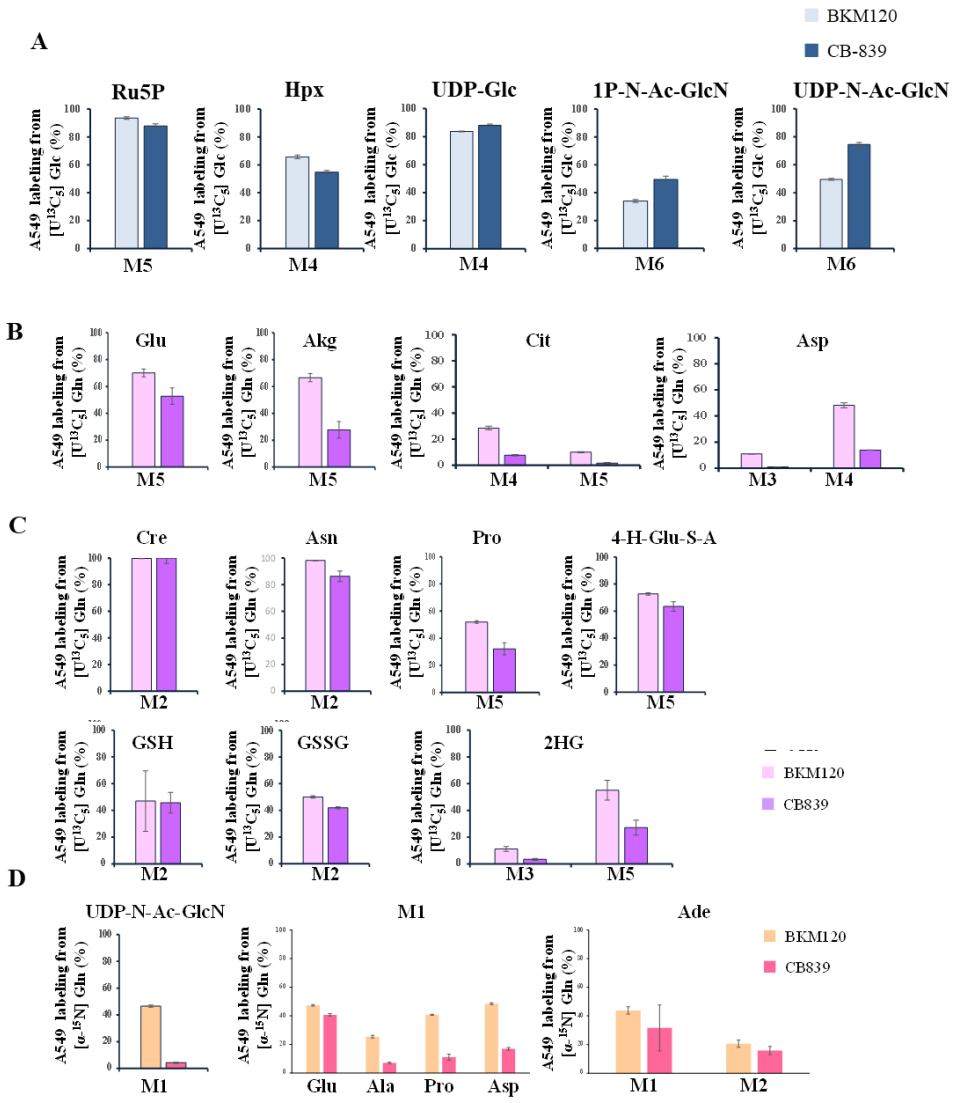
A
BKM120
CB-839
Ru5P
Hpx
UDP-Glc
1P-N-Ac-GlcN
UDP-N-Ac-GlcN
A549 labeling from [U13C5] Glc (%)
M5
M4
M4
M6
M6
B
Glu
Akg
Cit
Asp
A549 labeling from [U13C5] Gln (%)
M5
M5
M4
M5
M3
M4
C
Cre
Asn
Pro
4-H-Glu-S-A
M2
M2
M5
M5
GSH
GSSG
2HG
M2
M2
M3
M5
BKM120
CB839
D
UDP-N-Ac-GlcN
M1
Ade
A549 labeling from [α-15N] Gln (%)
M1
Glu
Ala
Pro
Asp
M1
M2
BKM120
CB839

Figure S4

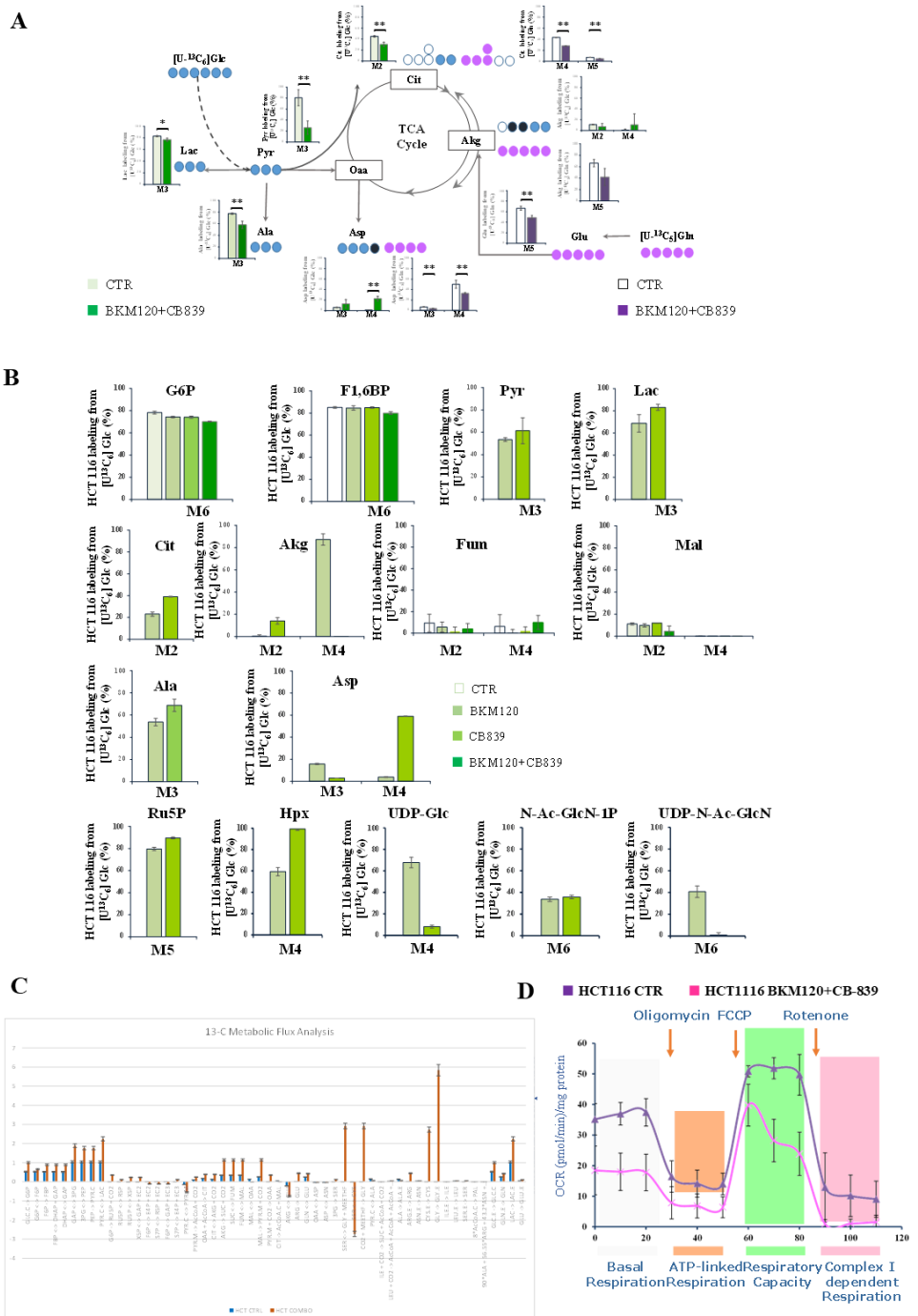
A
[U-13C6]Glc
Lac
Pyr
Ala
Cit
TCA Cycle
Akg
Oaa
Asp
Glu
[U-13C5]Gln
CTR
BKM120+CB839
B
G6P
F1,6BP
Pyr
Lac
Cit
Akg
Fum
Mal
Ala
Asp
CTR
BKM120
CB839
BKM120+CB839
Ru5P
Hpx
UDP-Glc
N-Ac-GlcN-1P
UDP-N-Ac-GlcN
C
13-C Metabolic Flux Analysis
D
HCT116 CTR
HCT1116 BKM120+CB-839
Oligomycin
FCCP
Rotenone
OCR (pmol/min)/ug protein
Basal Respiration
ATP-linked Respiration
Respiratory Capacity
Complex I dependent Respiration

Figure S5

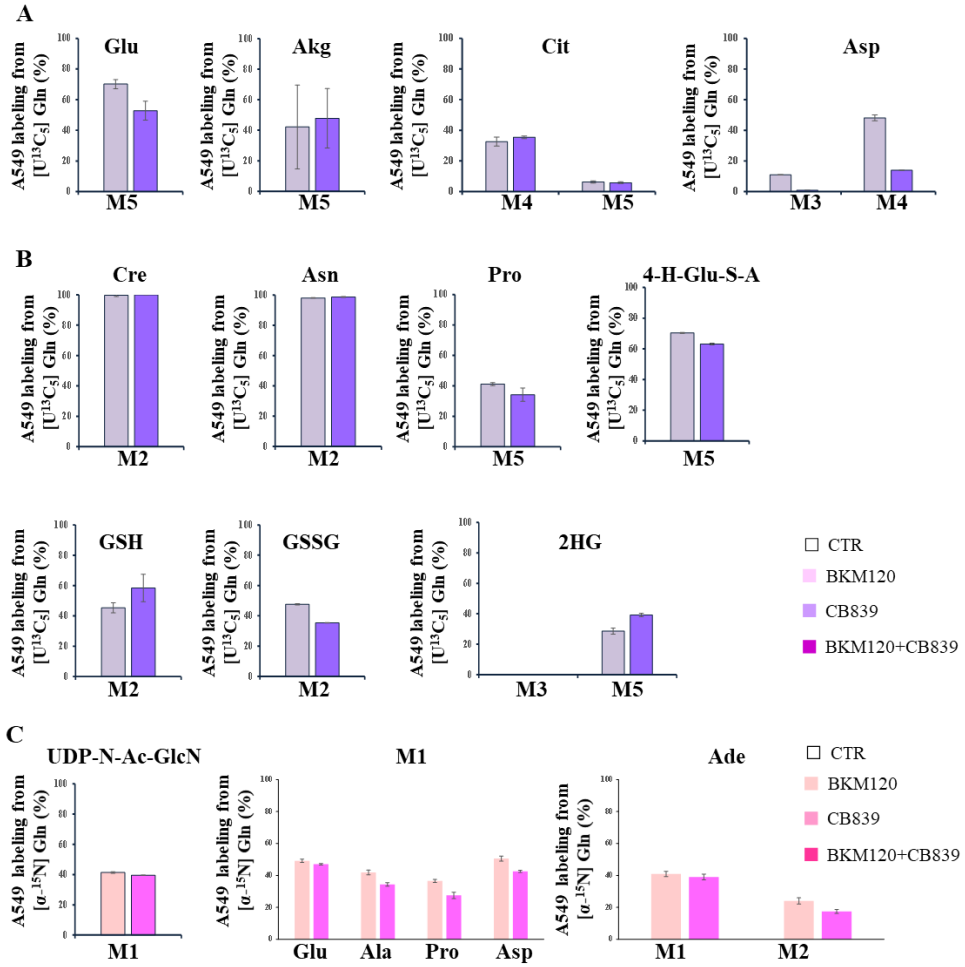
A
Glu
Akg
Cit
Asp
A549 labeling from [U13C5] Gln (%)
M5
M5
M4
M5
M3
M4
B
Cre
Asn
Pro
4-H-Glu-S-A
M2
M2
M5
M5
GSH
GSSG
2HG
M2
M2
M3
M5
CTR
BKM120
CB839
BKM120+CB839
C
UDP-N-Ac-GlcN
M1
Ade
A549 labeling from [α-15N] Gln (%)
M1
Glu
Ala
Pro
Asp
M1
M2
CTR
BKM120
CB839
BKM120+CB839

Figure S6

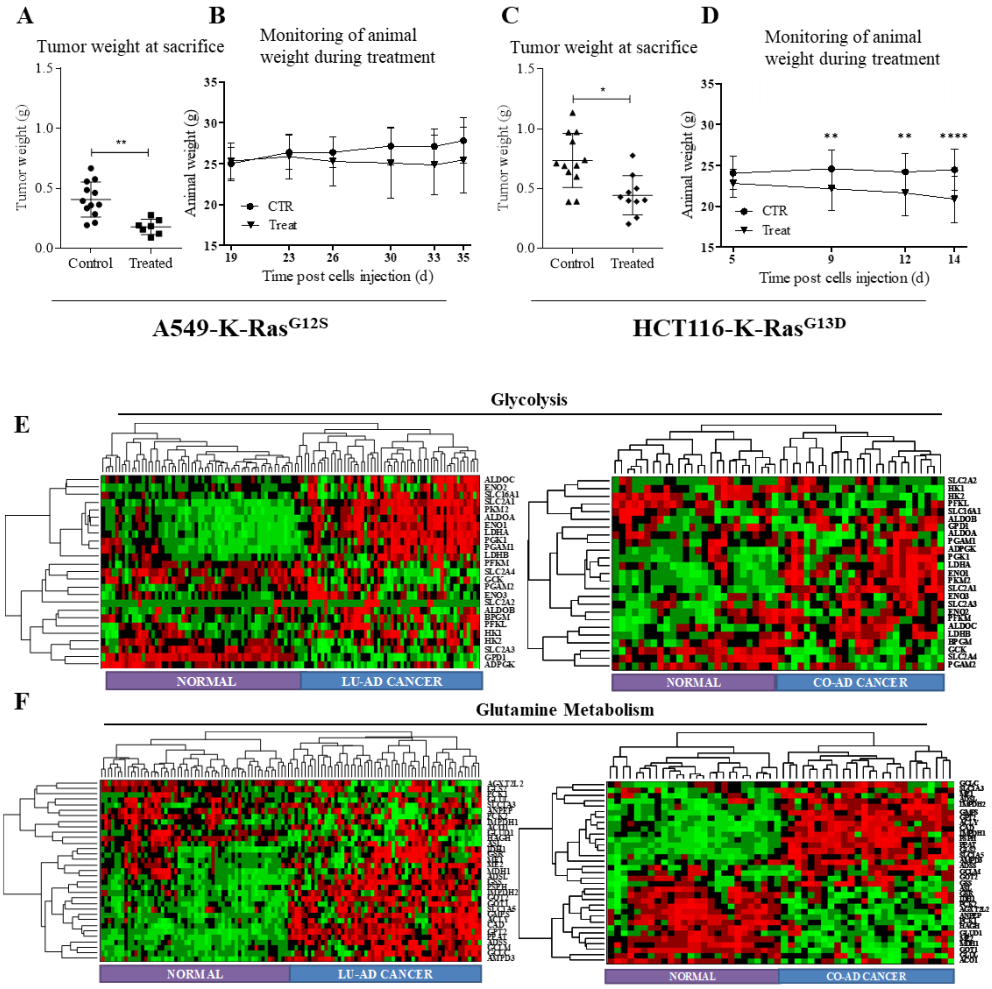
A
Tumor weight at sacrifice
Tumor weight (g)
Control
Treated
B
Monitoring of animal weight during treatment
Animal weight (g)
CTR
Treat
Time post cells injection (d)
A549-K-Ras^{G12S}
C
Tumor weight at sacrifice
D
Monitoring of animal weight during treatment
HCT116-K-Ras^{G13D}
E
Glycolysis
NORMAL
LU-AD CANCER
CO-AD CANCER
F
Glutamine Metabolism

Figure S7

Supplementary Figures Legend:

Figure 3.S1. Metabolic pathways analysis of lung and colon cancer cells.

(A) Proliferation curve of A549 (■), HCT116 (■) and HCC78 (■), human cancer cells. Cells were plated in normal medium, collected and counted at indicated time points.

(B) Extracellular uptake and secretion of Glc, Lac, Gln, and Glu in lung and colon cancer cells grown for 48h.

(C and D) Proliferation curve of A549 (left panel), HCT116 (middle panel) and HCC78 (right panel) cancer cells. Cells were plated in 6-well plates in normal medium. Culture medium was replaced after 18h with normal medium (■), containing 1mM glucose (■, C) or 0.5mM glutamine (■, D -lower panel-) . Cells were collected and counted at the indicated time points. Error bars indicates SD (n=3).

(E) Metabolic pathways analysis of A549 and HCC78 lung cancer cells. Comparison of samples by Student's t-test statistical analysis (A549 versus HCC78 lung cancer cells). Student's t-test statistical analysis was performed using Mass Profiler Professional (MPP) software. The dendrogram was produced by applying a hierarchical clustering algorithm. The color range legends was automatically generated by MPP, considering the minimum and maximum values of most compounds identified to highlight the best differences between samples through the most suitable color scale.

(F) Fumarate and Malate labelling from [U-$^{13}C_5$]glutamine in A549 (■) and HCT116 (■). Data represent mean ± SD of five independent experiments.

(G) ATP levels and intracellular ROS levels were measured by enzymatic assay and DCFDA staining respectively in A549 (■) and HCT116 (■) grown in medium for 48h. Error bars indicate SD (n=3).

(H) BKM120 dose response curves for A549, HCT116 and HCC78 measured as cells per well treated for 48 hours with 0 to 20μM BKM120 (left panel). CB-839 dose response curves for A549, HCT116 and HCC78 measured as cells per well treated for 48 hours with 0 to 1000nM CB-839 (right panel). Error bars represent standard deviation for n=3 biological replicates.

(I) Aldolase activity of HCC78 cancer cells under 1μM BKM120 for 48h measured by enzymatic assay.

(J) Glutamate production of HCC78 cancer cells under 50nM CB-839 for 48h

(K) A549 and HCT116 cancer cell lines were incubated with aldolase inhibitor (BKM120 ■), glutaminase inhibitor (CB839 ■) or BKM120 + CB-839 (■) and CTR ■ collected and counted at indicated time points.

(L) Analysis of basal autophagy of A549, HCT116 and HCC78 measured by Cyto-ID® Autophagy detection kit

Figure 3.S2. Metabolic pathways analysis of A549 and HCT116 cancer cells under drugs treatment

(A) One way ANOVA statistical analysis box plot (CTRL versus combinatorial treatment) and box plot of intracellular metabolites of A549 in the four experimental conditions by LC-MS and GC-MS.

(B) Intracellular ROS levels of A549 CTR and under combinatorial treatment measured by DCFDA staining. Error bars indicate SD (n=3).

(C) One way ANOVA statistical analysis box plot (CTR versus combinatorial treatment) and box plot of intracellular metabolites of HCT116 in the four experimental conditions by LC-MS and GC-MS.

(D) Intracellular ROS levels of HCT116 CTR and under combinatorial treatment measured by DCFDA staining. Error bars indicate SD (n=3).

(E) Untargeted metabolic profiling of HCC78 lung cancer cell lines. Hierarchical clustering heatmaps show significantly ($p \leq 0.05$) different intracellular metabolites by LC-MS and GC-MS (left panel). Enriched metabolic pathways were ranked according to their FDR values calculated by the MetPa method implemented in MetaboAnalyst 2.0 software (upper right panel). The most significant pathways were represented by both the bigger/red dots and by those dots with higher log p value. The pathway impact is calculated as the sum of the importance

measures of the matched metabolites normalized by the sum of the importance measures of all metabolites in each pathway.

Figure 3.S3. [U-$^{13}C_6$]glucose isotope labelling enrichment of A549 cancer cells under drugs treatment

(A) Schematic representation and percentage isotope labelling enrichment of metabolites from [U-$^{13}C_6$]glucose (blue circle) and [U-$^{13}C_5$]glutamine (violet circle) in A549 cancer cells.

(B-C) Intermediate metabolites labelling of glycolysis (B), TCA Cycle and amino acids (C) from [U-$^{13}C_6$]glucose of A549 in the four experimental conditions by LC-MS and GC-MS.

(D) Net flux values estimated by ^{13}C MFA for A549 cancer cells CTR and under BKM120 plus CB839 treatments. Net flux values for cells are listed using abbreviation R1, R2,...R26, respectively.

(E) Mitochondrial respiration reflected by OCR levels was detected in A549 CTR (■) and under combinatorial treatments (■) cancer cells under basal conditions or following the addition of oligomycin (0.1 μM), the uncoupler FCCP (F, 0.5 μM) or the electron transport inhibitor Rotenone (R, 2 μM).(n=5).

Figure 3.S4. [U-$^{13}C_6$]-glucose, [U-$^{13}C_5$] and [α-^{15}N]-glutamine isotope labelling enrichment of A549 cancer cells under drugs treatment

(A) Amino sugar metabolism and PPP intermediates from [U-$^{13}C_6$]glucose labelling of A549 in BKM120 and CB-839 conditions by LC-MS and GC-MS.

(B-C) Intermediates metabolites labelling of TCA cycle (B), amino acids and glutathione metabolism (C) from [U-$^{13}C_5$] glutamine of A549 in BKM120 and CB-839 conditions by LC-MS and GC-MS.

(D) Intermediates metabolites isotope labelling from [α-^{15}N]glutamine of A549 in BKM120 and CB-839 conditions by LC-MS and GC-MS.

Figure 3.S5. [U-$^{13}C_6$]glucose isotope labelling enrichment of HCT116 cancer cells under drugs treatment

(A) Schematic representation and percentage isotope labelling enrichment of metabolites from [U-$^{13}C_6$]glucose (blue circle) and [U-$^{13}C_5$]glutamine (violet circle) in HCT116cancer cells.

(B) Intermediates metabolites labelling of glycolysis, TCA Cycle, and alternative glucose metabolic pathways from [U-$^{13}C_6$]glucose of HCT116in the four experimental conditions by LC-MS and GC-MS.

(C) Net flux values estimated by ^{13}C MFA for HCT116 cancer cells CTR and under BKM120 plus CB839 treatments. (Net flux values for cells are listed using abbreviation R1, R2,...R26, respectively.

(D) Mitochondrial respiration reflected by OCR levels was detected in HCT116 CTR (■) and under combinatorial treatments (■) under basal conditions or following the addition of oligomycin

(O, 1 μM), the uncoupler FCCP (F, 0.5 μM) or the electron transport inhibitor Rotenone (R, 2 μM).(n=5).

Figure 3.S6. [U-$^{13}C_5$] and [α-^{15}N]-glutamine isotope labelling enrichment of HCT116cancer cells under drugs treatment

(A-B) Intermediates metabolites labelling of TCA cycle (A), amino acids and glutathione metabolism (B) from [U-$^{13}C_5$] glutamine of HCT116 in BKM120 and CB-839 conditions by LC-MS and GC-MS.

(C) Intermediates metabolites isotope labelling from [α-^{15}N]glutamine of HCT116 in BKM120 and CB-839 conditions by LC-MS and GC-MS.

Figure 3.S7. Post-mortem analysis of A549 and HCT116 tumours after treatment.

(A) Post mortem analysis of tumour weight of A549 tumours exposed to the combinatorial treatment compared to CTR.

(B) Weight of A549 xenograft mice exposed to the combinatorial treatment compared to CTR.

(C) Post mortem analysis of tumour weight of HCT116 tumours exposed to the combinatorial treatment compared to CTR.

(D) Weight of HCT116 xenograft mice exposed to the combinatorial treatment compared to CTR.

(E-F) TGCA expression data for lung and colon adenocarcinoma patients of glycolysis-associated gene (E) and glutamine metabolism-associated gene (F)

4. CHAPTER 2

Glutamine mediated differential metabolic reprogramming via shift of mitochondrial dynamics and lipid synthesis confers endocrine therapy resistance in ERα-positive breast cancer.

Rohit Bharat[1,2], Daniela Gaglio[1,3,], Marcella Bonanomi[1,2], Stefania Astrologo[4], Thierry Mondeel[4], Pernette J Vershure[4], Luca Magnani[5], Hans V Westerhoff [4,6,7], Lilia Alberghina[1,2], Marco Vanoni[1,2,*]

1.SYSBIO.IT, Centre of Systems Biology, Piazza della Scienza 2, Milano 20126, Italy.

2.Department of Biotechnology and Biosciences, University of Milano-Bicocca, Piazza della Scienza 2, 20126 Milan, Italy.

3.Institute of Molecular Bioimaging and Physiology, National Research Council (IBFM-CNR), via F.lli Cervi 93, 20090 Segrate, MI, Italy.

4.Synthetic, Systems Biology and Nuclear Organization, Swammerdam Institute for Life Sciences, University of Amsterdam, Amsterdam, The Netherlands

5.Department of Surgery and Cancer, Division of Cancer, Imperial College London, Imperial Centre for Translational and Experimental Medicine (ICTEM), London, W12 0NN, UK.

6.Molecular Cell Physiology, Faculty of Science, VU University Amsterdam, De Boelelaan 1085, 1081 HV Amsterdam, The Netherlands.

7.Manchester Centre for Integrative Systems Biology, School of Chemical Engineering and Analytical Science, University of Manchester

** Corresponding Authors:*

Marco Vanoni- E Mail: marco.vanoni@unimib.it

Keywords:

Metabolic Rewiring, Endocrine therapy resistance, ERα breast cancer, glycolysis, glutamine, mitochondria, metabolomics, ^{13}C metabolic flux analysis

(Manuscript in preparation)

4.1 ABSTRACT

Adaptation to endocrine therapy by estrogen receptor alpha (ERα) positive breast cancer cells via drug specific mechanisms has posed a substantial challenge in the treatment of ERα positive patients. Deeper understanding of metabolic rewiring used by cancer cells to survive and overcome the effects of drugs appears crucial for development of efficacious personalized treatment strategy. Here, using untargeted metabolomics, stable isotope resolved fluxomics and systems level modelling approach, we demonstrated the metabolic heterogeneity among endocrine therapy (ET) resistant and sensitive phenotypes to highlight drug dependent differential metabolic rewiring in ERα positive breast cancer. Divergence of metabolic propensity from glucose to glutamine was found to be a focal factor triggering enhanced mitochondrial function and fatty acid synthesis via reductive carboxylation, potentially conferring increased epigenetic regulation capability due to increased Acetyl-CoA. By using transcriptomics driven flux balance analysis (FBA) and ^{13}C metabolic flux analysis (MFA) we identified vital fluxes differentiating the resistant phenotypes along with the identification of potential targets that could aid in personalized treatment strategy. Increased OXPHOS was a strategic feature observed in aromatase inhibitor (AI) resistant cell lines where targeting with anti-diabetic drug metformin showed remarkable outcome vindicating its role as an adjuvant for therapy of AI resistant ERα positive patients.

4.2 INTRODUCTION

Over 70% of the breast cancer exhibit oncogenic activation of ERα signalling pathway (Musgrove and Sutherland, 2009) and this has served as the basis for ET which employs selective estrogen receptor modulator (SERM) like Tamoxifen, or selective estrogen down regulator. (SERD) like Fulvestrant/Faslodex and AI like Letrozole and Anastrozole, for both cancer prevention and treatment (Palmieri et al., 2014). However, over 40% of the ERα patients receiving ET eventually relapse (Clarke et al., 2015; Forbes et al., 2008; Ma et al., 2015; Markopoulos, 2010). Several molecular mechanisms for resistance development have been proposed in the past but despite significant efforts and discoveries made in recent years the exact cause of ET failure in ERα breast cancer patients remain largely unknown.

Understanding metabolic pathways required by tumour cells is now observed as a key component driving development of tumour therapeutics (Vander Heiden, 2013). Many cancer cells exhibit increased demand for nutrients like glucose to maintain their highly proliferative nature (Heiden et al., 2009). This altered metabolism could be a consequence of differential expression of oncogenes which promote the increased aerobic glycolysis, fatty acid (FA) synthesis and glutaminolysis providing them the metabolic flexibility required to support their cell growth and proliferation (Commisso et al., 2013; Gao et al., 2009; Yun et al., 2009). Resistance to ET drugs in ERα Breast cancer could also be attributed to deregulation of metabolic pathways regulated by oncogenes such as *MYC* (Miller et al., 2011), *mTOR*

(DeGraffenried et al., 2004) etc. However, even though targeting signalling pathways seems like a promising avenue for the care of breast cancer patients exhibiting endocrine resistance, it still poses a challenge, as little is known about the complex regulation and interplay between the networks.

Recent finding showed that ERα breast cancer cells exhibit differential epigenetic reprogramming in response to ET in a drug specific mechanism and show upregulation of metabolic pathway for cholesterol biosynthesis in a specific drug resistant model (Nguyen et al., 2015). However, a detailed understanding of the metabolic rewiring occurring in response to drug treatment remained unknown. In this study we vastly explored the metabolic differences among ET sensitive (MCF-7) and the derived resistant models (Tamoxifen resistant-MCF-T, Fulvestrant resistant-MCF-F, and Long Term Estrogen Deprived-LTED mimicking AI resistance) using Mass spectrometry based metabolomics, ^{13}C-Fluxomics and Computational Modelling approaches, supported by their transcriptomics knowledge, to show how differential utilization of glutamine in a specific drug resistant model redirects the metabolic switching towards a glucose independent mechanism and thus leading to enhanced mitochondrial function via OXPHOS as well as increased FA synthesis via reductive carboxylation of glutamine. Metabolic profiling of these sensitive and resistant models provides and insight to the key metabolic pathways which could be driving endocrine resistance and potentially open up new avenues for developing better targeted therapies.

Additionally we also show an already available diabetic drug-Metformin which is under clinical trial for its potential as a neoadjuvant in cancer therapy (Decensi et al., 2015),(Hadad et al., 2015) could prove to be a major asset to address the problem of ET resistance in AI resistant model.

4.3 RESULTS

4.3.1 Analogous metabolic response but divergent metabolic adaptation to ET drugs

To understand the impact of specific drug treatments on ERα breast cancer metabolism we started our analysis by looking into the immediate effect of ET drugs (Tamoxifen, Fluvestrant, and Estrogen (E2) Deprivation) on consumption and secretion of important nutrients like glucose, glutamine, lactate and glutamate and its consequential effect on cell proliferation of our cell line model MCF-7 (Figure-4.1 A-C). The metabolic phenotype of MCF-7 is highly glycolytic which is elucidated by the ΔLac/ΔGluc ratio of~ 2 (Figure-4.1C). The drug treatments showed substantial decrease in glucose consumption and lactate secretion where E2 deprivation showed the maximum decrease (Figure-4.1B), but interestingly this decrease in consumption and secretion of glucose and lactate respectively was not reflected correspondingly in cell proliferation rates when compared to tamoxifen treatment with respect to normal condition, where tamoxifen treatment had a much stronger effect on cell proliferation compared to –E2 (Figure-4.1A). A significant increase in glutamine consumption was observed in all the drug treatments (Figure-4.1B) but increase of ΔLac/ΔGluc ratio was only observed in –E2 condition (Figure-4.1C) suggesting that the lactate produced could be coming through glutamine. This observation could explain why E2 deprivation did not show much stronger immediate effect on cell proliferation as tamoxifen, as glutamine could be fuelling the cell survival in -E2 condition,

whereas the increased glutamine consumption in tamoxifen treatment could be as a stress response

(#Data for Fulvestrant treatment under analysis and to be included)

Next we compared the metabolic differences among ET sensitive (MCF-7) and the derived resistant cell lines (MCF-T, MCF-F and LTED) (Figure-4.1 D-F) where MCF-7 had the fastest proliferation whereas LTED was the slowest (Figure-4.1D). We noticed that after adaptation to ET drugs over the course of resistance development the tamoxifen resistant and fulvestrant resistant MCF-T & MCF-F respectively had regained back their glucose consumption ability and had higher glucose consumption rates compared to MCF-7 and same was reflected in their Lactate secretion but LTED did not (Figure-4.1E). ΔLac/ΔGluc of MCF-T was ~2, similar to MCF-7 suggesting a glycolytic phenotype, but MCF-F and LTED showed ratios much higher (Figure-4.1F) indicating metabolic rewiring from glucose to glutamine or other carbon sources for lactate production. Interestingly the proliferation rates of the cell lines inversely correlated with ΔLac/ΔGluc ratio where glycolytic phenotypes having the highest proliferation rates and decreased proliferation due to a switch from glucose to glutamine mediated metabolism (Liberti and Locasale, 2016). The expression of insulin dependent glucose transporter *GLUT4* was highly upregulated in MCF-T and greatly downregulated in LTED (Figure-4.1G), whereas the glutamine transporters *SNAT1* and *SNAT2* were significantly upregulated in LTED (Figure-4.1 H, I) correlating with the consumption rates.

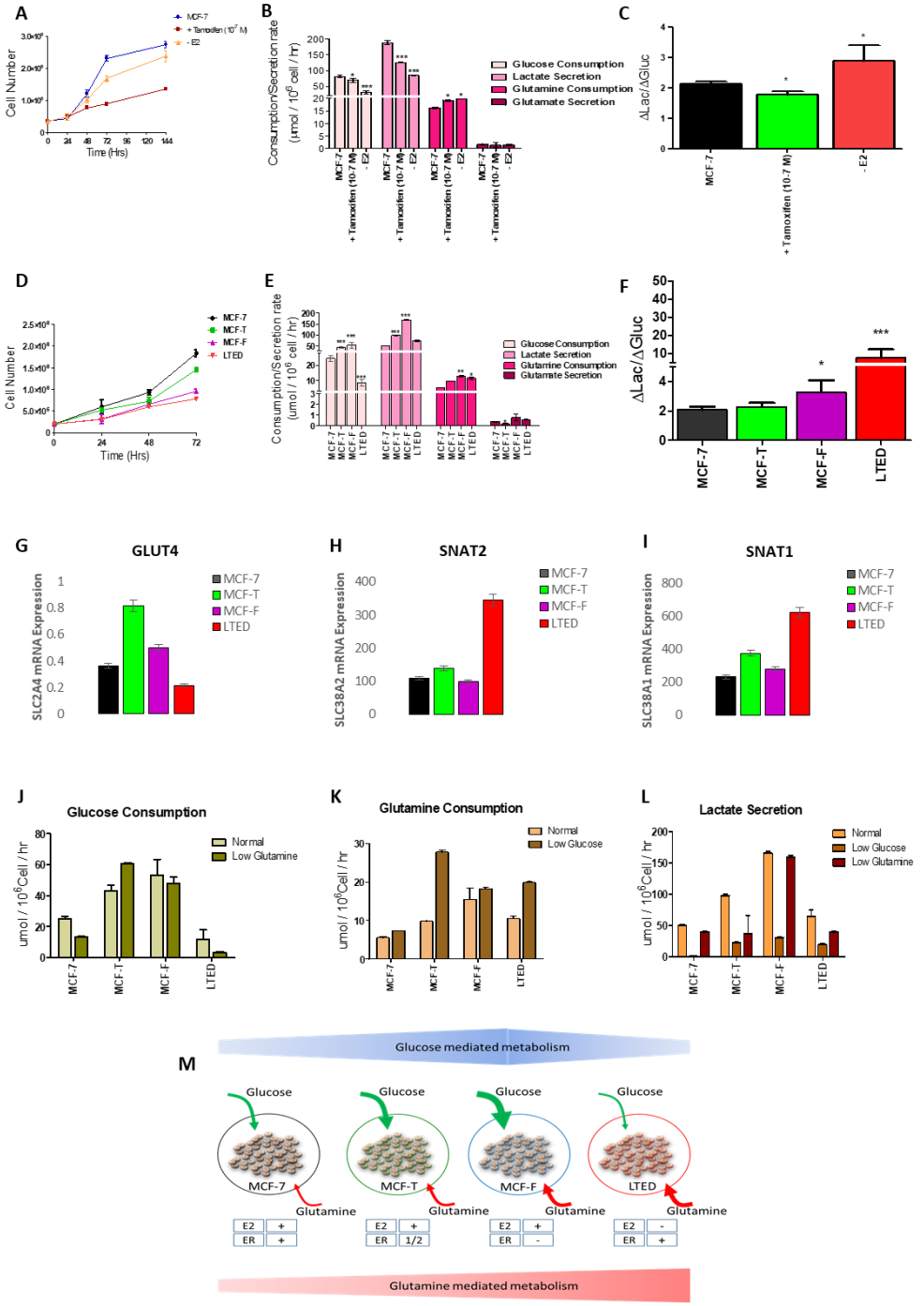
A
Cell Number
Time (Hrs)
MCF-7
+ Tamoxifen (10⁻⁷ M)
- E2
B
Consumption/Secretion rate (µmol / 10⁶ cell / hr)
Glucose Consumption
Lactate Secretion
Glutamine Consumption
Glutamate Secretion
C
ΔLac/ΔGluc
D
Cell Number
Time (Hrs)
MCF-7
MCF-T
MCF-F
LTED
E
Consumption/Secretion rate (µmol / 10⁶ cell / hr)
F
ΔLac/ΔGluc
G
GLUT4
SLC2A4 mRNA Expression
H
SNAT2
SLC38A2 mRNA Expression
I
SNAT1
SLC38A1 mRNA Expression
J
Glucose Consumption
umol / 10⁶Cell / hr
Normal
Low Glutamine
K
Glutamine Consumption
umol / 10⁶Cell / hr
Normal
Low Glucose
L
Lactate Secretion
umol / 10⁶Cell / hr
Normal
Low Glucose
Low Glutamine
M
Glucose mediated metabolism
Glucose
MCF-7
MCF-T
MCF-F
LTED
Glutamine
E2
ER
Glutamine mediated metabolism

Figure-4.1. Metabolic differences among ET sensitive and resistant cell lines. A. Effect of acute treatment with Tamoxifen/E2 Deprivation on cell proliferation of breast cancer cell line MCF-7 cell line. B. Effect of drug treatment (+Tamoxifen/-E2) on metabolite consumption/secretion rates of MCF-7 measured after 48hrs. C. Graph depicting changes in Lactate to glucose ratio upon drug treatment (+Tamoxifen/-E2) on MCF-7 measured after 48hrs. D. Differences in proliferation rates of MCF-7 compared to drug resistant cell lines MCF-T, MCF-F and LTED. E. Dissimilarities in metabolite consumption and secretion rates among ET sensitive and resistant cell lines. F. Differences in Lactate over glucose ratio among ET sensitive and resistant cell lines. G. Graph of mRNA expression of glucose transporter gene *GLUT4* (SLC2A4). H. Graph of mRNA expression of glutamine transporter gene *SNAT2* (SLC38A2). I. Graph of mRNA expression of glutamine transporter gene *SNAT1* (SLC38A1). J. Comparison of changes in glucose consumption rates among cell lines when grown in normal media or upon nutrient perturbation with low glutamine condition. K. Comparison of changes in glutamine consumption rates among cell lines when grown in normal condition of upon nutrient perturbation with low glucose condition. L. Comparative differences in lactate secretion rates when cell lines were subjected to either normal or low glucose condition or low glutamine condition. M. Schematics depicting the differences among ET sensitive and resistant cell lines based on their dependence on glucose or glutamine metabolism

Nutrient perturbation experiments further validated the above findings and revealed the metabolic flexibility of the resistant cell lines where MCF-7 did not show any significant difference in glucose consumption when grown in low glutamine condition (Figure-4.1 J) indicating their less dependence on glutamine but their lactate secretion was significantly reduced in low glucose condition but not in low glutamine (Figure-4.1 L). MCF-T cells could compensate for glucose or glutamine perturbation by increasing glutamine or glucose consumption respectively (Figure-4.1 J, K). Glucose consumption of LTED cells was decreased when subjected to low glutamine media indicating their

higher dependence on glutamine and probable reduction in metabolic activity (Figure-4.1 J), whereas their glutamine consumption was increased when subjected to growth in low glucose media.

The switch from glucose to glutamine mediated metabolism seems to be independent of Estrogen Receptor (ER) status or E2 availability for the cells (Figure-4.1 M) as MCF-F have completely downregulated ER due to action of fulvestrant and partial downregulation of activity of tamoxifen on ER in MCF-T (Dixon, 2014).

4.3.2 Glutamine drives diversification of metabolic profiles in response to drug treatment.

Metabolic profiling of ET sensitive and resistance cells using untargeted mass spectrometry reveals a wide array of differences in metabolic profiles of the sensitive and resistant cell lines. Metabolites related to glutamine metabolism such as glutamine, alpha-ketoglutaric acid, glutamic acid etc. were found to be highly upregulated in the resistant cell lines and metabolites dependent on glucose metabolism such as fructose, glycerol-1-Phosphate, DHAP etc. were found to upregulated in MCF-7 (Figure- 4.2A) consistent to the above findings from nutrient consumption experiments (metabolite abundances of few key metabolites are shown in Supplementary fig-4.S3). Even though all the endocrine therapeutic approaches work by altering estrogen receptor, but contrary to the belief that they would have a similar effect on the

cells, we show that the all the ET drugs have completely different effect on breast cancer metabolism as can be seen from the PCA analysis of the resistant and sensitive cell lines (Figure- 4.2B). LTED and MCF-F had the most diverse effect as can be seen from the separation on component 2 of the PCA plot. We see that MCF-F & MCF-T grouped much closely together when compared with LTED and MCF-7 indicative of similar activity of the drugs belonging to the same class i.e. SERM's but even though tamoxifen resistant cell line had a grouping closer to MCF-F it was in between MCF-7 and MCF-F which could explain the partial agonist activity of tamoxifen (Macnab et al., 1984) . Variable importance in projection analysis (VIP) (Figure- 4.2C) reveals cholesterol as one of the key metabolites for LTED cell lines and the metabolite abundance of cholesterol was also found to be almost 2 fold higher in LTED compared to other cell lines (Supplementary fig-4.S3) which coincided with our previous findings from the RNAseq analysis (Nguyen et al., 2015). VIP analysis showed high score for eicosapentaenoic acid (EPA) in LTED which was intriguing as it has been shown to restore tamoxifen sensitivity in breast cancer with high *Akt* activity (deGraffenried et al., 2003), upregulation of EPA along with gene regulating its biosynthesis- *ACOT2* which shows to have better relapse free survival in patients with high *ACOT2* activity (Supplementary Fig-4.S4). Gene which regulates synthesis for the precursor for EPA (*FADS1*) was also found to be upregulated in LTED (Supplementary fig-4.S1A) suggesting an alternative role of this metabolite in AI resistance which should be investigated

further. Patients with high *FADS1* showed poor RFS compared to their low expression counterparts (Supplementary Fig-4.S4)

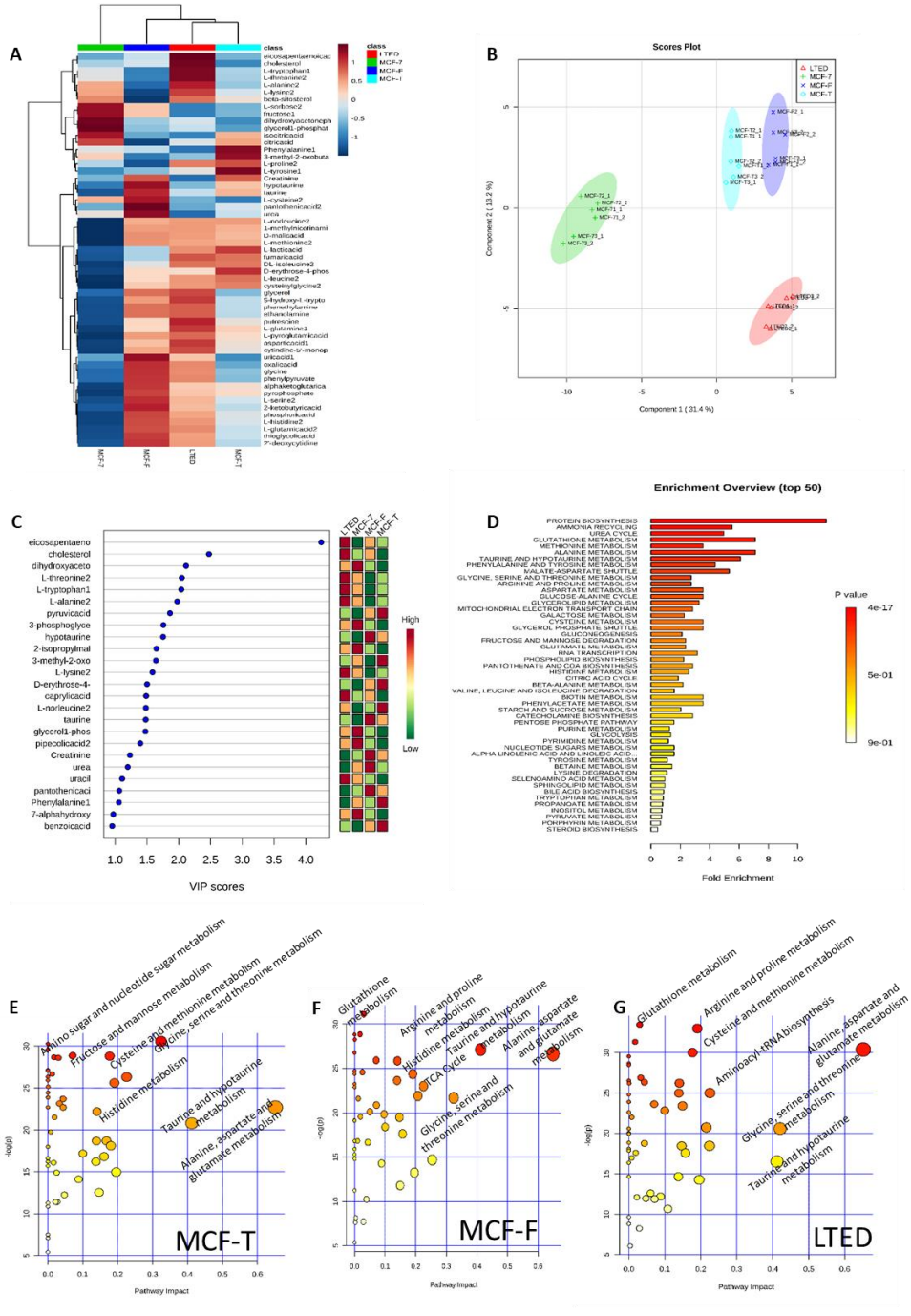
A
class
LTED
MCF-7
MCF-F
MCF-T
B
Scores Plot
LTED
MCF-7
MCF-F
MCF-T
Component 2 (13.2 %)
Component 1 (31.4 %)
C
LTED
MCF-7
MCF-F
MCF-T
eicosapentaeno
cholesterol
dihydroxyaceto
L-threonine2
L-tryptophan1
L-alanine2
pyruvicacid
3-phosphoglyce
hypotaurine
2-isopropylmal
3-methyl-2-oxo
L-lysine2
D-erythrose-4-
caprylicacid
L-norleucine2
taurine
glycerol1-phos
pipecolicacid2
Creatinine
urea
uracil
pantothenicaci
Phenylalanine1
7-alphahydroxy
benzoicacid
High
Low
1.0 1.5 2.0 2.5 3.0 3.5 4.0
VIP scores
D
Enrichment Overview (top 50)
PROTEIN BIOSYNTHESIS
AMMONIA RECYCLING
UREA CYCLE
GLUTATHIONE METABOLISM
METHIONINE METABOLISM
ALANINE METABOLISM
TAURINE AND HYPOTAURINE METABOLISM
PHENYLALANINE AND TYROSINE METABOLISM
MALATE-ASPARTATE SHUTTLE
GLYCINE, SERINE AND THREONINE METABOLISM
ARGININE AND PROLINE METABOLISM
ASPARTATE METABOLISM
GLUCOSE-ALANINE CYCLE
CYSTEINE METABOLISM
MITOCHONDRIAL ELECTRON TRANSPORT CHAIN
GALACTOSE METABOLISM
CYSTEINE METABOLISM
GLYCEROL PHOSPHATE SHUTTLE
GLUCONEOGENESIS
FRUCTOSE AND MANNOSE DEGRADATION
GLUTAMATE METABOLISM
RNA TRANSCRIPTION
PHOSPHOLIPID BIOSYNTHESIS
PANTOTHENATE AND COA BIOSYNTHESIS
HISTIDINE METABOLISM
CITRIC ACID CYCLE
BETA-ALANINE METABOLISM
VALINE, LEUCINE AND ISOLEUCINE DEGRADATION
BIOTIN METABOLISM
PHENYLACETATE METABOLISM
STARCH AND SUCROSE METABOLISM
CATECHOLAMINE BIOSYNTHESIS
PENTOSE PHOSPHATE PATHWAY
PURINE METABOLISM
GLYCOLYSIS
PYRIMIDINE METABOLISM
NUCLEOTIDE SUGARS METABOLISM
ALPHA LINOLENIC ACID AND LINOLEIC ACID
TYROSINE METABOLISM
BETAINE METABOLISM
LYSINE DEGRADATION
SELENOAMINO ACID METABOLISM
SPHINGOLIPID METABOLISM
BILE ACID BIOSYNTHESIS
TRYPTOPHAN METABOLISM
PROPANOATE METABOLISM
INOSITOL METABOLISM
PYRUVATE METABOLISM
ORNITHINE METABOLISM
STEROID BIOSYNTHESIS
P value
4e-17
5e-01
9e-01
0 2 4 6 8 10
Fold Enrichment
E
Amino sugar and nucleotide sugar metabolism
Fructose and mannose metabolism
Cysteine and methionine metabolism
Glycine, serine and threonine metabolism
Histidine metabolism
Taurine and hypotaurine metabolism
Alanine, aspartate and glutamate metabolism
MCF-T
-log(p)
Pathway Impact
F
Glutathione metabolism
Arginine and proline metabolism
Histidine metabolism
Taurine and hypotaurine metabolism
Alanine, aspartate and glutamate metabolism
TCA Cycle
Glycine, serine and threonine metabolism
MCF-F
-log(p)
Pathway Impact
G
Glutathione metabolism
Arginine and proline metabolism
Cysteine and methionine metabolism
Aminoacyl-tRNA biosynthesis
Alanine, aspartate and glutamate metabolism
Glycine, serine and threonine metabolism
Taurine and hypotaurine metabolism
LTED
-log(p)
Pathway Impact

Figure-4.2 Untargeted metabolic profiling and pathway analysis of ET resistant cell lines. A. Hierarchical clustering heat maps showing significantly ($p \leq 0.05$) different intracellular metabolites quantitated by GC-MS based untargeted metabolic analysis of MCF-7, MCF-T, MCF-F & LTED cancer cells using Metaboanlayst 4.0. B. Principal component analysis (PCA) of MCF-7, MCF-T, MCF-F and LTED with mean centring and scaling to display the inherent variance between the metabolic phenotypes. C. Variable importance in projection investigation of key metabolites among ET resistant and sensitive cell lines. D. Metabolic pathway enrichment analysis of significantly different metabolites ($p<0.05$) in resistant cell lines (MCF-T, MCF-F & LTED) when compared to MCF-7. E. Pathway impact analysis of metabolites significantly different in MCF-T vs MCF-7. F. Pathway impact analysis of metabolites significantly different in MCF-F vs MCF-7. G. Pathway impact analysis of metabolites significantly different in LTED vs MCF-7

Enrichment of metabolites belonging to protein biosynthesis, ammonia recycling, urea cycle, methionine metabolism was found in resistant cell lines compared to MCF-7. (Figure- 4.2D). Analysis of pathway impact of individual cell lines compared to MCF-7 (Figure- 4.2 E-G) shows that pathways related to glucose metabolism like amino sugar and nucleotide metabolism, fructose metabolism, glycine serine and threonine metabolism had an higher impact on MCF-T (Figure- 4.2E), whereas glutamine mediated metabolism like glutathione metabolism, aspartate and glutamate metabolism, TCA cycle etc had an higher impact on MCF-F and LTED (Figure- 4.2F and G). Higher glutathione metabolism reveals higher Reactive Oxygen Species (ROS) related stress management capabilities in MCF-F and LTED cells owing to increased glutamine reliance. Pathway perturbation analysis shows activation of nucleotide salvage pathways in LTED compared to MCF-7 (Supplementary Fig-4.S1B) which

could be a probable mechanism to sustain the nucleotide demand in case of a probably impaired pentose phosphate pathway as a consequence of decreased dependence and utilization of glucose.

4.3.3 Augmented lipogenesis propelled by reductive carboxylation drives resistance.

Next we unravelled the differences in metabolic fluxes using [U-^{13}C6] Glucose and [U-$^{13}C_5$] Glutamine stable isotope tracers (Figure- 4.3 and 4). As it was expected LTED showed decreased M3 labelling in pyruvate (PYR) from [U-$^{13}C_6$] glucose (Figure-4.3A) corresponding with overall decreased Mole Percent Enrichment (MPE) (Figure- 4.3B). Interestingly LTED and MCF-F showed higher M2 PYR labelling which indicates their higher malic enzyme activity in the direction of malate to pyruvate axis, which was verified by the higher expression of ME1 gene compared to MCF-7 (supplementary Fig-4.S1A). MCF-T showed increased M3 labelled alanine (ALA) which corresponded with the increased expression of GPT gene (supplementary Fig-4.S1A). Whereas LTED showed decreased M3 alanine but higher M2 labelled alanine, indicating that in LTED phenotype the ME1 derived pyruvate was preferentially being used more for alanine synthesis when compared to others. ME1 enzyme generates necessary NADPH required for fatty acid biosynthesis(Carracedo et al., 2013) and glutathione metabolism(Salvemini et al., 1999) and intervention of *ME1* has been shown to abrogate cancer growth(Fritz et al., 2013). This could also be one of the reason for higher glutathione metabolism observed earlier. Citrate labelling

obtained from [U-$^{13}C_6$] glucose unravelled the compromised utilization of glucose to fuel TCA cycle in resistant phenotypes as can be seen from the MPE of citrate (Figure- 4.3B).

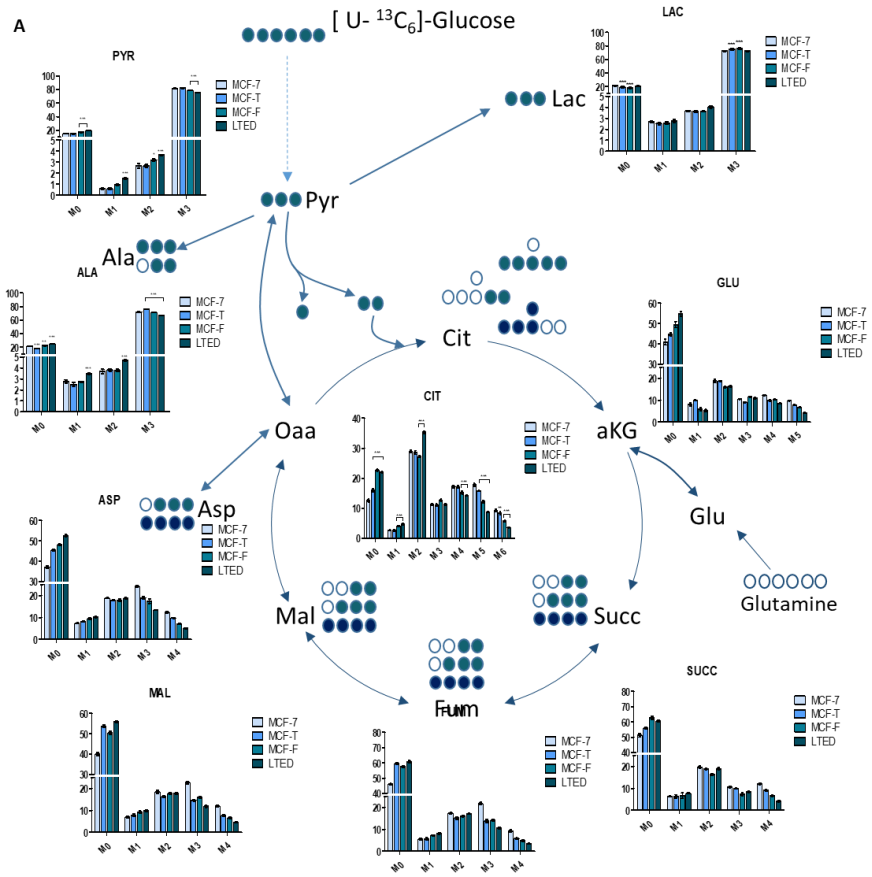

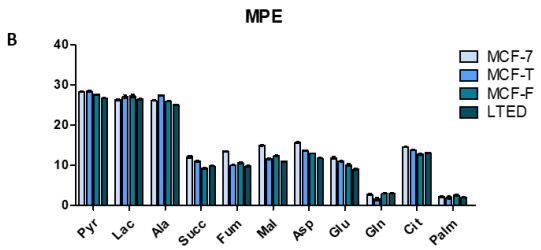

Figure-4.3 Difference in glucose metabolism among ET sensitive and resistant cell lines mapped using [U-$^{13}C_6$]-glucose. A. Schematic representation and percentage isotope labelling enrichment of metabolites from [U-$^{13}C_6$]-glucose in MCF-7, MCF-T, MCF-F & LTED cells for the metabolites of the central carbon metabolism. The coloured bubbles represent the most abundant labelling pattern for the specific metabolites whereas darker blue bubbles represent the labelling pattern upon the second round of TCA cycle. B. Mole percent enrichment showing the contribution of [U-$^{13}C_6$]-glucose in labelling of various metabolites.

But surprisingly LTED showed much higher M2 labelling in citrate, but M4 and M6 labelled citrate which indicate the subsequent 2nd and 3rd round of TCA were found to be slower than MCF-7, thus the higher M2 labelling in LTED could be due to decreased preference for glucose derived citrate and hence accumulation of citrate in mitochondria which could further be exported out into the cytoplasm to be used for lipogenesis via *SLC25A1* mitochondrial citrate carrier which was found to be much upregulated in LTED cells (Supplementary fig-4.S1A). *SLC25A1* has recently been shown to drive stemness and therapy resistance in lung cancer (Fernandez et al., 2018) and could potentially serve as a key factor and probable target in AI resistance as well. M2 and M4 labelling patterns of succinate, fumarate and malate further validate the decreased dependence on glucose to fuel TCA cycle in resistant phenotypes.

Analysis of mass isotopomer distribution obtained through [U-$^{13}C_5$] glutamine (Figure- 4.4) reveals increased reductive carboxylation of glutamine in LTED and MCF-F seen from higher M5 labelled citrate as well as M3 labelling of malate, fumarate and

aspartate when compared to MCF-7 (Figure- 4.4A). Increased MPE of TCA metabolites via glutamine was seen in resistant cells compared to sensitive counterpart indicating overall higher glutamine utilization (Figure- 4.4B). M4 labelling of succinate,

fumarate, and malate in MCF-T conveys higher rate of forward TCA cycle compared to LTED and MCF-7.

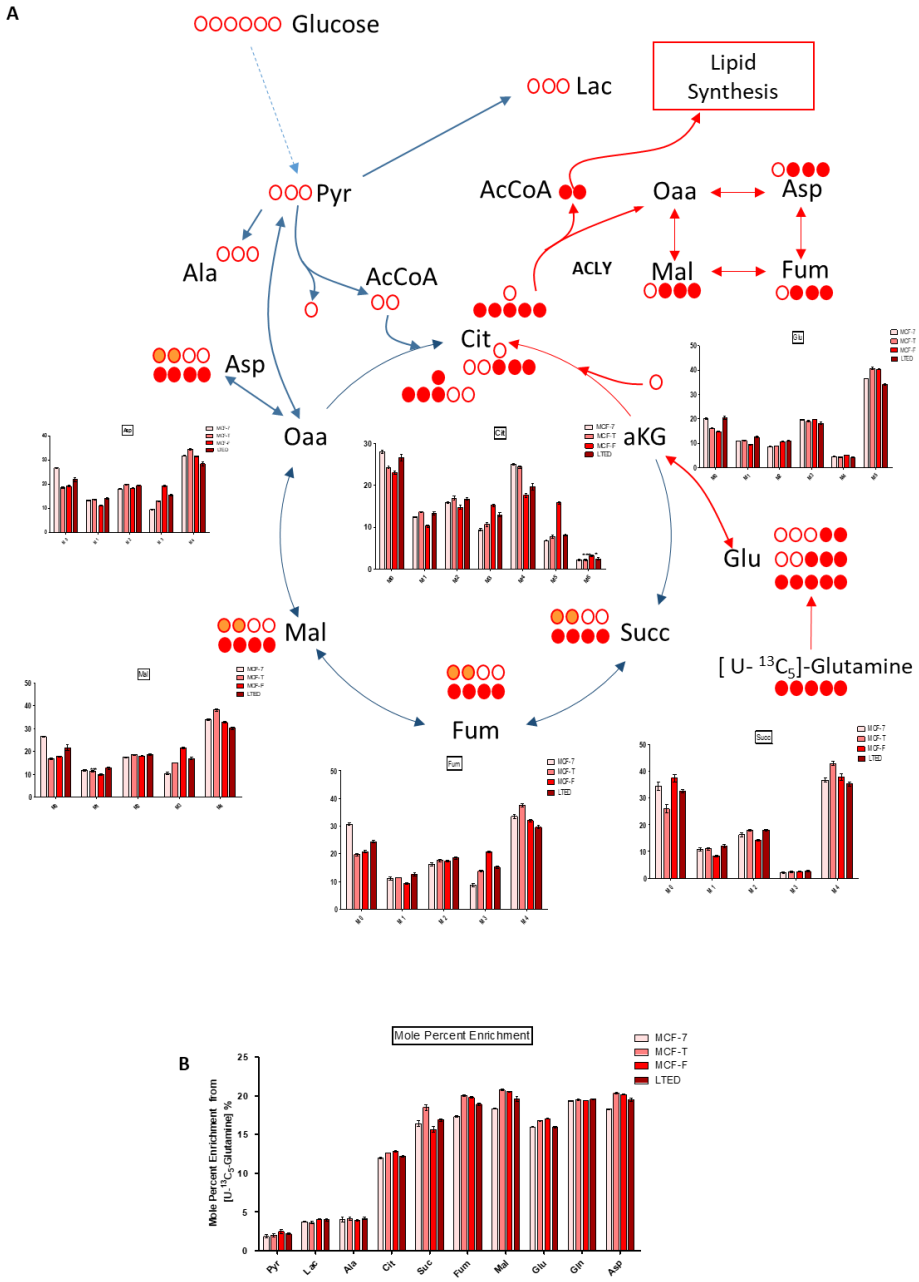

Figure-4.4 Difference in glutamine metabolism among ET sensitive and resistant cell lines mapped using stable isotope tracer [U-$^{13}C_5$]-glutamine. A. Schematic representation and percentage isotope labelling enrichment of metabolites from [U-$^{13}C_5$]-glutamine in MCF-7, MCF-T, MCF-F & LTED cells for the metabolites of the central carbon metabolism. The coloured bubbles represent the most abundant labelling pattern for the specific metabolites whereas darker red bubbles represent the labelling pattern upon the second round of TCA cycle. B. Mole percent enrichment showing the contribution of [U-$^{13}C_5$]-glutamine in labelling of various metabolites.

As stated earlier increased cholesterol biosynthesis was observed in AI resistant cell lines hence we wanted to assess the contribution of glucose and glutamine driving lipid synthesis. Analysis of overall palmitate abundance shows significantly higher palmitate levels in LTED (supplementary Fig-4.S2A). MPE analysis shows that no significant differences on Palmitate derived from [U-$^{13}C_6$] glucose but much higher MPE was observed for palmitate derived from [U-$^{13}C_5$] glutamine in LTED cell lines indicating that glutamine regulated greater acetyl co-a (AcCoA) contribution for lipid synthesis via reductive carboxylation in LTED compared to other resistant phenotypes (Supplementary Fig-4.S2C-D). Further to validate these findings AcCoA levels were measured in the cell lines grown in low glucose and low glutamine media (Supplementary Fig-4.S2B). Surprisingly AcCoA levels in LTED were much higher compared to other phenotypes and no significant effect in overall AcCoA levels was observed when grown in low glucose conditions indicating their ability to increase glutamine consumption as seen above upon nutrient perturbation. AcCoA severely dropped in

LTED when subjected to low glutamine indicating majority of the AcCoA in LTED was contributed via glutamine in contrary to glucose. MCF-F did not show much difference when compared between low glucose and low glutamine. Acety-CoA is a key molecule not only for lipid synthesis but also has great implication on epigenetic modification via histone acetylation, hence allowing modulating gene expression of vital genes. Increased reductive carboxylation and *ACLY* activity could potentially allow greater histone acetylation capability (Wellen et al., 2009) to LTED cells allowing them to differentially regulate their gene expression and potentially acquire AI resistance (Supplementary Fig-4.S2E)

4.3.4 Reprogrammed mitochondrial metabolism in AI resistance

Next we employed ^{13}C Metabolic Flux Analysis (MFA) to compute fluxes through central carbon metabolism. Metabolic model covering glycolysis, TCA metabolism, the pentose phosphate pathway (PPP), and fatty acid and biomass biosynthesis was constructed and data for uptake/secretion of major cellular fluxes like glucose, glutamine, lactate and glutamate were incorporated along with mass isotopomer distribution of metabolites. Flux estimations through the metabolic network was carried out using elementary metabolite unit (EMU)-based algorithm and its associated confidence intervals by assessing flux fit sensitivity to minor flux deviations (Figure- 4.5A) (Antoniewicz et al., 2006; Young, 2014; Young et al., 2008). The flux distributions indicated increased TCA metabolism including pyruvate dehydrogenase and glutamine anaplerosis in LTED when

compared to others (Figure- 4.5B) but had the lowest flux through glycolysis indicating its glucose independent metabolism.

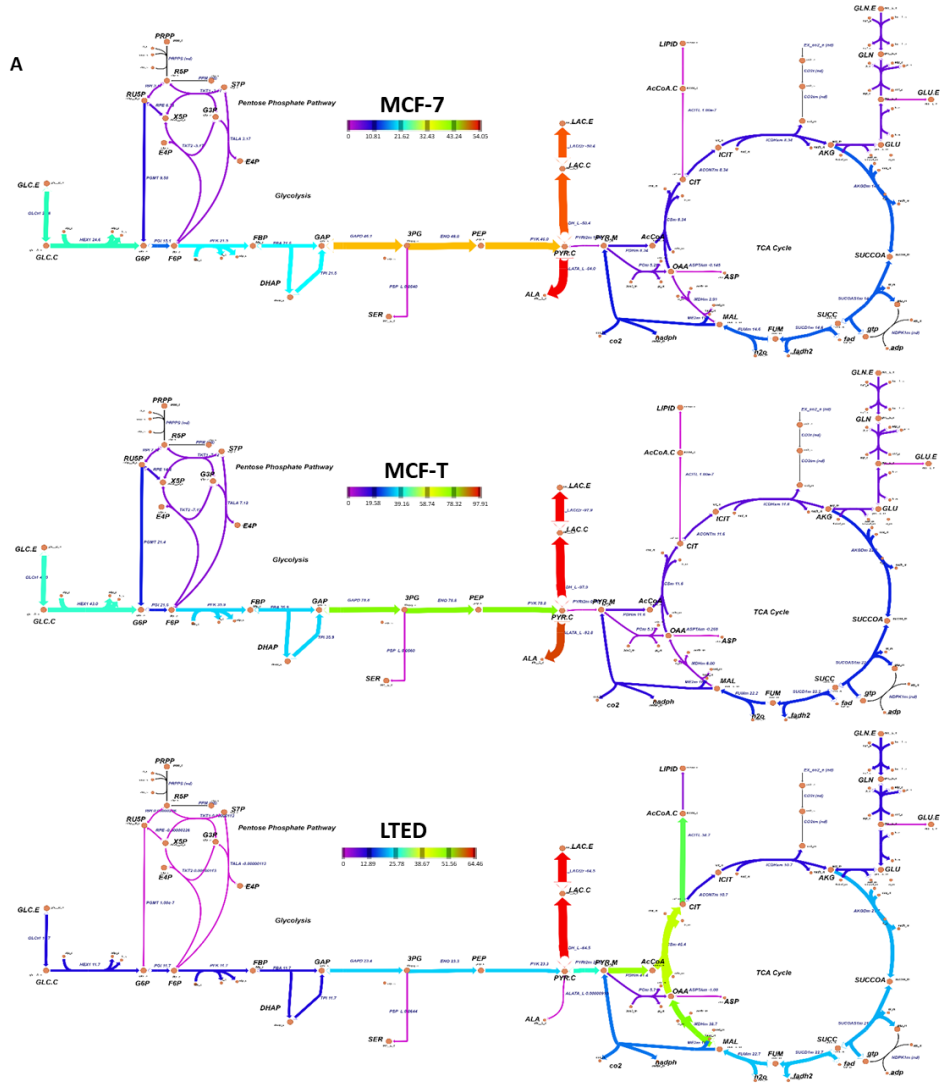
A
MCF-7
MCF-T
LTED
Pentose Phosphate Pathway
Glycolysis
TCA Cycle
PRPP
R5P
S7P
RU5P
G3P
X5P
E4P
GLC.E
GLC.C
G6P
F6P
FBP
GAP
DHAP
3PG
PEP
PYR.C
LAC.E
LAC.C
ALA
SER
LIPID
AcCoA.C
AcCoA
ICIT
CIT
AKG
OAA
ASP
GLN.E
GLN
GLU.E
GLU
SUCCOA
SUCC
MAL
FUM
co2
hdqbh
h2o
fadh2
fad
gtp
adp

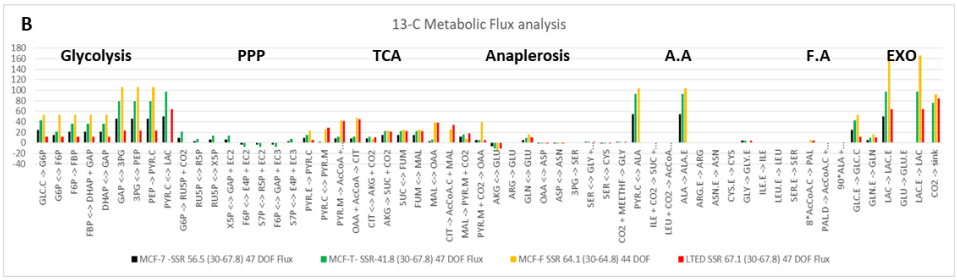
B
13-C Metabolic Flux analysis
Glycolysis
PPP
TCA
Anaplerosis
A.A
F.A
EXO
MCF-7 -SSR 56.5 (30-67.8) 47 DOF Flux
MCF-T- SSR-41.8 (30-67.8) 47 DOF Flux
MCF-F SSR 64.1 (30-64.8) 44 DOF
LTED SSR 67.1 (30-67.8) 47 DOF Flux

Figure-4.5. ^{13}C Metabolic Flux Analysis of MCF-7, MCF-T, MCF-F and LTED cell lines. A. Schematics of Central carbon metabolism depicting the differences in flux distributions obtained through ^{13}C MFA among MCF-7, MCF-T and LTED cell lines where the colours and the thickness of the arrows depict the differences in flux distribution through a reaction of the pathway. Where Violet colour represents very low flux shown with a thinner arrow and Red colour indicates higher flux through a reaction indicated with a thicker arrow. B. Bar graph of flux distribution through various reactions of the metabolic network calculated by ^{13}C metabolic flux analysis.

Corresponding to MPE, LTED showed the maximum flux towards fatty acid synthesis. Increased flux through PPP was observed in MCF-T where as MCF-F showed the highest rates of flux through glycolysis. MCF-7 and MCF-T showed higher flux in alanine secretion but was absent in MCF-F and LTED. (All the flux estimations for the cell lines are included in Supplementary Table 4.S1). Speculating based on increased flux through TCA cycle in LTED we assessed the mitochondrial activity in the cell lines by measuring oxygen consumption rate using a seahorse XF analyser (Figure- 4.6A). LTED cell line despite least glucose utilization showed the maximal basal respiration as well highest maximal respiratory capacity (Figure- 4.6C). Surprisingly MCF-F showed the least mitochondrial respiration. ATP production through respiration was the higher in LTED compared to other cell lines (Figure- 4.6B) whereas MCF-7 showed the highest non-mitochondrial respiration (Fig.-6D). Higher respiratory capacity of the LTED cell lines could is an indication towards their enhanced metabolic flexibility, possibly conferring endocrine resistance. Increased mitochondrial respiration has been observed

in drug resistance in other hormone dependent cancer like prostate cancer (Ippolito et al., 2016).

4.3.5 Metformin as a potential adjuvant in treatment of AI resistant tumours.

Having established the high mitochondrial respiration in AI-resistant cell line, we investigated the effect of anti-diabetic drug metformin (1,1-dimethylbiguanide hydrochloride) on cell proliferation and viability of the ET sensitive and resistant tumours. Metformin has been shown to has been shown to have anti-proliferative, anti-invasive, and anti-metastatic effects in multiple cancer cells (Cantrell et al., 2010; Leclerc et al., 2013) including breast cancer (Sharma and Kumar, 2018), but it is application on treatment of therapy resistant cancers has not been well exploited. Upon treatment with varying doses of metformin, remarkable results were obtained in case of LTED where metformin severely inhibited the cell proliferation at increasing doses (Figure- 4.6E). Slight dose dependent decrease in cell proliferation was also observed in MCF-T but no significant effect was seen in MCF-F upon increasing doses of metformin. Cell viability measurements showed more than 70% cell death in LTED cells whereas only about 10% cell death was observed in MCF-7 at the same concentration of metformin (20mM) (Figure-4.6F). MCF-T also showed slight decrease in cell viability on higher doses on metformin. These findings vindicate the adjuvant

use of metformin in breast cancer treatment and also promises its potential benefits in treatment of AI-Resistant cancer.

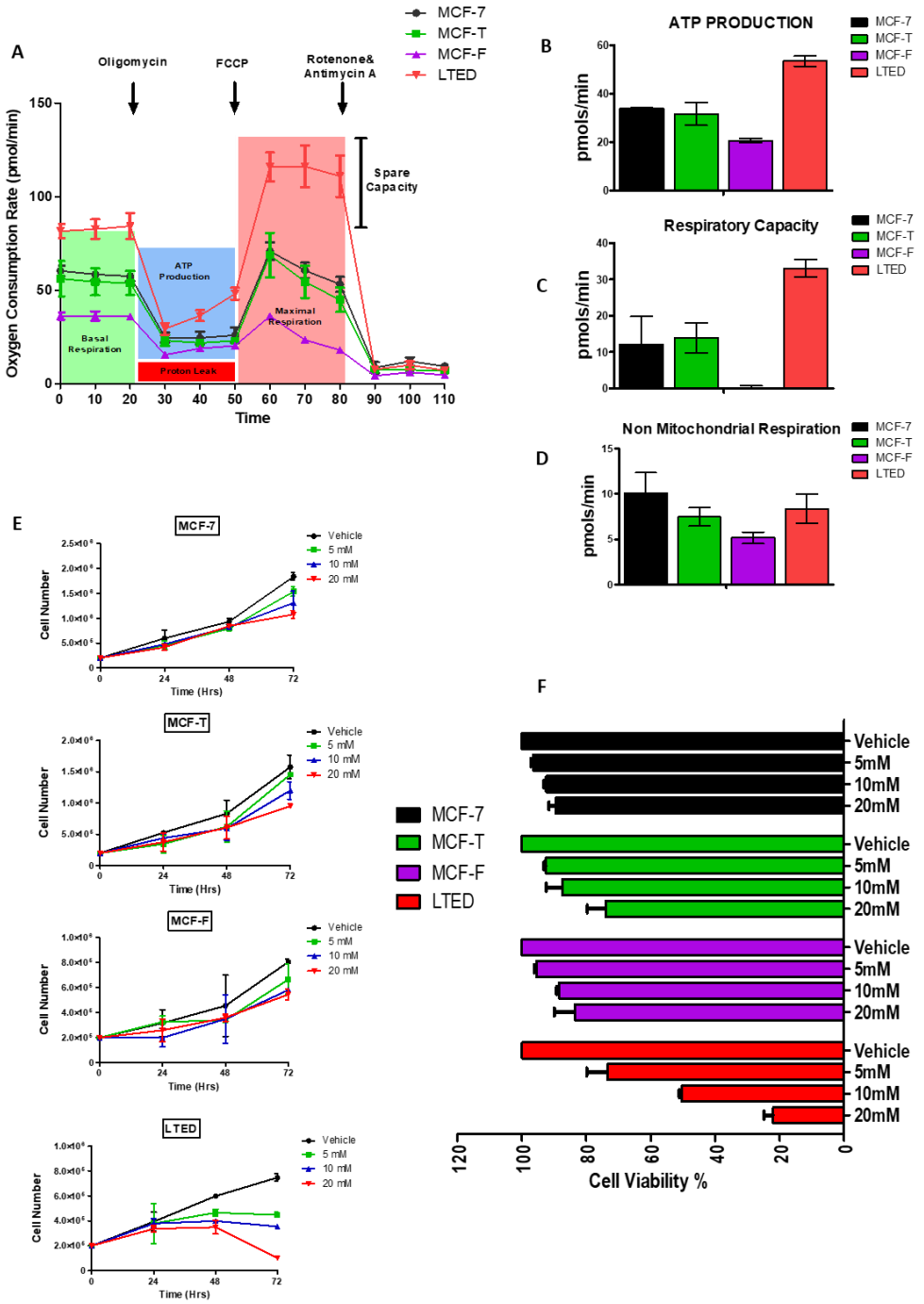
A
Oligomycin
FCCP
Rotenone&
Antimycin A
MCF-7
MCF-T
MCF-F
LTED
Oxygen Consumption Rate (pmol/min)
Time
Spare
Capacity
ATP
Production
Basal
Respiration
Proton Leak
Maximal
Respiration
B
ATP PRODUCTION
pmols/min
C
Respiratory Capacity
D
Non Mitochondrial Respiration
E
MCF-7
MCF-T
MCF-F
LTED
Vehicle
5 mM
10 mM
20 mM
Cell Number
Time (Hrs)
F
Vehicle
5mM
10mM
20mM
Cell Viability %

Figure-4.6 Differences in mitochondrial metabolism within resistant and sensitive phenotypes. A. Differences in mitochondrial respiration depicted by oxygen consumption rates (OCR) under basal condition and upon subsequent treatment with drugs altering the mitochondrial activity namely Oligomycin (1µM), Uncoupler FCCP (0.5µM) or electron transport inhibitor Rotenon&Antimycin A (2µM). B. Graph showing the ATP production via respiration obtained by subtracting the OCR after Oligomycin treatment from the basal respiration for the cell lines. C. Graph depicting the maximal respiratory capacity for the cell lines obtained by subtracting basal OCR from the OCR obtained after FCCP addition. D. Graph showing differences in the non-mitochondrial respiration for the resistant and sensitive cell lines.

4.4 DISCUSSION

Acquired drug resistance poses a major hurdle for the efficacy of endocrine therapy, and for this reason enormous efforts have been made in the last decade to identify molecular mechanism assisting resistance development.

Herein we comprehensively analyzed the metabolic differences among ET resistant cell lines (MCF-T. MCF-F, LTED) and sensitive cell line (MCF-7) and showcased the vast metabolic heterogeneity and drug dependent differential metabolic rewiring among the phenotypes. Treatment of MCF-7 with endocrine therapeutic drug induced increased glutamine consumption, whereas decreased inhibited glucose consumption and lactate secretion. Estrogen has been shown to increase insulin mediated glucose consumption and activation of *GLUT4* (Cheng et al., 2001; Yao and Brinton, 2012) and *AKT* mediated increased glycolysis in breast cancer cells (O'Mahony et al., 2012). Thus the decrease of glucose consumption and lactate secretion could be due to meddling with estrogen signalling via ET drugs. The metabolic switching and increased glutamine consumption could be an acute survival response mediated by cancer cells in order to maintain energy homeostasis. Upon prolonged treatment with ET drugs we see a regain and increase of glucose consumption in tamoxifen and fulvestrant cell lines whereas LTED cells still heavily relied upon glutamine rather than glucose. Tamoxifen and fulvestrant have been shown to interfere with mitochondrial

function (Chen et al., 2008; Cheng et al., 2001). This deregulated mitochondrial function could lead to altered AMP/ATP ratio leading to activation of *AMPK* complex (Hardie, 2011) which can increase glucose consumption and downregulate cholesterol and lipid synthesis (Jeon, 2016) in MCF-T and MCF-F and opposite for LTED. Glutamine consumption in all the resistant cell lines still remained higher than MCF-7 suggesting utilization of glutamine for much more enhanced functions rather than just maintaining energy homeostasis and potentially fueling activation of pathways required for resistance.

Detailed metabolic profiling using untargeted metabolomics approach highlighted the different metabolic pathways which were activated in resistant cell lines. An upregulation of glutamine mediated metabolites and pathways was seen in all the resistant cell lines rendering better ROS management capability via activation of pathways like glutathione metabolism (Mailloux et al., 2013). The hypothesis for *AMPK* mediated regulation of glucose and lipid metabolism were supported form metabolomics analysis where we saw decreased cholesterol in MCF-T and MCF-F whereas LTED showed higher cholesterol levels in concordance with our previous findings from transcriptomic analysis. (Nguyen et al., 2015) Increased EPA levels in LTED is an interesting finding as enzymes responsible for synthesis of EPA (*FADS1* & *ACOT2*) show to be upregulated (Supplementary figure 4.S1) and have poor survival of ER+ breast cancer patients (Supplementary Figure 4.S4). *ACOT2* is also involved in pathway of ovarian

steroidogenesis utilizing cholesterol for synthesis of estradiol. The evaluation of EPA as a biomarker as well the dissecting its role in driving resistance is an interesting avenue for further research.

Systems level analysis of flux distribution we highlighted the differences in flux distribution where reductive carboxylation of glutamine in LTED cell lines is a significant finding as glutamine is found to fuel increased lipogenesis and acetyl-CoA synthesis. Acetyl-CoA is involved in a range of metabolic functions including epigenomic regulation of DNA via histone acetylation. Increased *ACLY* expression directly links the metabolic and epigenetic axis (Wellen et al., 2009). This enhanced Acetyl-CoA level mediated by *ACLY* activity could render higher epigenetic control to LTED cells via allowing them to maintain the epigenetic landscape favoring growth and survival under lack of estrogen availability. Along with *ACLY*, finding the increased expression of mitochondrial citrate transporter *SLC25A1* further substantiates the importance of reductive carboxylation for these cells, making these two as an interesting target against resistance. Using ^{13}C MFA approach we resolved the flux distributions which is vital to determine the key fluxes required for cancer cells survival. Targeting cancer cells by inhibiting their vital fluxes can be a promising approach which can used to prevent cancer metabolic rewiring and thus making therapy more efficacious. Using ^{13}C MFA we identified increased fluxes in TCA cycle of LTED which were further validated by increased mitochondrial respiration in these cell lines further and subsequent treatment with metformin

showed remarkable results against LTED. Thus detailed analysis of metabolism stands crucial for determining therapy and guaranteeing promising outcome.

MCF-T and MCF-F showed decreased mitochondrial activity and did not respond to metformin treatment, this further could point towards leading to differential *AMPK* activity in these cell lines and needs further analysis.

This study is limited by the lack of animal experiments, but it highlights the detailed metabolic rewiring using a comprehensive systems level analysis which contributes towards the very limited knowledge available about cancer metabolic rewiring in resistance towards endocrine therapy. These findings may potentially open up new avenues of research and discovery of novel and considerably better therapeutic targets led by systems metabolomics approach for the treatment of ERα positive breast cancer patients.

,

4.5 MATERIALS & METHODS

4.4.1 Cell culture

The ET sensitive a(MCF-7) and resistant (MCF-T, MCF-F, LTED) cell lines were a generous gift from Dr. Luca Magnani (Imperial College London). MCF-7 cell line was routinely grown in Dulbecco's modified Eagle's medium (DMEM) containing 4mM L-glutamine, 1mM sodium pyruvate, plus 10-8 M 17-b-estradiol (SIGMA E8875) supplemented with 10% fetal bovine serum (FBS). MCF-T and MCF-F were cultured as MCF-7 (without estradiol) with the addition of 10-7 M 4-Hydroxytamoxifen (SIGMA H7904) and 10-7 M Fulvestrant (SIGMA I4409) respectively. LTED cell line was grown in Pheol red free-DMEM containing 4mM L-glutamine, 1mM sodium pyruvate and 10% charcoal stripped FBS. All the media were supplemented with 100 U/ml penicillin and 100 mg/ml streptomycin and the cells were incubated at 37 °C in a 5% CO2 incubator. All reagents for media were purchased from Life Technologies (Carlsbad, CA, USA).

4.4.2 Cell proliferation analysis and cell treatments

Cells were plated in 6-well plates in normal growth medium. For the proliferation curves in nutrients deprivation conditions, culture medium was replaced after 18 hours with a normal medium, a low glutamine medium (0.5mM glutamine) or a low glucose medium (1 mM glucose). The cells were collected and counted after 24, 48, 72 and 144 hours.

For the proliferation curves in the presence of the drugs, cells were treated with indicated amounts of drugs and counted at intervals of 24, 48, 72, 144 hours. For the dose-response curves, cells were treated with the indicated amounts tamoxifen, fulvestrant or deprived of Estrogen for 72 hours and then counted.

4.4.3 Cell viability analysis

Cells were plated in 6-well plates in normal growth medium and the media was replaced with media containing metformin (Indicated concentrations) after 24 hrs. Cell viability was assessed using trypan blue dye exclusion assay after 72hrs of treatment. Data are expressed as percentage of survival with respect to control condition (Normal growth medium with Vehicle)

4.4.4 Metabolites Consumption and Secretion analysis

Absolute quantification of glucose, lactate, glutamine and glutamate in spent media was determined enzymatically using YSI2950 biochemistry analyzer (YSI Incorporated, Yellow Springs, OH, USA).

4.4.5 Acetyl-Coa Quantification.

Quantification of Acetyl-Coa in cell lines was carried out using commercially available PicoProbe™Acetyl-CoA Fluorometric Assay Kit (BioVision, Milpitas, CA)

4.4.6 Metabolites extraction from cell culture samples

For untargeted experiments, cells were plated in 6-well plates with normal growth medium. After 18 hours, cells were washed with PBS and incubated for 48 hours in fresh complete medium in the presence or the absence of treatments. For labelling experiments, cells were incubated for 48 hours in fresh media supplemented with 25mM [U-$^{13}C_6$] glucose or 4mM [U-$^{13}C_5$] glutamine (purchased by Cambridge Isotope Laboratories, Inc.) in the presence or the absence of treatments.

Metabolites extraction for GC-MS analysis was performed as described previously (Gaglio et al., 2011).

For metabolites extraction for LC-MS analysis, cells were quickly rinsed with NaCl 0.9% and quenched with 500 µl ice-cold 70:30 methanol-water. The plates were placed at -80°C for 10 minutes, then the cells were collected by scraping with a pipette tip. Cells were sonicated 5 seconds for 5 pulses at 70% power twice. Samples were centrifuged at 12000g for 10 min and the supernatant was collected in a new tube and evaporated under air flow at 37°C. The samples were re-suspended with 150 ul of H2O prior to analyses.

4.4.7 GC-MS metabolic profiling

Derivatization of the samples for untargeted GC-MS analyses was performed as described (Gaglio et al., 2011). For labelling experiments, derivatization was carried out by first dissolving the polar metabolites using 60µl of 2% methoxyamine hydrochloride

in pyridine (Pierce) held at 40°C for 6h. After dissolution and reaction, 90 µl of MTBSTFA + 1% TBDMCS (Pierce) were added and samples were incubated at 60°C for 1h. Derivatized samples were analyzed by GC-MS using a DB-35MS column (30 m x 0.25mm i.d. x 0.25 µm) installed in an Agilent 7890B gas chromatograph (GC) interfaced with an Agilent 7200 Accurate-Mass Quadrupole Time-of-Flight (qTOF) mass spectrometer (MS) operating under electron impact (EI) ionization at 70eV. For untargeted experiments, GC-MS analyses was performed as previously described (Gaglio et al., 2011). Statistical and pathway analysis of the untargeted metabolomics data was performed using Metaboanalyst 4.0(Chong et al., 2018)

For labelling experiments, 1µl of sample was injected in split less mode at 270°C, using helium as the carrier gas at a flow rate of 1 ml/min. The GC oven temperature was held at 100°C for 3 min and increased to 300°C at 3.5°C/min. The data were pre-processed using the OpenChrom software package (Wenig and Odermatt, 2010). Raw intensity values across accurate masses were first binned into unit masses (i.e. 50, 51, 52, etc. ± 0.1 m/z) and exported as ".csv" files followed by conversion to NetCDF using the OpenChrom software's file converters. Mass isotopologue distributions (MIDs) were determined using MATLAB by integrating metabolite ion fragments and correcting for natural abundance from an adapted in-house algorithm (Fernandez et al., 1996)

4.4.8 Seahorse oxygen consumption rate

Cellular oxygen consumption rate (OCR) was measured with a Seahorse XF extracellular flux analyzer (Seahorse Bioscience Inc) according to the manufacturer's instructions. Briefly, cells were seeded in a Seahorse XF 24-well assay plate at a cell density of 4000 cells per well in normal growth medium. After overnight attachment, the medium was washed and replaced with pre warmed assay medium (non-buffered DMEM supplemented with 1mM sodium pyruvate, 25mM glucose and 4mM glutamine, pH 7.4) and incubated in a non-CO2 incubator at 37 °C for 60 min. Basal levels of OCR were recorded followed by a mitochondrial stress test (1μM oligomycin, 1μM FCCP, 0.5μM rotenone/ antimycin A). Three measurements of OCR were taken for the baseline and after sequential injection of mitochondrial inhibitors. Data was normalized to the protein concentration by Bradford assay ((Bio-Rad, Hemel Hempstead, UK)

4.4.9 ^{13}C Metabolic flux analysis

^{13}C MFA was carried out using INCA v1.7 based on Elementary Metabolite Unit (EMU) framework (Young, 2014; Young et al., 2008). Flux through metabolic network consisting of Glycolysis, PPP, TCA, FA, & Biomass synthesis was constructed (Antoniewicz, 2018) and was estimated by lease squares regression of metabolite labelling pattern and measured extracellular fluxes. The flux values of the network were iteratively adjusted using a Levenberg-Marquardt (local search)

algorithm to minimize the sum of squared residual (SSR) objective function (Gavin, 2013). The best global fit was found after estimating at least 50 times using random initial guesses for all reactions in the metabolic network. All the fluxes were subjected to chi-square statistical test to assess goodness of fit and 95% confidence intervals were computed (Antoniewicz et al., 2006).

4.6 REFERENCES

Antoniewicz, M.R. (2018). A guide to ^{13}C metabolic flux analysis for the cancer biologist. Exp. Mol. Med. 50, 19.

Antoniewicz, M.R., Kelleher, J.K., and Stephanopoulos, G. (2006). Determination of confidence intervals of metabolic fluxes estimated from stable isotope measurements. Metab. Eng. 8, 324–337.

Cantrell, L.A., Zhou, C., Mendivil, A., Malloy, K.M., Gehrig, P.A., and Bae-Jump, V.L. (2010). Metformin is a potent inhibitor of endometrial cancer cell proliferation—implications for a novel treatment strategy. Gynecol. Oncol. 116, 92–98.

Carracedo, A., Cantley, L.C., and Pandolfi, P.P. (2013). Cancer metabolism: fatty acid oxidation in the limelight. Nat. Rev. Cancer 13, 227–232.

Chen, J.-Q., Brown, T.R., and Yager, J.D. (2008). Mechanisms of Hormone Carcinogenesis: In Advances in Experimental Medicine and Biology, pp. 1–18.

Cheng, C.M., Cohen, M., Wang, J., and Bondy, C.A. (2001). Estrogen augments glucose transporter and IGF1 expression in primate cerebral cortex. FASEB J. 15, 907–915.

Chong, J., Soufan, O., Li, C., Caraus, I., Li, S., Bourque, G., Wishart, D.S., and Xia, J. (2018). MetaboAnalyst 4.0: towards more transparent and integrative metabolomics analysis. Nucleic Acids Res. 46, W486–W494.

Clarke, R., Tyson, J.J., and Dixon, J.M. (2015). Endocrine resistance in breast cancer – An overview and update. Mol. Cell. Endocrinol. 418, 220–234.

Commisso, C., Davidson, S.M., Soydaner-Azeloglu, R.G., Parker, S.J., Kamphorst, J.J., Hackett, S., Grabocka, E., Nofal, M., Drebin, J.A., Thompson, C.B., et al. (2013). Macropinocytosis of protein is an amino acid supply route in Ras-transformed cells. Nature 497, 633–637.

DeCensi, A., Puntoni, M., Guerrieri-Gonzaga, A., Cazzaniga, M., Serrano, D., Lazzeroni, M., Vingiani, A., Gentilini, O., Petrera, M., Viale, G., et al. (2015). Effect of Metformin on Breast Ductal Carcinoma In Situ Proliferation in a Randomized Presurgical Trial. Cancer Prev. Res. 8, 888–894.

deGraffenried, L.A. (2003). Eicosapentaenoic acid restores tamoxifen sensitivity in breast cancer cells with high Akt activity. Ann. Oncol. 14, 1051–1056.

deGraffenried, L.A. (2004). Inhibition of mTOR Activity Restores Tamoxifen Response in Breast Cancer Cells with Aberrant Akt Activity. Clin. Cancer Res. 10, 8059–8067.

Dixon, J.M. (2014). Endocrine Resistance in Breast Cancer. New J. Sci. 2014, 1–27.

Fernandez, C.A., Rosiers, C. Des, Previs, S.F., David, F., and Brunengraber, H. (1996). Correction of ^{13}C Mass Isotopomer Distributions for Natural Stable Isotope Abundance. J. Mass Spectrom. 31, 255–262.

Fernandez, H.R., Gadre, S.M., Tan, M., Graham, G.T., Mosaoa, R., Ongkeko, M.S., Kim, K.A., Riggins, R.B., Parasido, E., Petrini, I., et al. (2018). The mitochondrial citrate carrier, SLC25A1, drives stemness and therapy resistance in non-small cell lung cancer. Cell Death Differ. 25, 1239–1258.

Forbes, J.F., Cuzick, J., Buzdar, A., Howell, A., Tobias, J.S., and Baum, M. (2008). Effect of anastrozole and tamoxifen as adjuvant treatment for early-stage breast cancer: 100-month analysis of the ATAC trial. Lancet Oncol. 9, 45–53.

Fritz, V., Benfodda, Z., Henriquet, C., Hure, S., Cristol, J.-P., Michel, F., Carbonneau, M.-A., Casas, F., and Fajas, L. (2013). Metabolic intervention on lipid synthesis converging pathways abrogates prostate cancer growth. Oncogene 32, 5101–5110.

Gaglio, D., Metallo, C.M., Gameiro, P.A., Hiller, K., Danna, L.S., Balestrieri, C., Alberghina, L., Stephanopoulos, G., and Chiaradonna, F. (2014). Oncogenic K-Ras decouples glucose and glutamine metabolism to support cancer cell growth. Mol. Syst. Biol. 7, 523–523.

Gao, P., Tchernyshyov, I., Chang, T.-C., Lee, Y.-S., Kita, K., Ochi, T., Zeller, K.I., De Marzo, A.M., Van Eyk, J.E., Mendell, J.T., et al. (2009). c-Myc suppression of miR-23a/b enhances mitochondrial glutaminase expression and glutamine metabolism. Nature 458, 762–765.

Hadad, S.M., Coates, P., Jordan, L.B., Dowling, R.J.O., Chang, M.C., Done, S.J., Purdie, C.A., Goodwin, P.J., Stambolic, V., Moulder-Thompson, S., et al. (2015). Evidence for biological effects of metformin in operable breast cancer: biomarker analysis in a pre-operative window of opportunity randomized trial. Breast Cancer Res. Treat. 150, 149–155.

Hardie, D.G. (2011). AMP-activated protein kinase-an energy sensor that regulates all aspects of cell function. Genes Dev. 25, 1895–1908.

Hariharan, K., Nguyen, N.-T., Chakraborti, N., Barlat, F., and Lee, M.-G. (2015). Determination of Anisotropic Yield Coefficients by a Data-Driven Multiobjective Evolutionary and Genetic Algorithm. Mater. Manuf. Process. 30, 403–413.

Vander Heiden, M.G. (2013). Exploiting tumor metabolism: challenges for clinical translation. J. Clin. Invest. 123, 3648–3651.

Vander Heiden, M.G., Cantley, L.C., and Thompson, C.B. (2009). Understanding the Warburg Effect: The Metabolic Requirements of Cell Proliferation. Science (80-.). 324, 1029–1033.

Ippolito, L., Marini, A., Cavallini, L., Morandi, A., Pietrovito, L., Pintus, G., Giannoni, E., Schrader, T., Puhr, M., Chiarugi, P., et al. (2016). Metabolic shift toward oxidative phosphorylation in docetaxel resistant prostate cancer cells. Oncotarget 7.

Jeon, S.M. (2016). Regulation and function of AMPK in physiology and diseases. Exp. Mol. Med. 48, e245.

Leclerc, G.M., Leclerc, G.J., Kuznetsov, J.N., DeSalvo, J., and Barredo, J.C. (2013). Metformin Induces Apoptosis through AMPK-Dependent Inhibition of UPR Signaling in ALL Lymphoblasts. PLoS One 8, e74420.

Liberti, M. V., and Locasale, J.W. (2016). The Warburg Effect: How Does it Benefit Cancer Cells? Trends Biochem Sci 41, 211–218.

Ma, C.X., Reinert, T., Chmielewska, I., and Ellis, M.J. (2015). Mechanisms of aromatase inhibitor resistance. Nat. Rev. Cancer 15, 261–275.

Macnab, M.W., Tallarida, R.J., and Joseph, R. (1984). An evaluation of tamoxifen as a partial agonist by classical receptor theory — An explanation of the dual action of tamoxifen. Eur. J. Pharmacol. 103, 321–326.

Mailloux, R.J., McBride, S.L., and Harper, M.-E. (2013). Unearthing the secrets of mitochondrial ROS and glutathione in bioenergetics. Trends Biochem. Sci. 38, 592–602.

Markopoulos, C.J. (2010). Minimizing early relapse and maximizing treatment outcomes in hormone-sensitive postmenopausal breast cancer: efficacy review of AI trials. Cancer Metastasis Rev. 29, 581–594.

Miller, T.W., Balko, J.M., Ghazoui, Z., Dunbier, A., Anderson, H., Dowsett, M., Gonzalez-Angulo, A.M., Mills, G.B., Miller, W.R., Wu, H., et al. (2011). A Gene Expression Signature from Human Breast Cancer Cells with Acquired Hormone Independence Identifies MYC as a Mediator of Antiestrogen Resistance. Clin. Cancer Res. 17, 2024–2034.

Musgrove, E.A., and Sutherland, R.L. (2009). Biological determinants of endocrine resistance in breast cancer. Nat. Rev. Cancer 9, 631–643.

Nguyen, V.T.M., Barozzi, I., Faronato, M., Lombardo, Y., Steel, J.H., Patel, N., Darbre, P., Castellano, L., Győrffy, B., Woodley, L., et al. (2015). Differential epigenetic reprogramming in response to specific endocrine therapies promotes cholesterol biosynthesis and cellular invasion. Nat. Commun. 6, 10044.

O'Mahony, F., Razandi, M., Pedram, A., Harvey, B.J., and Levin, E.R. (2012). Estrogen Modulates Metabolic Pathway Adaptation to Available Glucose in Breast Cancer Cells. Mol. Endocrinol. 26, 2058–2070.

Palmieri, C., Patten, D.K., Januszewski, A., Zucchini, G., and Howell, S.J. (2014). Breast cancer: Current and future endocrine therapies. Mol. Cell. Endocrinol. 382, 695–723.

Salvemini, F., Franzé, A., Iervolino, A., Filosa, S., Salzano, S., and Ursini, M.V. (1999). Enhanced Glutathione Levels and Oxidoresistance Mediated by Increased Glucose-6-phosphate Dehydrogenase Expression. J. Biol. Chem. 274, 2750–2757.

Sharma, P., and Kumar, S. (2018). Metformin inhibits human breast cancer cell growth by promoting apoptosis via a ROS-independent pathway involving mitochondrial dysfunction: pivotal role of superoxide dismutase (SOD). Cell. Oncol. 41, 637–650.

Wellen, K.E., Hatzivassiliou, G., Sachdeva, U.M., Bui, T. V., Cross, J.R., and Thompson, C.B. (2009). ATP-Citrate Lyase Links Cellular Metabolism to Histone Acetylation. Science (80-.). 324, 1076–1080.

Wenig, P., and Odermatt, J. (2010). OpenChrom: a cross-platform open source software for the mass spectrometric analysis of chromatographic data. BMC Bioinformatics 11, 405.

Yao, J., and Brinton, R.D. (2012). Estrogen Regulation of Mitochondrial Bioenergetics. In Advances in Pharmacology, pp. 327–371.

Young, J.D. (2014). INCA: a computational platform for isotopically non-stationary metabolic flux analysis. Bioinformatics 30, 1333–1335.

Young, J.D., Walther, J.L., Antoniewicz, M.R., Yoo, H., and Stephanopoulos, G. (2008). An elementary metabolite unit (EMU) based method of isotopically nonstationary flux analysis. Biotechnol. Bioeng. 99, 686–699.

Yun, J., Rago, C., Cheong, I., Pagliarini, R., Angenendt, P., Rajagopalan, H., Schmidt, K., Willson, J.K. V., Markowitz, S., Zhou, S., et al. (2009). Glucose Deprivation Contributes to the Development of KRAS Pathway Mutations in Tumor Cells. Science (80-.). 325, 1555–1559.

4.7 SUPPLEMENTARY INFORMATION

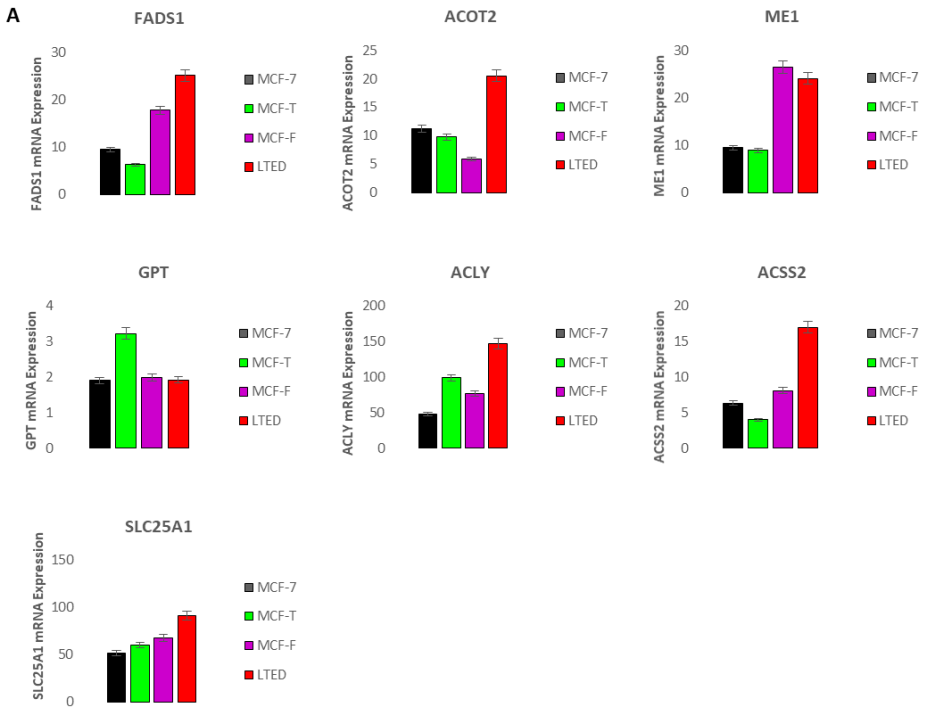

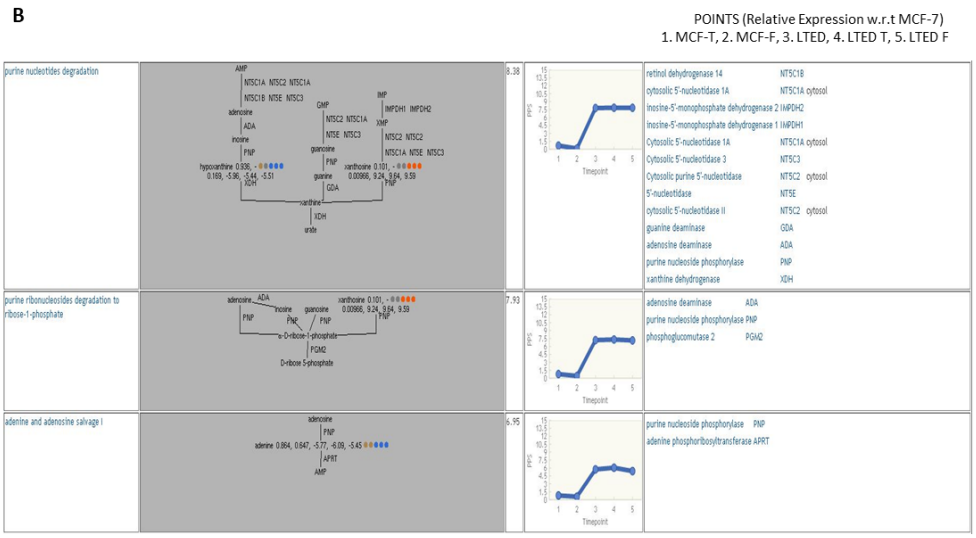

Supplementary figure: S1

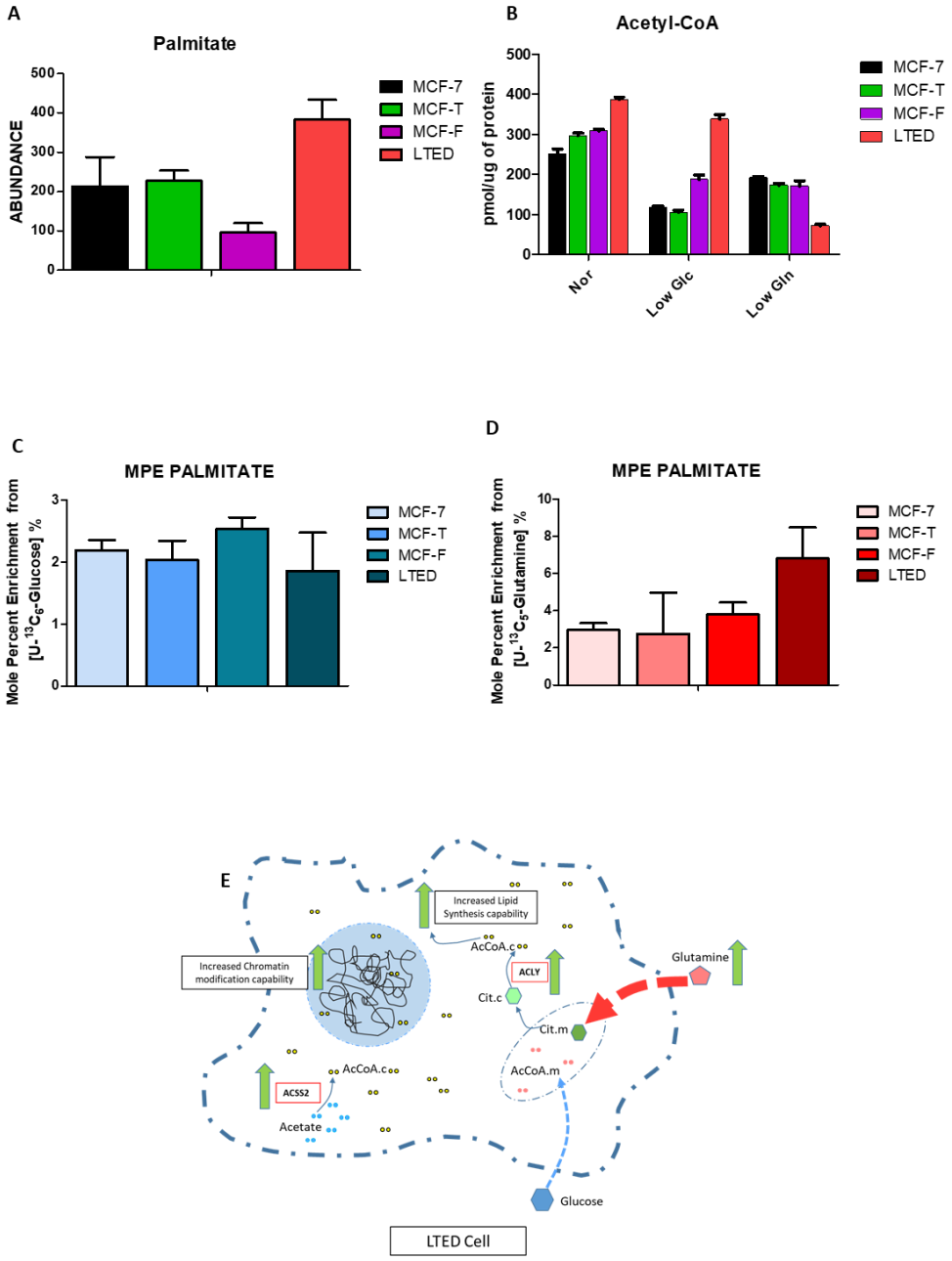

Supplementary Figure: S2

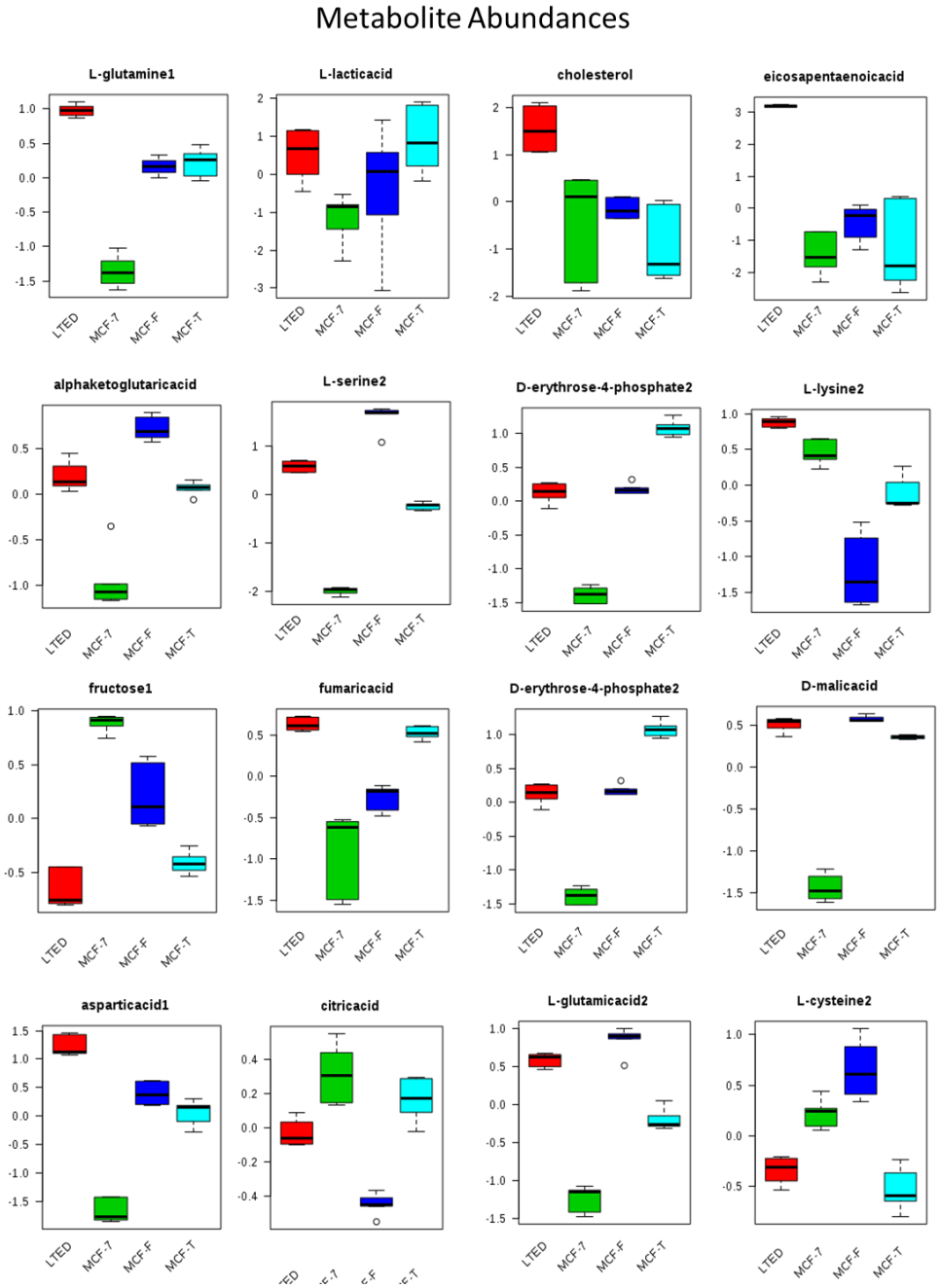

Supplementary Figure: S3

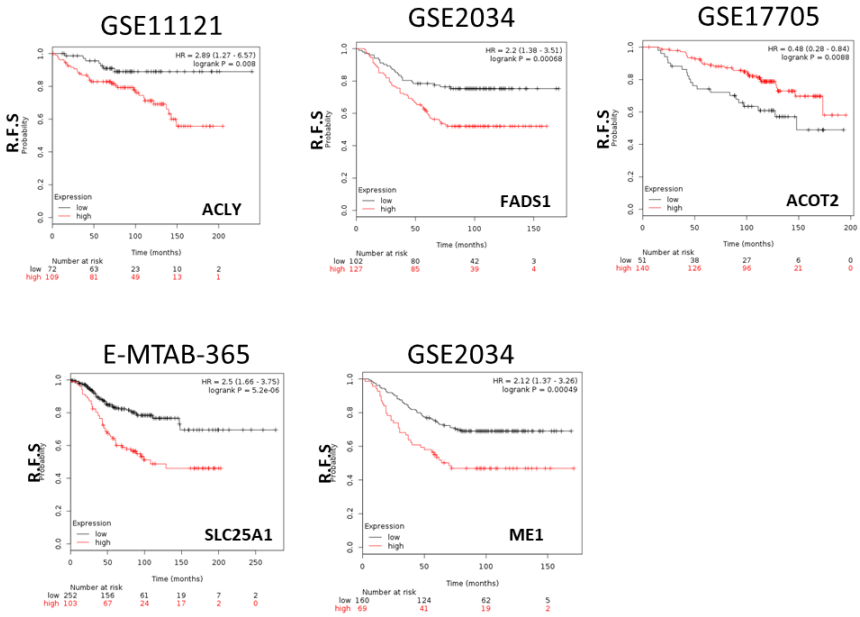

Supplementary Figure: S4

SUPPLEMENTARY FIGURE LEGENDS

Figure 4.S1: A) bar plots of expression data for *FADS1*, *ACOT2*, *ME1*, *GPT*, *ACLY*, *ACSS2* and *SLC25A1*. **B)** Pathway perturbation score analysis for MCF-T, MCF-F, LTED, LTED-T (Long term estrogen deprived-Tamoxifen resistant), LTED-F (Long term estrogen deprived-Fulvestrant resistant) with respect to MCF-7 represented by points 1, 2,3,4,5 respectively showing activation of nucleotide salvage pathway in LTED.

Figure 4.S2 A) Bar plot for metabolite abundance of palmitate in MCF-7, MCF-T, MCF-F and LTED. **B)** Intra cellular acetyl-CoA

levels in cell lines MCF-7, MCF-T, MCF-F and LTED in normal media as well in nutrient deprived media. **C)** Mole percent Enrichment of Palmitate obtained through [U-$^{13}C_6$]-Glucose in MCF-7, MCF-T, MCF-F and LTED cell lines. **D)** Mole percent Enrichment of Palmitate obtained through [U-$^{13}C_5$]-Glutamine in MCF-7, MCF-T, MCF-F and LTED cell lines. **E)** Schematics depicting model of resistance in LTED cell line.

Figure 4.S3: Intracellular metabolite levels quantified using untargeted GC-MS in MCF-7 (Red), MCF-T (Green), MCF-F (Blue) and LTED (Turquoise) cell lines

Figure 4.S4: Surival plot depicting Relapse free survival of ER+ Breast cancer patients with high expression or low expression for following genes. *ACLY*, *FADS1*, *ACOT2*, *SLC25A1* and *ME1*

5. CHAPTER 3

Dissecting glutamine roles in promoting proliferation in transformed mouse fibroblasts

Elena Sacco[1,2], Gaia De Sanctis[1,2], Marzia Di Filippo[2,3], Riccardo Colombo[2,3], Chiara Damiani[2,3], Daniela Gaglio[2,4], **Rohit Bharat**[1,2], Marcella Rocchetti[1], Eleonora Torre[1], Gianmarco Rinaldi[5,6], Sarah-Maria Fendt[5,6], Lilia Alberghina[1,2] and Marco Vanoni[1,2]*.

1. *Department of Biotechnology and Biosciences, University of Milano-Bicocca, Piazza della Scienza 2, 20126 Milan, Italy*
2. *SYSBIO, Centre of Systems Biology, Milan, Italy*
3. *Department of Informatics, Systems and Communications, University of Milano-Bicocca, Viale Sarca 336, 20126 Milan, Italy*
4. *Institute of Molecular Bioimaging and Physiology, National Research Council (IBFM-CNR), Segrate, Italy*
5. *Laboratory of Cellular Metabolism and Metabolic Regulation, Department of Oncology, University of Leuven, Leuven, B-3000, Belgium*
6. *Laboratory of Cellular Metabolism and Metabolic Regulation, Vesalius Research Center, VIB, Leuven, B-3000, Belgium*

*Corresponding author

E-mail: marco.vanoni@unimib.it

(Manuscript in preparation)

5.1 ABSTRACT

The enhanced growth and survival of K-Ras-transformed cells rely on deep changes in metabolism, including glutamine addiction and increased oxidative stress.

We study glutamine roles in metabolism, signal transduction and redox homeostasis in K-ras-transformed NIH3T3 mouse fibroblasts (NIH-RAS), by complementing glutamine deprivation with dimethyl-α-ketoglutarate (AKG) and nonessential amino acids (NEAA).

The combination AKG+NEAA only partly rescues glutamine deprivation, likely due to a low glutamine synthetase (GS) activity in NIH-RAS cells. This substitution results in low levels of nucleotides and the non-use of reductive carboxylation of AKG – predicted by ENGRO model– to synthesize lipids, whose content is lower due to downregulated expression of genes involved in lipogenesis that correlates with lower NADPH levels.

Thus, in NIH-RAS cells glutamine is essential as a carbon and nitrogen source for biosynthesis (amino acids, nucleotides and glutathione) and as a signalling molecule.

We successfully exploit an integrated, Systems Biology approach to study nutritionally-perturbed transformed cells, pushing forward a system-level understanding of complex diseases like cancer.

5.2 INTRODUCTION

In the last decades, increasing attention has been directed to the dependency of some cancer cells on the conditionally essential amino acid glutamine [1,2,3,4]. Indeed, during situations of stress, the organism needs glutamine supplementation with the diet to satisfy the increased demand of this amino acid [1,2]. Similarly, rapidly growing cancer cells may display an increased glutamine consumption to sustain their fast proliferation and may die rapidly in the absence of glutamine [3]. Moreover, it has been shown that glutamine synthetase (GS) levels in glutamine-dependent cell lines are inversely correlated with sensitivity to glutamine deprivation [17]. As a metabolic precursor, glutamine is used for protein, RNA and DNA biosynthesis. Moreover, through the process known as glutaminolysis, glutamine generates ammonia and glutamate (GLU) that, in turn, can be catabolized to α-ketoglutarate (AKG) through either transamination or oxidative deamination. As such, glutamine participates in energy production and cellular redox homeostasis, being a precursor of the antioxidant glutathione [4]. As the carbon skeleton from glutaminolysis can be used for anabolic or anaplerotic processes, tumour cells may be addicted to glutamine as an alternative fuel (which is oxidized to CO2 for energy production), or because glutamine-derived AKG enters the TCA cycle to replenish metabolic intermediates removed for biosynthesis, particularly NADPH and fatty acids [5]. Alternatively, glutamine can undergo reductive carboxylation (RC), which consists in the reverse conversion of AKG into citrate through mitochondrial and

cytosolic isoforms of NADP+/NADPH-dependent isocitrate dehydrogenase. Subsequent metabolism of glutamine-derived citrate provides both the acetyl-CoA for lipid synthesis and the 4-carbon intermediates needed to produce remaining TCA cycle metabolites and related macromolecular precursors [6].

Besides playing a particularly important role in cell growth and metabolism, glutamine acts as a signalling molecule that ultimately activates a master regulator of protein translation, the mammalian target of rapamycin (mTOR) pathway [7,8]. mTOR is an atypical serine/threonine kinase that integrates several stimuli to regulate cell growth, metabolism, and aging [9]. Indeed, mTORC1 acts by phosphorylating multiple downstream targets, including the p70 ribosome protein S6 kinase (S6K1), that phosphorylates and activates ribosomal protein S6 (rpS6), a component of the 40S ribosomal subunit involved in the regulation of cell size and cell proliferation [10]. Although mTOR-signalling appears to respond most acutely to the essential amino acid leucine, glutamine uptake and export is required for EAA activation of mTORC1 [8,11].

We propose to dissect glutamine roles in cell proliferation by using K-ras-transformed NIH3T3 mouse fibroblasts (NIH-RAS) as cellular model, extensively characterized in our laboratory [12,13,14]. We feed glutamine-deprived NIH-RAS with dimethyl-alpha-ketoglutarate (AKG) –a membrane-permeable analogue of alpha-ketoglutarate- as carbon source and nonessential amino acids (NEAA: Pro, Ala, Asp, Asn) as nitrogen source, to

reconstitute glutamine and facilitate the understanding of its roles in sustaining cell growth. In a Systems Biology perspective, we study NIH-RAS cell metabolism with ENGRO metabolic model and –omics technologies, highlighting that glutamine owns multiple and unique roles in proliferating cells and may not be substituted by other nutrients, even if contained in its structure. Indeed, we demonstrate that glutamine is necessary to activate mTOR pathway and hence lipogenesis and, above all, to maintain redox homeostasis, allowing NIH-RAS cells to produce lipids through reductive carboxylation of glutamine and to provide a source of nitrogen for nucleotide biosynthesis.

5.3 RESULTS

5.3.1 Alpha-ketoglutarate and nonessential amino acids partly rescue glutamine deprivation in NIH-RAS cells

To study nutritional dependency of transformed cells, the first step usually consists in the analysis of physiological readouts, like cell proliferation and viability, under different nutrient perturbations. In this context, we first evaluated parental NIH3T3 and transformed NIH-RAS cell proliferation under glutamine deprivation and we observed that both NIH3T3 and NIH-RAS cell lines are glutamine-addicted, as they die in the absence of this amino acid (Supplementary Figure 3.S1 for NIH3T3 cells, Figure 5.1A for NIH-RAS cells, light blue line). This is in accordance with previous literature data [15].

Given that glutamine is a nitrogen and carbon source, we tried to substitute this amino acid with other nutrients having analogous function. Particularly, when glutamine is available in the medium, it is converted into glutamate and ammonium by glutaminase (GLS), then glutamate is converted into α-ketoglutarate and ammonium either by glutamate dehydrogenase (GDH) or transaminases (Figure 5.1B, left panel). As these reactions are reversible, we decided to supplement dimethyl-α-ketoglutarate (AKG) –a membrane-permeable analogue of α-ketoglutarate– and ammonium to glutamine-deprived NIH3T3 and NIH-RAS cells, in order to allow these cells to synthesize glutamine through glutamine synthetase (GS)-catalysed reaction (Figure 5.1B, right panel). As a source of ammonium, we provided NIH3T3 and NIH-

RAS with nonessential amino acids (NEAA: aspartate, asparagine, alanine, proline), since previous experiments demonstrated that supplementing ammonium sulfate or ammonium acetate to NIH3T3 and NIH-RAS cells resulted in cell toxicity and death (data not shown), differently from what happens in yeast.

Supplementing equimolar amounts of glutamate (GLU, 4 mM) to glutamine-depleted NIH3T3 and NIH-RAS did not rescue their growth ability (Supplementary Figure 3.S1 for NIH3T3 cells, Figure 5.1A for NIH-RAS cells, dark green line), as reported by Eagle [16] and, later, by Tardito [17]. Similarly, supplementing NEAA or AKG was ineffective in rescuing growth (Supplementary Figure 3.S1 for NIH3T3 cells, Figure 5.1A for NIH-RAS cells, yellow and light green lines, respectively).

Only co-supplementation of AKG AND NEAA (Supplementary Figure 5.S1 for NIH3T3 cells, Figure 5.1A for NIH-RAS cells, red line) restored cell growth and viability, but only in NIH-RAS cells. The apparent mass duplication time (MDT) of NIH-RAS in both these conditions was about 4.5 longer than in standard (STD) medium.

Due to the low number of NIH3T3 cells grown in –GLN+AKG+NEAA medium and to the ensuing low reliability of experimental results obtainable with such a small cell fraction, we decided to focus our attention on NIH-RAS cells and to analyse different parameters in these cells grown in STD versus –GLN+AKG+NEAA medium.

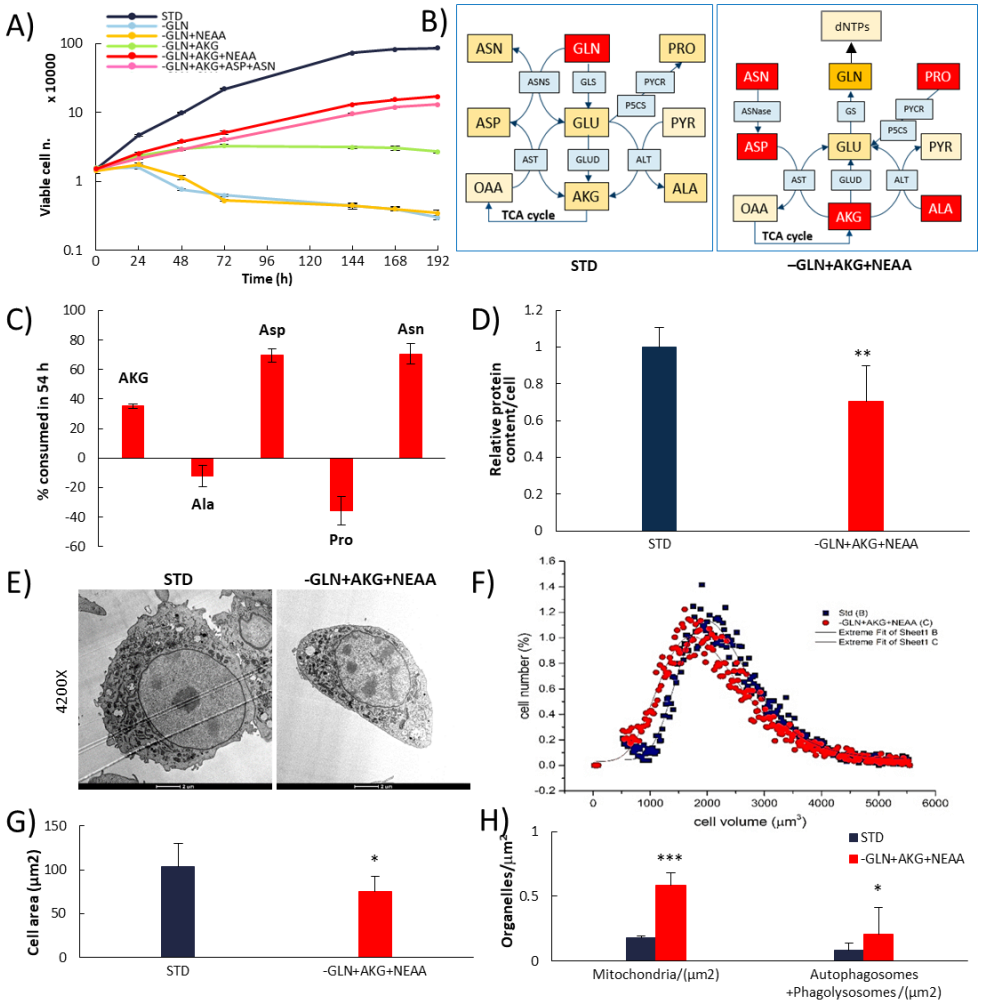

Figure 5.1 Proliferation and physiology of nutrient perturbed-mouse fibroblasts. (A) Growth kinetics of NIH-RAS cells grown under different nutrient conditions as indicated (STD: 4 mM Gln; AKG: 4 mM dm-aKG; NEAA: 4 mM Ala, 4 mM Asp, 4 mM Asn, 4 mM Pro; GLU: 4 mM Glu) and counted daily with trypan blue excluding method (semilog curves). (B) Representative scheme of cell metabolism in STD (left) and –GLN+AKG+NEAA (right) media. (C) AKG and NEAA consumption for NIH-RAS cells after 54 h of growth under conditions indicated. Measurements were made with GC-MS on fresh and spent media. (D) Cellular size of NIH-RAS cells grown in STD and –GLN+AKG+NEAA, determined by measuring protein content per cell

(Bradford assay). **P<0.01 (Student's t-test). (E) Representative images of electron microscopy (TEM) analysis of fixed NIH-RAS cells grown in STD and –GLN+AKG+NEAA media for 54 hours (magnification: 4200X). (F) Volumes distribution of NIH-RAS cells grown in STD and –GLN+AKG+NEAA, determined by Coulter Counter analysis (G) Cell area calculated on the pictures obtained from TEM analysis (H) Quantification of lipid droplets, mitochondria and autophagosomes made on the pictures obtained from TEM analysis.

We aimed to understand if NIH-RAS cells internalize and consume AKG and NEAA supplemented to the glutamine-free medium. NIH-RAS cells grown in –GLN+AKG+NEAA consume substantial amounts of AKG, Asp and Asn. Little if any consumption of Ala and Pro was detected, suggesting that Asp and Asn may be the only required amino acids to allow growth of NIH-RAS in glutamine-deprived media supplemented with AKG Figure 5.1C). This conclusion is supported by growth kinetics results (Figure 5.1A, fuchsia line).

Next, we analysed cell dimensions by measuring protein content per cell and cell volume and we found that NIH-RAS cells are significantly smaller when grown in –GLN+AKG+NEAA medium compared to STD medium (Figure 5.1D,5.1F).

This observation was confirmed by the TEM analysis of the intracellular morphology of NIH-RAS cells grown in STD and in –GLN+AKG+NEAA medium (Figure 5.1E,1G), in which glutamine-deprived NIH-RAS cells supplemented with AKG and NEAA display a higher number of mitochondria (Figure 5.1H).

5.3.2 Glutamine-deprived NIH-RAS cells supplemented with AKG+NEAA downregulate the expression of genes involved in lipogenesis

Transcriptomic analysis on NIH-RAS cells grown in STD and in –GLN+AKG+NEAA media revealed that only 115 genes are differentially expressed between the two nutritional conditions (Fold Change >1.5; corrected P value <0.05) (Figure 5.2A). The heat map in Figure 5.2A shows the hierarchical clustering of such differentially expressed genes (DEGs), represented in green if downregulated in NIH-RAS cells grown in –GLN+AKG+NEAA medium, while in red if upregulated. As STRING and Panther analyses revealed (Figure 5.2B and C, respectively), most of the DEGs deal with metabolism, especially cholesterol biosynthesis and transport. Other identified DEGs are involved in the response to the oxidative stress induced by nutrient deprivation, like that mediated by p53 signalling pathway, and in cell cycle, like the downregulated Cdkn1a gene.

To integrate transcriptomic data and deepen the aspect of the strong impact on metabolism induced by growth in –GLN+AKG+NEAA medium, a computational analysis was carried out to identify the "reporter metabolites" (Figure 5.2D; see Materials and Methods for the reporter metabolite identification process). Reporter metabolites are those spots in the metabolism where there is a substantial regulation either to maintain homeostasis (i.e. a constant metabolite level) or adjust the concentration of the metabolite to another level required for proper

functioning of the metabolic network. Thus, the identification of reporter metabolites adds knowledge to the pathway analysis shown in Figure 5.2C, as it considers the information on the connectivity and the magnitude of the significance of change for differentially expressed genes. Moreover, reporter metabolite analysis also takes into account genes not differentially expressed, which can exhibit significant coordinated changes when considered together.

Reporter metabolite analysis confirmed that most of the downregulated genes in cells grown in –GLN+AKG+NEAA medium deal with lipid synthesis, especially cholesterol synthesis and transport (Figure 5.2D), which is a process that requires a high amount of NADPH. In this regard, the most relevant reporter metabolite (i.e. to which the highest normalized score is associated) was NADP –either in its reduced or oxidized form- (Figure 5.2D), suggesting potential differences in redox state between NIH-RAS cells grown in STD medium and glutamine-deprived NIH-RAS cells.

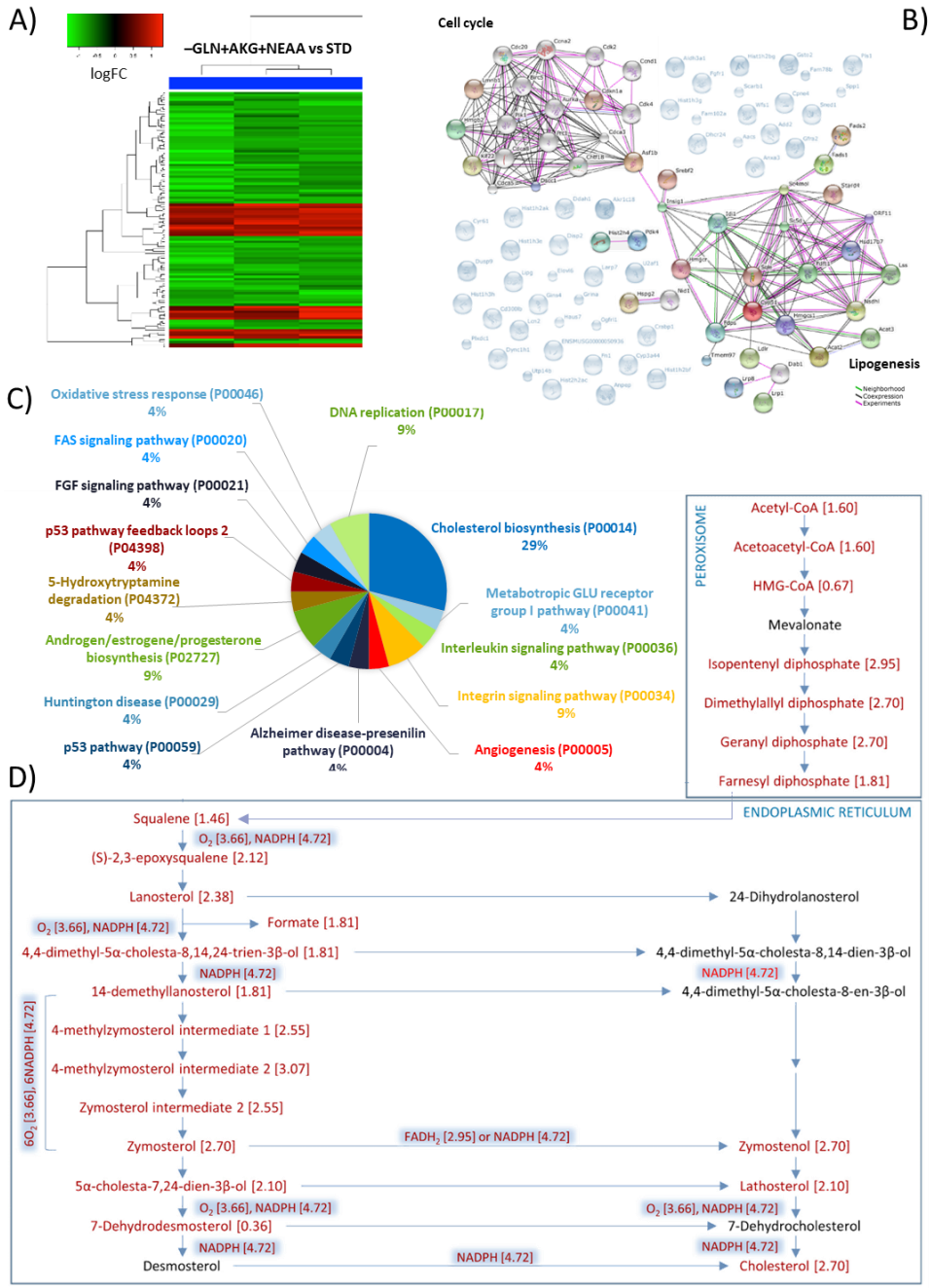

Figure 5.2 Transcriptional profile of NIH-RAS cells under nutrient perturbation.

(A) Heat map of significant DEGs (115; FC>1.5; corrected P value<0.05) in NIH-RAS

grown in –GLN+AKG+NEAA versus STD media. (B) STRING analysis of putative interactions between the identified DEGs. (C) List of pathways affected by the identified DEGs (Panther analysis). (D) Main reporter metabolites (RM) mapped in red on steroid biosynthetic pathway. In parenthesis: normalized score for each RM.

To validate transcriptomic data, we performed quantitative real-time PCR analyses on some differentially expressed genes, important in cell cycle and metabolism, particularly in lipid metabolism (Figure 5.3A). Then, we analysed cell cycle in NIH-RAS cells grown in STD and –GLN+AKG+NEAA media by co-labelling cells with anti-BrdU and anti-Ki67 antibodies (two markers of cell proliferation) (Figure 5.3B). In line with the reduction of mass duplication time (MDT) of NIH-RAS cells grown in –GLN+AKG+NEAA medium (Figure 5.1A), we obtained a lower growth fraction in nutritionally-perturbed condition. Finally, we measured lipid and cholesterol levels in STD and –GLN+AKG+NEAA media, confirming a lower lipid content (Figure 5.3C-D) and a reduction of 40% of cholesterol levels under glutamine deprivation (Figure 5.3E).

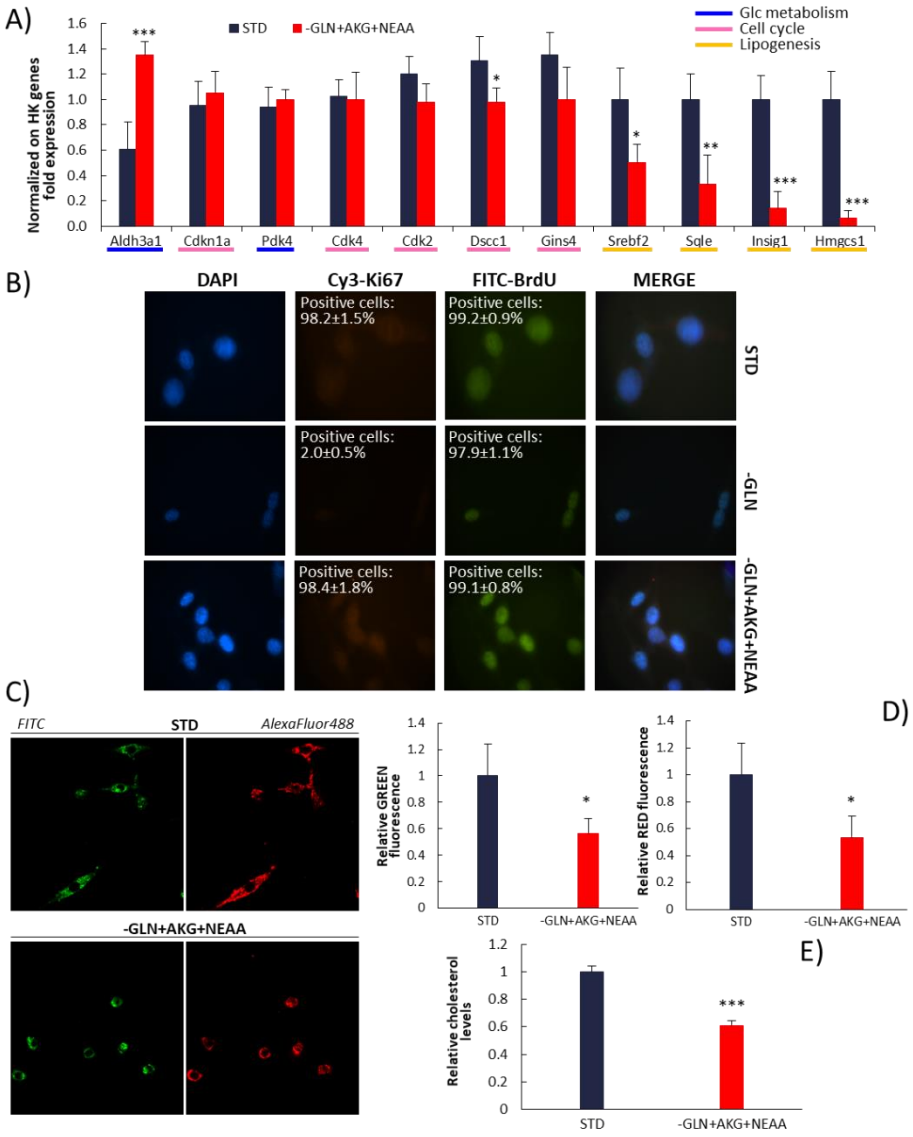

Figure 5.3 Glutamine-deprived NIH-RAS cells supplemented with AKG and NEAA downregulate cell cycle and lipogenesis. (A) Quantitative real-time PCR analysis of the expression of those genes found differentially expressed in the transcriptomics analysis (see Figure 4). (B) Fluorescence microscopy analysis of cell cycle phase of NIH-RAS cells grown under conditions indicated and hybridized with antibodies against Ki67 (marker for all cell cycle phases except for G0 phase) and BrdU

(marker of S-phase). (C-D) Nile Red staining of lipids in NIH-RAS cells grown in STD and –GLN+AKG+NEAA media. Cells were analyzed with confocal microscope (60X magnification) and photos were taken after exciting with FITC (left) and AlexaFluor488 channels (right). Green and red cell fluorescences integrated on cell area were determined using ImageJ software and plotted in the histograms (D). (E) Cholesterol levels in NIH-RAS cells grown in STD and –GLN+AKG+NEAA media, measured with Total Cholesterol Assay kit (Cell Biolabs). *P<0.05; **P<0.01; ***P<0.001 (Student's t-test).

5.3.3 AKG and NEAA mitigate oxidative stress and redox unbalance induced by glutamine deprivation in NIH-RAS cells.

As mentioned above, computational analyses on transcriptomic data suggested that NIH-RAS cells grown in STD and in –GLN+AKG+NEAA media may differ in terms of redox potential (Figure 5.2D). Thus, we wanted to explore this aspect, as well as to further validate transcriptomic results.

As expected from reporter metabolites analysis (Figure 2D), we found a different NADPH content in NIH-RAS cells grown in STD and in –GLN+AKG+NEAA media. Particularly, glutamine-deprived NIH-RAS cells supplemented with AKG and NEAA display 40% of NADPH when compared to the same cells grown in STD medium (Figure 5.4A).

According to literature data on K-ras-transformed cell lines [19], we found that glutamine deprivation enhances oxidative stress in NIH-RAS cells, and supplementation of AKG or NEAA partly decreases ROS levels, especially when combined in the –GLN+AKG+NEAA medium (Figure 5.4D).

Measuring reduced glutathione (GSH) and total glutathione (GSH+GSSG) levels (Figure 5.4-C), we found that glutamine deprivation leads to decreased GSH and GSH+GSSG levels, due to the lack of glutamate (and ensuing glutathione) precursor glutamine. As seen for ROS levels, supplementation of AKG or NEAA –but above all their combination- partly restores basal

H)

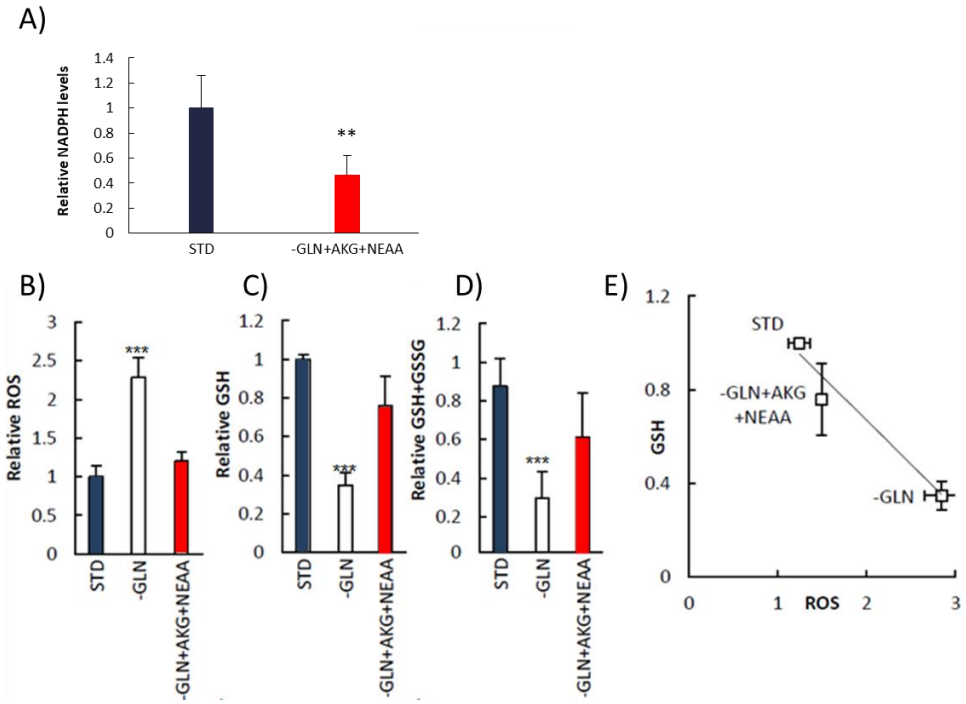

GSH and GSH+GSSG levels. According to the role of ROS scavenger that glutathione in the reduced form has [20], we obtained a negative correlation between ROS and GSH levels (Figure 5.4E)

Figure 5.4 Redox state of NIH-RAS cells is altered when grown in –GLN+AKG+NEAA medium. (A) NADPH levels of NIH-RAS cells grown under conditions indicated as determined with NADP/NADPH Quantitation Kit (BioVision). *P<0.05; **P<0.01 (Student's t-test). (B) Relative ROS levels in NIH-RAS cells grown for 54 h under conditions indicated as determined by DCFDA staining. Each bar represents the mean of at least three independent experiments with error bars representing the standard deviation. (C) Reduced glutathione levels measured after 54 h from medium change as described in Rahman et al. 2006. Each bar represents the mean of at least three independent experiments with error bars representing the s.d. (D) Total glutathione levels measured after 54 h from medium change as described in Rahman et al. 2006. Each bar represents the mean of at least three independent experiments with error bars representing the s.d. (E) Negative correlation between reduced glutathione levels and ROS levels.

5.3.4 Glutamine-deprived NIH-RAS cells supplemented with AKG and NEAA show an increased mitochondrial respiration

As a first attempt to study NIH-RAS cell metabolism, we analysed glycolysis and oxidative phosphorylation (OXPHOS), the two major mechanisms in mammalian cells to produce ATP [Zhang et al. 2012]. Specifically, we measured the extracellular acidification rate (ECAR), which approximates glycolytic activity under certain conditions, and the mitochondrial oxygen consumption rate (OCR), which is a key metric of mitochondrial function. The increased ratio of OCR to ECAR in NIH-RAS cells grown in –GLN+AKG+NEAA medium compared to that of NIH-RAS cells grown in STD medium may indicate cellular preference for OXPHOS versus glycolysis when mitochondria are coupled for oxygen consumption and energy generation through ATP synthase activity (Figure 5.5A).

A lower diversion of glucose into lactate may also derive from the increased reliance of NIH-RAS cells on glucose to produce essential building blocks –like amino acids- in the absence of glutamine. Thus, we analysed fresh and spent media to measure glucose consumption (and subsequent lactate production), finding that NIH-RAS grown in –GLN+AKG+NEAA may consume a little less glucose (and produce a little less lactate). However, the differences are minor and unlikely to be significant. On the

contrary, cells grown in –GLN+AKG+NEAA produce and secrete large quantities of glutamate (Figure 5.5B).

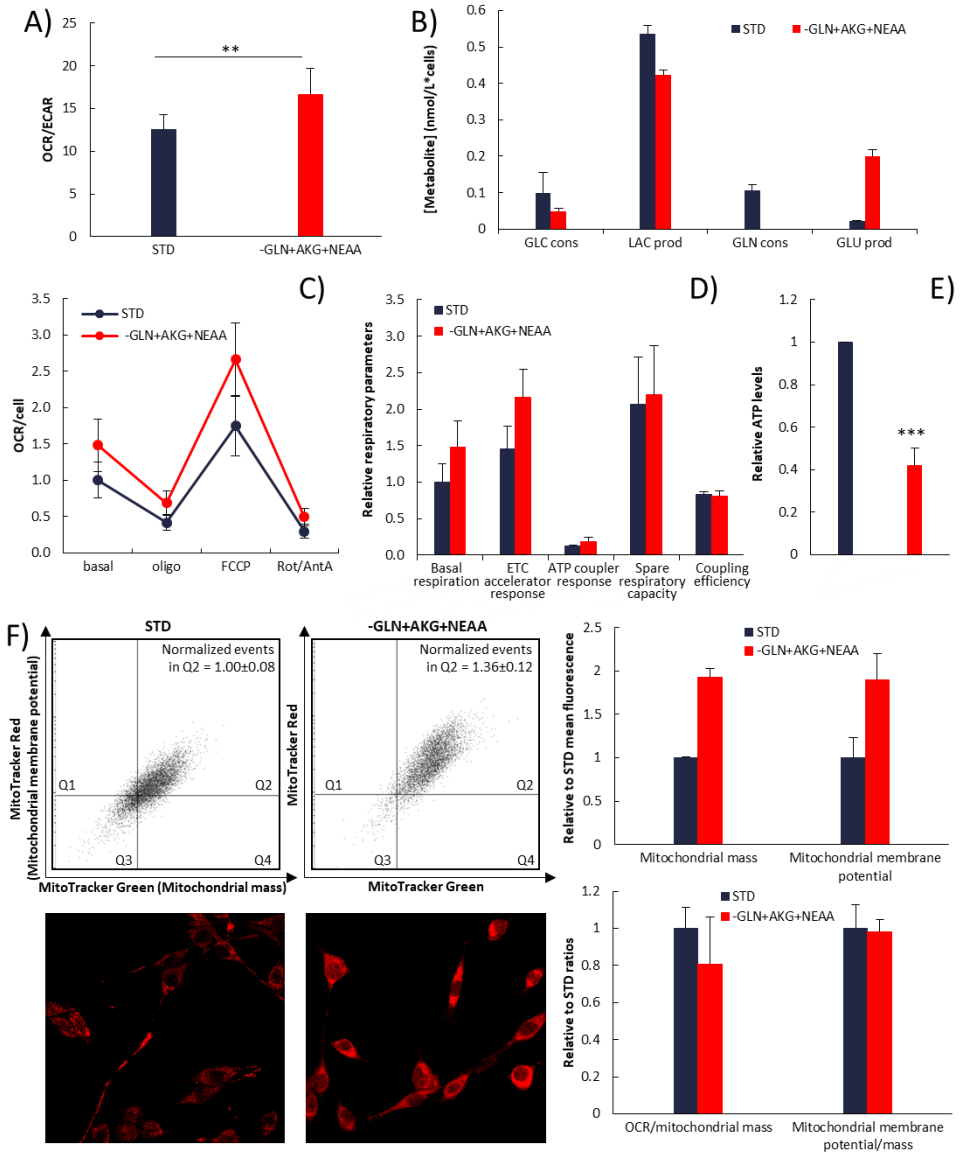

Figure 5.5 Glutamine-deprived NIH-RAS cells supplemented with AKG and NEAA decrease lactate production while enhancing oxygen consumption to sustain an increased use of ATP. (A) Ratio between Oxygen Consumption Rate (OCR) and

Extracellular Acidification Rate (ECAR) of nutritionally-perturbed NIH-RAS cells measured using the XF24 Extracellular Flux Analyzer under basal conditions. Results derive from 2 independent experiments each performed in 7 replicates. (B) Glucose and glutamine consumption and lactate and glutamate production under conditions indicated measured with YSI Analyzer. (C-D) Response to oligomycin, FCCP and rotenone/antimycin A treatment (C) and relative respiratory parameters (D) of NIH-RAS cells grown in STD and –GLN+AKG+NEAA media measured during a MitoStress Test performed with the XF24 Extracellular Flux Analyzer (Seahorse Biosciences). (E) Relative ATP levels in NIH-RAS cells grown in STD and –GLN+AKG+NEAA media for 54 h, measured by Victor (Perkin Elmer) after using ATPLite Assay Kit (Perkin Elmer). (F) MitoTracker Red and MitoTracker Green analysis of mitochondria of NIH-RAS cells grown in STD and –GLN+AKG+NEAA media, measured by FACS and –for MitoTracker Red- with a confocal microscope. **P<0.01; ***P<0.001 (Student's t-test).

First, as low energy levels may contribute to the slow growth of glutamine-deprived NIH-RAS cells, we measured ATP content, which was reduced of about 50% in glutamine-deprived NIH-RAS compared to NIH-RAS grown in STD medium (Figure 5.5D).

5.3.5 Glutamine-deprived NIH-RAS cells do not follow reductive carboxylation of AKG and divert Glucose and NEAA mainly to glutamate production

We analysed metabolic profile of NIH-RAS cells grown in STD and in –GLN+AKG+NEAA media with GC/MS technology. As Figure 5.6A shows, in –GLN+AKG+NEAA condition we observed a vast downregulation of metabolites when compared to STD media. Metabolites like Glucose, cytosine and Erythrose-4-Phosphate, Citrate were present in higher level in –GLN+AKG+NEAA condition, whereas Malate, Asparate, Serine,

glycine etc were downregulated when compared to STD condition. Increased glucose and Citrate levels could indicate the comping mechanism under glutamine deprivation in order to maintain energy homeostasis and the data correlated with the transcriptomic analysis where increased expression of genes involved in glucose metabolism was observed in –GLN+ALG+NEAA condition (Figure 5.6A). Pathway enrichment analysis of the metabolites downregulated and upregulated in –GLN+AKG+NEAA condition reveal downregulation of metabolites belonging to pathways of Urea cycle, Ammonia recycling, glutamate metabolism, alanine and amino sugar metabolism (Figure 5.6B), whereas enrichment of pathways Transfer of Acetyl group to mitochondria, fatty acid biosynthesis, glycolysis, citric acid cycle, (Figure 5.6C), indicating higher mitochondrial engagement and thus coinciding with higher mitochondrial number as well as activity observed earlier (Figure 5.5). The higher amount of Fatty acids like Palmitic acid, Stearic acid and caprylic acid observed in –GLN+AKG+NEAA condition contradicts with findings of transcriptomic analysis where decrease expression of genes involved in lipogenesis was observed. This difference in metabolic level and transcriptomic level could be due to higher accumulation of these fatty acids as a result of impaired metabolism in –GLN+AKG+NEAA condition, rather than caused by increased synthesis.

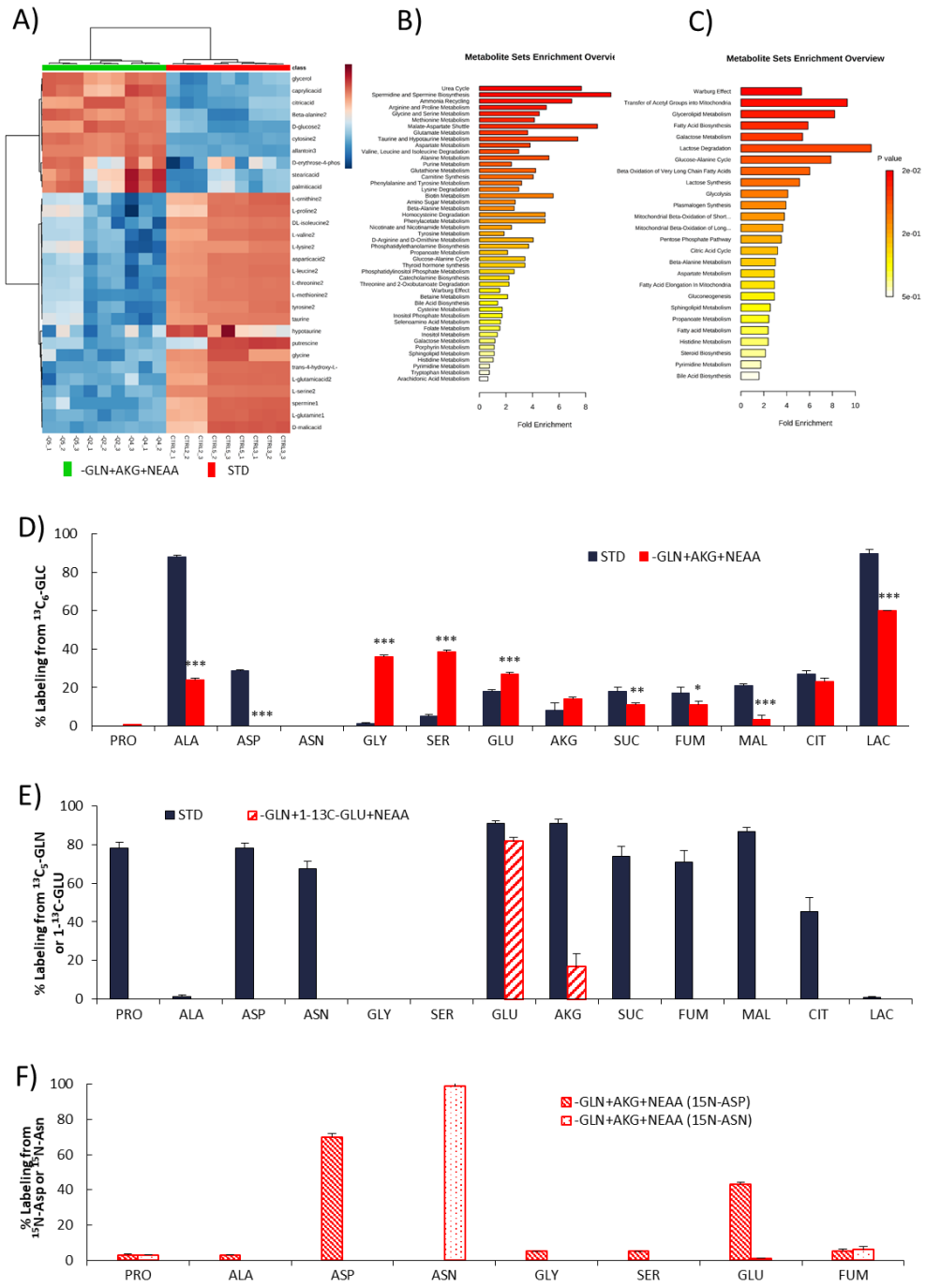
A)
B)
C)
Metabolite Sets Enrichment Overvie
Metabolite Sets Enrichment Overview
P value
Fold Enrichment
-GLN+AKG+NEAA
STD
D)
% Labeling from $^{13}C_6$-GLC
STD
-GLN+AKG+NEAA
PRO
ALA
ASP
ASN
GLY
SER
GLU
AKG
SUC
FUM
MAL
CIT
LAC
E)
% Labeling from $^{13}C_5$-GLN or 1-^{13}C-GLU
STD
-GLN+1-13C-GLU+NEAA
F)
% Labeling from ^{15}N-Asp or ^{15}N-Asn
-GLN+AKG+NEAA (15N-ASP)
-GLN+AKG+NEAA (15N-ASN)

Figure 5.6 Metabolome and metabolic fluxes of NIH-RAS cells under nutrient perturbation. (A) Heatmap of Metabolic profile of NIH-RAS cells grown in Std and in –GLN+AKG+NEAA for 54 h, analyzed with GC-MS. (B) Pathway enrichment of metabolites downregulated in –GLN+AKG+NEAA condition (C) Pathway enrichment of metabolites upregulated in –GLN+AKG+NEAA condition (D) Percentage of metabolite labelling from [U-$^{13}C_6$]glucose in NIH-RAS cells grown in STD and –GLN+AKG+NEAA conditions. The analysis was made with GC-MS on NIH-RAS cells grown for 54 h. NA = not applicable, due to isotope dilution by external addition of NEAAs. (E) Percentage of metabolite labelling from [U-$^{13}C_5$]glutamine (for STD medium) or from [1-^{13}C]glutamate (for –GLN+GLU+NEAA medium) analyzed with GC-MS after 54 h of cell growth. (F) Percentage of metabolite labelling from [^{15}N]aspartate and from [^{15}N]asparagine in NIH-RAS cells grown for 54 h in –GLN+AKG+NEAA medium, measured with GC-MS.

Next, we analyzed the fluxome of NIH-RAS cells grown in STD and in –GLN+AKG+NEAA media to understand if glucose (another major nutrient source for transformed cells) is diverted to other pathways to sustain growth when cells are glutamine-deprived and to understand if supplements AKG and NEAA under glutamine deprivation follow the same metabolic pathways as glutamine.

First, we provided NIH-RAS cells grown in STD and –GLN+AKG+NEAA media with [U-$^{13}C_6$]-Glucose, finding that, compared to STD medium labelled glucose is preferentially converted to serine, glycine and glutamate in –GLN+AKG+NEAA medium and less converted to lactate (Figure 5.6D). This was further validated from the lower M+3 labelled lactate derived from [U-$^{13}C_6$]-Glucose in –GLN+AKG+NEAA condition (Figure 5.7). –GLN+AKG+NEAA showed higher M+3 labelled pyruvate indicating higher flux towards glucose to

pyruvate and correlating with higher glycolysis observed from metabolomics analysis (Figure 5.7).

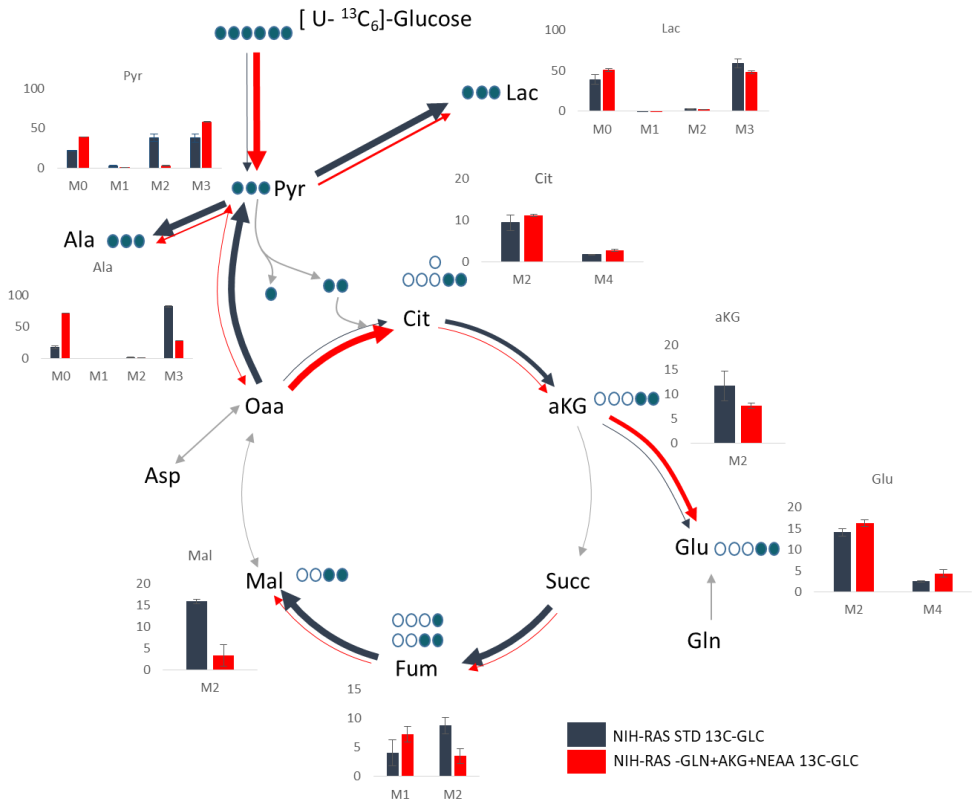

Figure 5.7 Flux map of NIH-RAS cells under nutrient perturbation. Metabolic flux map depicting major flux distribution obtained through [U-$^{13}C_6$]-Glucose in STD and –GLN+AKG+NEAA condition. Blue arrows depict flux for NIH-RAS cells grown in STD media whereas Red arrows represent flux for NIH-RAS cells grown under –GLN+AKG+NEAA condition. The thickness of the arrows represent the condition with higher or lower flux where thicker arrows represent higher flux for the specific reaction. Grey arrows represent fluxes not resolved using [U-$^{13}C_6$]-Glucose. Blue bubbles represent the most abundant labelling pattern obtained using [U-$^{13}C_6$]-Glucose.

–GLN+AKG+NEAA condition also showed significant decrease in flux from pyruvate to alanine correlating with metabolomic

analysis (Figure 5.6B) whereas higher pyruvate carboxylase flux was observed in cells grown in STD condition (Figure 5.7). Cells grown in –GLN+AKG+NEAA showed higher M+2 & M+4 citrate labelling via [U-$^{13}C_6$]-Glucose suggesting higher citrate synthase flux and higher utilization of acetyl Co-A into mitochondria, similarlily higher M+2 and M+4 labelling was observed in Glutamate indicating utilization of glucose for glutamate synthesis. Forward TCA cycle flux was slower in –GLN+AKG+NEAA condition observed by lower M+4 labellin of Succicate, Fumarate and Malate (Figure 5.7). The enhanced growth of RAS transformed cells possibly due to WarburQ effect [22] the evidence of which can be observed from higher fluxes in reactions catalysed by succicate dehydrogenase, fumarase, pyruvate carboxylase and lactate dehydrogenase leading to higher lactate secretion supported by TCA cycle in STD condition (Figure 5.7) is lost when grown in –GLN+AKG+NEAA condition.

Then, we provided [U-$^{13}C_5$]-glutamine to NIH-RAS cells grown in STD medium (Figure 5.6E). Compared to what seen for glucose, NIH-RAS cells showed a higher use of glutamine for the synthesis of TCA cycle intermediates and for NEAA biosynthesis (with the exception of glucose-derived alanine), while lactate fully derived from glucose rather than from glutamine.

Likewise, we provided [1-^{13}C]-glutamate -and NEAA- to glutamine-deprived NIH-RAS cells. Strikingly, about 80% of the glutamate was still [1-^{13}C]-labelled<, suggesting that glutamate

may not be converted to other metabolites under glutamine deprivation (Figure 5.6C).

Finally, we provided NIH-RAS cells grown in –GLN+AKG+NEAA medium either with [^{15}N]-aspartate or with [^{15}N]-asparagine (the only NEAA that enter NIH-RAS cells) to follow their intracellular destiny. While asparagine is not used to synthesize other molecules, aspartate is mainly used to produce glutamate, since 43% of glutamate is 15N-labelled (Figure 5.6F).

Previous results on NIH-RAS cell metabolism [21] suggested that glutamine reductive carboxylation (RC) through the aconitase-catalyzed reaction is a marker of the enhanced growth of NIH-RAS cells when compared to their parental NIH3T3 normal cell line. Therefore, we performed a series of Flux Balance Analysis (FBA) simulations on the model on central carbon metabolism ENGRO introduced in [22] by maximizing the backward direction of the aconitase–catalyzed reaction in both STD and –GLN+AKG+NEAA conditions. The aim of the analysis was to investigate the compatibility of the two growth conditions with the possibility of undergo RC. Figure 5.8A-B shows that when the backward direction of aconitase-catalyzed reaction is maximized, NIH-RAS cells grown in –GLN+AKG+NEAA medium are less capable of relying on RC for fatty acid synthesis. Indeed, the aconitase-catalyzed reaction displays a much higher flux value for NIH-RAS cells grown in STD medium than for glutamine-deprived NIH-RAS cells. Furthermore, FBA experiments highlighted that recurring to RC in –GLN+AKG+NEAA growth

condition implies a 62%-reduction of biomass synthesis flux with respect to growth in STD medium, according to experimental observations (Figure 5.1B).

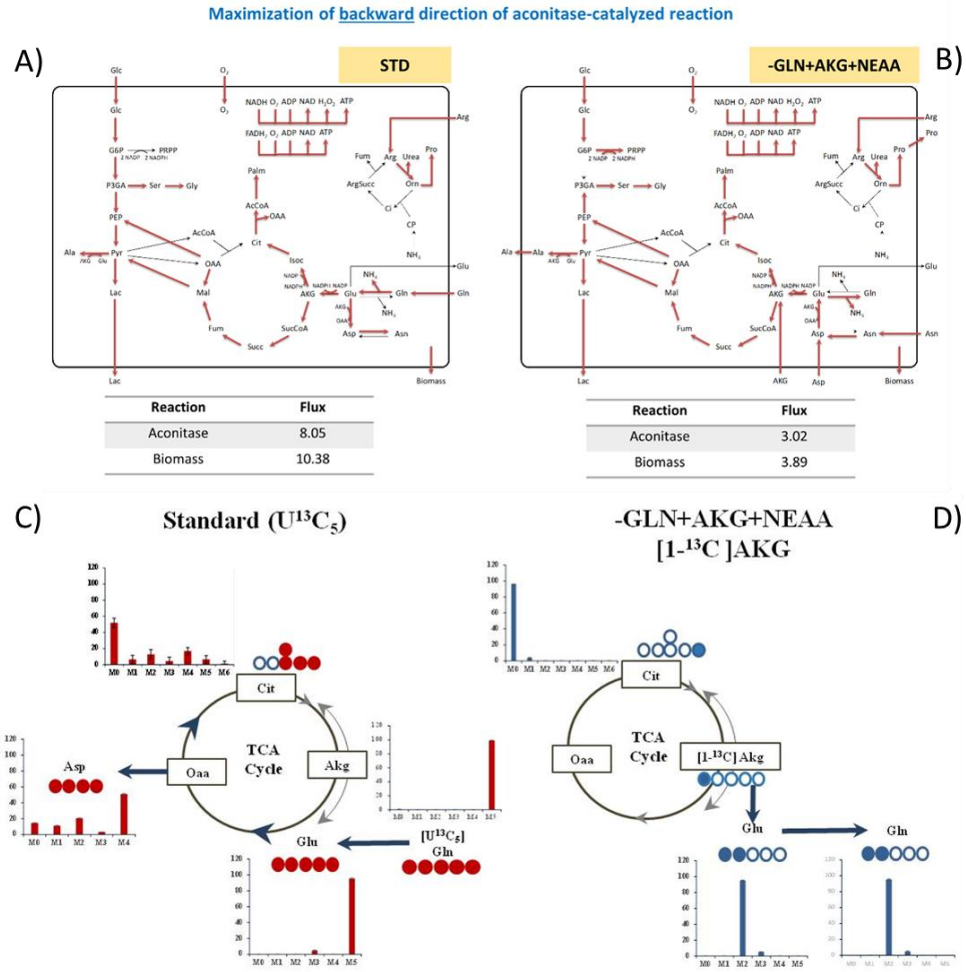

Figure 5.8 Utilization of reductive carboxylation (RC) pathway in NIH-RAS cells under nutrient perturbation. (A-B) Flux balance analysis (FBA) experiments on ENGRO network to maximize the backward direction of the aconitase-catalyzed reactions for NIH-RAS cells grown in STD (A) and –GLN+AKG+NEAA (B) media. (C) Map and experimental values of labelling destiny when [U-$^{13}C_5$]glutamine is

metabolized both reductively and oxidatively (for STD medium). (D) Map and experimental values of labelling destiny when [1-^{13}C]alpha-ketoglutarate is metabolized oxidatively (for –GLN+AKG+NEAA medium).

To validate computational results, we provided [U-$^{13}C_5$]-glutamine to NIH-RAS cells grown in STD medium (Figure 5.8C), founding that glutamine-derived labelled AKG undergoes both RC and forward TCA cycle. Indeed, both citrate M4 isotopomer (i.e. with 4 labelled carbon atoms, typical of oxidative metabolism) and citrate M5 isotopomer and M3 fumarate, M3malate and M3 aspartate (typical of reductive metabolism) are generated, in line with previous results [19].

On the contrary, as predicted by ENGRO model, we demonstrated that [1-^{13}C]-AKG in glutamine-deprived NIH-RAS cells only follow very significantly reduced RC, since neither TCA intermediates nor citrate were labelled (labelled carbon atom is indeed lost as CO2 in the decarboxylation step from AKG to succinyl-CoA) (Figure 5.8D). Surprisingly we observe a very high M2 labelling of glutamate and glutamine from [1-^{13}C]-AKG suggesting the conversion of aKG to glutamate, but exact mechanism needs to be resolved.

5.4 DISCUSSION

Growing cancer cells often depend on glutamine, some cell lines dying rapidly when deprived of this amino acid [3,4]. Glutamine concentration modulates the cancer phenotype of K-ras-transformed mouse fibroblasts [15]. Here we show that these cells are addicted to glutamine, since cells depleted of this amino acid stop growth and rapidly loose viability. Glutamine is composed by alpha-ketoglutarate and ammonium. Addition of these compounds (AKG+NEAA medium) to glutamine-deprived NIH-RAS cells restores viability, but cell proliferation is strongly hindered, cells being reduced in size and slow growing (Fig.5.1). Transcriptional analysis of AKG+NEAA-grown vs standard medium-grown NIH-RAS cells indicates limited differences in gene expression, mostly limited to genes involved in lipogenesis and – to a lesser extent – in cell cycle. Computational analysis that mapped expression data onto a genome-wide metabolic model highlighted NADPH as a major reporter metabolite. Biochemical assays of NADPH levels and lipid (including cholesterol) content validated these results. Our group previously showed using computational flux balance analysis (FBA) validated by experimental data, that NIH-RAS cells use intense aerobic glycolysis and glutamine reductive carboxylation as the fittest emergent strategy to support cell growth. When grown in AKG+NEAA medium, NIH-RAS cells largely revert their Warburg phenotype (Fig. 5.5) and no longer use AKG to fuel fatty acid biosynthesis through reverse carboxylation. FBA confirmed that when AKG + NEAA is used, attempts to maximize reverse carboxylation results in poor

biomass accumulation. Consistently with partial recovery of proliferation rate of NIH-RAS grown in AKG+NEAA medium by glutamine synthase overexpression, FBA data indicate that decreasing the glutamine synthase flux has strong impact on biomass accumulation in NIH- RAS cells when AKG+NEAA are used as growth substrates (data not shown).

In summary, these results reinforce the notion that glutamine supports the Warburg effect in hyperglycolytic cancer cells. They further indicate that, because of limiting glutamine synthase activity (data not shown), AKG+NEAA induces a large metabolic rearrangement that includes decreased accumulation of lipids – linked a drop in AKG reverse carboxylation – and NADPH, a decrease in fermentation and up-regulation of respiration (reverse Warburg effect).

As confirmed by FBA computational experiments, these rearrangements lead to a slow growth phenotype (decreased biomass accumulation in FBA terms). Once confirmed in human cancer cell lines, these studies will provide useful in deigning clinical protocols that make use of drugs directed against glutamine metabolism [4].

5.5 MATERIALS & METHODS

5.5. 1 Cell culture

Two cell lines have been used in this work, namely normal NIH3T3 mouse fibroblasts (obtained from the ATCC, Manassas, VA, USA) and a K-Ras-transformed normal-derived cell line –that we refer to as NIH-RAS. Both control and ras-transformed NIH3T3 have been passaged a similar number of times, taking care to refreeze the cell lines immediately and to use them for a limited number of passages. The cell lines are periodically assayed to check that the major properties of the cells do not change over time, that the major transformation-related phenotypes are retained and ras-dependent. The cell lines were routinely grown in Dulbecco's modified Eagle's medium (Invitrogen Inc., Carlsbad, CA, USA) containing 10% newborn calf serum (NCS), 4 mM glutamine, 100 U/ml penicillin and 100 mg/ml streptomycin, that we refer to as standard medium (STD), at 37°C in a humidified atmosphere of 5% CO2. Cells were passaged using trypsin-ethylenediaminetetraacetic acid (EDTA) (Invitrogen Inc., Carlsbad, CA, USA) and maintained in culture before experimental manipulation.

5.5.2 Cell proliferation analysis

Cells were plated at the density of 3000 cells/cm2 in standard medium and incubated overnight at 37°C and 5% CO2. After 18 h, cells were washed twice with phosphate-buffered saline (PBS) and, to verify the response to glutamine deprivation, cells were incubated in medium without glutamine (Invitrogen Inc.,

Carlsbad, CA, USA), possibly supplemented with dimethyl-2-oxoglutarate (AKG, 4 mM, Sigma Aldrich Inc.) or glutamate (GLU, 4 mM, Sigma Aldrich Inc.) and/or nonessential amino acids (Pro, Ala, Asp, Asn, 4 mM each, Sigma Aldrich Inc.).To measure cell proliferation, cells were treated with trypsin at 0, 24, 48, 54, 72, 144, 168, 192, 240 and 312 hours after medium change. Viable (i.e., unstained) cells were counted in a Bürker chamber after staining with 0.5% trypan blue.

5.5.3 Apoptosis Assay

Cells were plated at the density of 3000 cells/cm2 in standard medium and incubated overnight at 37°C and 5% CO2. After 18 h, cells were washed twice with PBS and incubated for 30 hours in medium without glutamine (Invitrogen Inc., Carlsbad, CA, USA), supplemented with dimethyl-2-oxoglutarate (AKG, 4 mM, Sigma Aldrich Inc.) and nonessential amino acids (Pro, Ala, Asp, Asn, 4 mM each, Sigma Aldrich Inc.). For apoptosis analysis, 1×106 cells (adherent and in suspension cells) were collected, stained with Annexin V-FITC (Immunotools, GmbH) and propidium iodide (Sigma Aldrich Inc.) and analyzed by FACScan (Becton-Dickinson) using the FL1 and FL2 channels. Data analysis was performed with Flowing Software.

5.5.4 Autophagy assay

Autophagy was determined by using Autophagy Assay Kit (Sigma Aldrich Inc.) following manufacturer's instructions. Briefly, NIH-RAS cells that had to be grown in STD medium were plated at

3000 cells/cm2, while NIH-RAS cells that had to be grown in –GLN+AKG+NEAA medium were plated at 9000 cells/cm2 in glass bottom petri dishes, suitable for confocal microscopy, with normal growth medium (STD). After 18 h at 37°C and 5% CO2, cells were rinsed twice with PBS and medium change was done, by incubating cells for 24 h with STD or –GLN+AKG+NEAA media. Cells were then incubated with the Autophagosome Detection Reagent working solution for 30 minutes in a 37°C in a 5% CO2 incubator and washed 4 times with wash buffer. Cells were imaged immediately under a confocal microscope with a DAPI channel.

5.5.5 Cell size measurement

NIH-RAS cells were plated at 3000 cells/cm2 (for 54 h-growth in STD and for 144 h-growth in –GLN+AKG+NEAA) and at 9000 cells/cm2 (for 54 h-growth in –GLN+AKG+NEAA) in 6-well plates in STD medium and incubated overnight at 37°C and 5% CO2. After 18 h, cells were washed twice with PBS and incubated for 54 h and 144 h in STD medium or in –GLN+AKG+NEAA medium. Cells were then 1) trypsinized and counted in a Bürker chamber (Trypan blue excluding method) and 2) scraped in lysis buffer to measure protein content with Bradford assay [28]. The resulting protein content was then normalized on cell number for both nutritional conditions (STD and –GLN+AKG+NEAA) to get the protein content per cell, which is an indicator of cell size.

5.5.6 Determination of intracellular ROS

Intracellular accumulation of H2O2 and O2•- was determined after 54 h from medium change with 2',7'-dichlorodihydrofluoresceine diacetate (Sigma Aldrich Inc.). The cells were incubated for 30 minutes at 37°C with H2DCFDA 10 mM, treated with trypsin, resuspended in PBS supplemented with NCS 10% (Invitrogen Inc., Carlsbad, CA, USA) and acquired by FACScan (Becton-Dickinson), using the Cell Quest software (BD Bioscience). The percentage of ROS producing cells was calculated for each sample and corrected for autofluorescence obtained from samples of unlabelled cells.

5.5.7 Determination of glutathione levels

For reduced and total glutathione measurements, cells were plated at the density of 3000 cells/cm2 in standard medium and incubated overnight at 37°C and 5% CO2. After 18 h, cells were washed twice with PBS and incubated for 54 h in STD medium or in medium without glutamine (Invitrogen Inc., Carlsbad, CA, USA), possibly supplemented with dimethyl-2-oxoglutarate (AKG, 4 mM, Sigma Aldrich Inc.) and/or nonessential amino acids (Pro, Ala, Asp, Asn, 4 mM each, Sigma Aldrich Inc.). Cells were then treated with trypsin, collected, washed twice with PBS and lysed through freeze-and-thaw cycles. Samples were deproteinized with a 5% 5-sulfosalicylic acid solution, centrifuged to remove the precipitated protein and assayed for glutathione. GSH measurement was an optimization of Tietze's enzymatic recycling method [23], in which GSH is oxidized by the sulfhydryl reagent

5,5'-dithio-bis (2-nitrobenzoic acid) (DTNB) to form the yellow derivative 5'-thio-2-nitrobenzoic acid (TNB), measurable at 412 nm and the glutathione disulfide (GSSG) formed is recycled to GSH by glutathione reductase in the presence of NADPH. The amount of glutathione in the samples was determined through a standard curve of reduced glutathione. Glutathione levels were normalized to protein content measured by Bradford assay (Bio-Rad reagent) on an aliquot of cell extract collected before deproteinization.

5.5.8 NADPH levels

The measurement of NADPH levels of NIH-RAS grown in STD, –GLN+AKG+NEAA and –GLN+GLU+NEAA media was made using NADP/NADPH Quantification Colorimetric Kit (BioVision), following manufacturer's instructions. Cells were seeded at the density of 3000 cells/cm2 (for growth in STD medium) and 9000 cells/cm2 (for growth in –GLN+AKG+NEAA and –GLN+GLU+NEAA media) in 150-mm dishes in STD medium and incubated overnight at 37°C and 5% CO2. After 18 h, cells were washed twice with PBS and incubated for 54 h in STD, –GLN+AKG+NEAA or –GLN+GLU+NEAA media. The day of the analysis, cell metabolism was quenched with liquid nitrogen and cells were lysed with NADP/NADPH Extraction Buffer provided with the kit. After following the protocol, NADPH and NADP+NADPH were quantified by reading the absorbance of the samples at 450 nm and comparing it with NADPH standard curve.

5.5.9 Cholesterol levels

Cholesterol levels of NIH-RAS grown in STD and –GLN+AKG+NEAA media were measured by using Total Cholesterol Assay Kit, Colorimetric (Cell Biolabs), following manufacturer's protocol. Cells were seeded at the density of 3000 cells/cm2 (for growth in STD medium) and 9000 cells/cm2 (for growth in –GLN+AKG+NEAA medium) in 150-mm dishes in STD medium and incubated overnight at 37°C and 5% CO2. After 18 h, cells were washed twice with PBS and incubated for 54 h in STD or –GLN+AKG+NEAA media. The day of the analysis, cells were lysed with a mixture of chloroform:isopropanol:NP-40 (7:11:0.1) and samples were processed according to the datasheet instructions. Finally, cholesterol levels were assayed by reading the absorbance of the samples at 570 nm and comparing it with cholesterol standard curve.

5.5.10 Lipid content (Nile Red staining)

The neutral lipid dye Nile Red (9-diethylamino-5H-benzo[α]phenoxazine-5-one) was used for lipid staining. The stock solution (1.0 mg/ml) in methanol was stored frozen (−20°C) in dark. Staining was carried out on live cells by adding the dye to a final concentration of 10 ng/ml directly in the culture medium for 5 minutes. Then, the dye was carefully washed out using PBS prior to microscopy. Lipid droplets were then visualized with confocal microscope (Nikon Eclipse Ti-E; 60X magnification) by exciting with FITC (green fluorescence) and AlexaFluor488 (red fluorescence) channels. Total fluorescence (i.e. green+red) per

cell was determined by analysing photos with ImageJ software: regions of interest (ROIs) corresponding to each cell were drawn on brightfield images, then ROIs were superimposed on photos acquired by exciting both with green and red fluorescence. Then, the corrected total cell fluorescence (CTCF) –normalized on cell area– was calculated, after subtracting the mean fluorescence of the background readings, by summing the corrected green and red fluorescence.

5.5.11 RNA extraction and transcriptomic analysis

Cells were plated at the density of 3000 cells/cm2 in standard medium and incubated overnight at 37°C and 5% CO2. After 18 h, cells were washed twice with PBS and incubated for 54 h in STD medium or for 144 h in medium without glutamine (Invitrogen Inc., Carlsbad, CA, USA) supplemented with dimethyl-2-oxoglutarate (AKG, 4 mM, Sigma Aldrich Inc.) and nonessential amino acids (Pro, Ala, Asp, Asn, 4 mM each, Sigma Aldrich Inc.). RNA was then extracted from cells by using TriFastTM reagent (EuroGOLD) and generated triplicate samples were stored at -80°C until the analysis. The QC evaluation was performed using Nanodrop and Agilent 2100 Bioanalyzer. Single strand biotinylated cDNA was generated from 200 ng of total RNA using two cycles of cDNA synthesis with the Affymetrix WT PLUS expression Kit. The first cycle-first strand synthesis was performed using an engineered set of random primers that excluded rRNA-matching sequences and included the T7 promoter sequences. After second-strand synthesis, the resulting

cDNA was in vitro transcribed with the T7 RNA polymerase to generate a cRNA. This cRNA was subjected to a second cycle-first strand synthesis in the presence of dUTP in a fixed ratio relative to dTTP. Single strand cDNA was then purified and fragmented with a mixture of uracil DNA glycosylase and apurinic/apirimidinic endonuclease 1 (Affymetrix) in correspondence of incorporated dUTPs. DNA fragments were then terminally labelled by terminal deoxynucleotidyl transferase (Affymetrix) with biotin. The biotinylated cDNA was hybridized to the Clariom D Arrays (previously known as Mouse GeneChip MTA 1.0 Arrays) containing more than 214000 full-length transcripts. After the hybridization, chips were washed and scanned on the Affymetrix Complete GeneChip® Instrument System, generating digitized image data (DAT) files and CEL files. CEL files were analyzed by R Bioconductor Oligo and Limma Packages, respectively. The full dataset was normalized by using the Robust Multialignment Algorithm (RMA). Results were filtered for a Fold Change ≥ 1.5. The genes were classified as Differentially Expressed if showed a FDR corrected p-value ≤ 0.05.

5.5.12 Reporter metabolites

Transcriptomic data were mapped on the corresponding enzymes of a genome scale metabolic model adding the p value obtained from a Student's t-test as a specification of the significance of differential gene expression (and so of the change for each enzyme). Each pi was then converted to a Z score of the enzyme

node (Zni) connected to the enzyme under investigation, by using the inverse normal cumulative distribution (θ–1).

$Zni = \theta{-}1\ (1\text{-}pi)$

Thus, each metabolite node in the genome-wide metabolic model (GWMM) was scored based on the normalized transcriptional response of its neighboring enzymes. Dealing with differential data, the normalized transcriptional response has been calculated as size-independent aggregated Z scores of the k neighboring enzymes.

$Z\ metabolite = (1/\sqrt{k}) \sum Zni$

The scoring used to identify reporter metabolites was a test for the null hypothesis "neighbor enzymes of a metabolite in the metabolic graph show the observed normalized transcriptional response by chance". Metabolites with the highest score are defined as reporter metabolites, namely those metabolites around which transcriptional changes occur.

To perform the analyses, the Cobra Toolbox function "reporterMets" was used, which implements under Matlab the reporter metabolites algorithm by Patil and Nielsen [30]. Regarding the input, the Recon 2.2 model [31] was used.

5.5.13 Metabolomic analyses

For metabolite extraction, NIH-RAS cells that had to be grown in STD medium were plated at 3000 cells/cm2, while NIH-RAS cells that had to be grown in –GLN+AKG+NEAA medium were plated at 9000 cells/cm2 –in order to reach the same cell density after 54 h– in 6-well plates with normal growth medium (STD). After 18

h at 37°C and 5% CO2, cells were rinsed twice with PBS and incubated for 54 h in STD medium or –GLN+AKG+NEAA medium. After 54 h from medium change, cells were quickly rinsed with NaCl 0.9% and quenched with 0.4 ml ice-cold methanol. An equal volume of water was added, and cells were collected by scraping with a pipette tip. Cells were sonicated 5 seconds for 5 pulses at 70% power three times. One volume of chloroform was added, and cells were vortexed at 4°C for 20 min. Samples were centrifuged at 12000 g for 10 min, and the aqueous phase was collected in a new tube and evaporated under airflow at 37°C. Dried polar metabolites were dissolved in 60 µl of 2% methoxyamine hydrochloride in pyridine (Pierce) and held at 40°C for 6 h. After dissolution and reaction, 90 µl of MSTFA (N-Methyl-N-(trimethylsilyl) trifluoroacetamid) was added and samples were incubated at 60°C for 1 h. For cell culture, GC/MS analysis was performed using 6890 GC system combined with 5975BMS system (Agilent Technologies) equipped with a 30-m DB-5MS capillary column operating under electron impact (EI) ionization at 70eV. 1 µl of sample was injected in splitless mode at 250°C, using helium as the carrier gas at a flow rate of 1 ml/min. The GC oven temperature was held at 70°C for 2 min and increased to 325°C at 10°C/min. GC/MS data processing was performed using Agilent MassHunter software and statistical analyses were performed using Mass Profile Professional (MPP) software [32]. Relative metabolites abundance was carried out after normalization to internal standard norvaline and cell number.

5.5.14 ^{13}C tracer analyses

All labelling experiments were performed in media with 10% dialyzed newborn calf serum (NCS) for 54 h. All tracers were purchased from Sigma-Aldrich. For metabolite extraction, NIH-RAS cells that had to be grown in STD medium were plated at 3000 cells/cm2, while NIH-RAS cells that had to be grown in –GLN+AKG+NEAA medium were plated at 9000 cells/cm2 –in order to reach the same cell density after 54 h– in 6-well plates with normal growth medium (STD). After 18 h at 37°C and 5% CO2, cells were rinsed twice with PBS and medium change was done, by incubating cells for 54 h with STD or –GLN+AKG+NEAA media containing dialyzed NCS and the proper tracer [U-$^{13}C_6$]-Glucose, [U-$^{13}C_5$]-glutamine, [1-^{13}C]-glutamate, [^{15}N]-aspartate or [^{15}N]-asparagine). Labelled cell cultures were then washed with 0.9% NaCl and metabolism was quenched in liquid nitrogen and then with -20°C cold 70% methanol. After cell scraping in 70% methanol (containing internal standards norvaline and glutarate), -20°C cold chloroform was added and the samples were vortexed at 4°C to extract metabolites. Phase separation was achieved by centrifugation at 4°C. The methanol-water phase containing polar metabolites was separated and dried using a vacuum concentrator. Dried metabolite samples were stored at −80 °C.

Polar metabolites were derivatized for 90 min at 37 °C with 7.5 µl of 20 mg/ml methoxyamine in pyridine and subsequently for 60 min at 60°C with 15 µl of N-(tert-butyldimethylsilyl)-N-methyl-trifluoroacetamide, with 1% tert-butyldimethylchlorosilane [33]

(Sigma-Aldrich). Mass distributions and metabolite concentrations were measured with a 7890A GC system (Agilent Technologies) combined with a 5975C Inert MS system (Agilent Technologies). 1 µl of sample was injected into a DB35MS column in splitless mode using an inlet temperature of 270°C. The carrier gas was helium with a flow rate of 1 ml/min. Upon injection, the GC oven was held at 100°C for 3 min and then ramped to 300°C with a gradient of 2.5°C/min followed by a 5 min after run at 320°C. The MS system was operated under electron impact ionization at 70 eV and a mass range of 100–650 amu was scanned. Mass distributions were extracted from the raw ion chromatograms using a custom Matlab M-file [34]. Mass spectra were corrected for naturally occurring isotopes [35] and for potential metabolite contamination in a blank extraction. All labelling fractions were transformed to a natural abundance corrected mass distribution vector (MDV) [36]. Metabolite levels were determined based on the internal standards norvaline and glutarate, and protein content determined with Pierce™ BCA Protein Assay Kit (Thermo Fisher Scientific) to normalize metabolomics data.

5.5.16 ENGRO metabolic network reconstruction

A metabolic network designed to evaluate the contribution of glucose and glutamine to biomass formation was extracted from the HMR [37] and Recon 2 [38] databases and manually curated. It includes central metabolic pathways and the connected

production of building blocks for lipids and protein biosynthesis, together accounting for 80% of the dry cellular biomass [38]. To streamline the analysis of ENGRO emergent properties, unless strictly required by reaction thermodynamics, all metabolites are assumed in the same compartment and linear pathways are lumped into a single reaction. The obtained model is structurally free from thermodynamically infeasible loops, which is a major problem in genome-wide models [39].

5.5.17 Flux Balance Analysis (FBA)

FBA requires a stoichiometric matrix S and a set of constraints that impose the upper and lower bound of fluxes. The steady state constraint is defined by the equation dx⁄(dt=S·v=0), where dx/dt are time derivatives of metabolite concentrations represented by the product of the m×n matrix S times the vector of fluxes v=(v_1,v_2, ⟦…,v⟧ _n), where vi is the flux of reaction i, n is the number of reactions, and m is the number of metabolites. The ensemble of functional states that the system can reach given a boundary condition I determines the feasible solutions space Φ=Σ∩I. By exploiting linear programming, FBA allows for optimization of the flux through a weighted sum of fluxes. In particular, the COBRA Toolbox [40] and the GLPK solver were used.

5.6 REFERENCES

1. Mizock BA (2010) Immunonutrition and critical illness: an update. Nutrition 26: 701-707.

2. Lacey JM, Wilmore DW (1990) Is glutamine a conditionally essential amino acid? Nutrition reviews 48: 297-309.

3. Yuneva M, Zamboni N, Oefner P, Sachidanandam R, Lazebnik Y (2007) Deficiency in glutamine but not glucose induces MYC-dependent apoptosis in human cells. The Journal of cell biology 178: 93-105.

4. Altman BJ, Stine ZE, Dang CV (2016) From Krebs to clinic: glutamine metabolism to cancer therapy. Nature reviews Cancer 16: 619-634.

5. Meng M, Chen S, Lao T, Liang D, Sang N (2010) Nitrogen anabolism underlies the importance of glutaminolysis in proliferating cells. Cell cycle 9: 3921-3932.

6. Mullen et al. 2012 Reductive carboxylation supports growth in tumours with defective mitochondria. Nature 481(7381): 385–388

7. Cohen A, Hall MN (2009) An amino acid shuffle activates mTORC1. Cell 136: 399-400.

8. Nicklin P, Bergman P, Zhang B, Triantafellow E, Wang H, et al. (2009) Bidirectional transport of amino acids regulates mTOR and autophagy. Cell 136: 521-534.

9. Duran RV, Oppliger W, Robitaille AM, Heiserich L, Skendaj R, et al. (2012) Glutaminolysis activates Rag-mTORC1 signalling. Molecular cell 47: 349-358.

10. Magnuson B, Ekim B, Fingar DC (2012) Regulation and function of ribosomal protein S6 kinase (S6K) within mTOR signalling networks. Biochemical Journal 441 (1): 1–21.

11. Zheng L, Zhang W, Zhou Y, Li F, Wei H, et al. (2016) Recent Advances in Understanding Amino Acid Sensing Mechanisms that Regulate mTORC1. International journal of molecular sciences 17.

12. Sacco E, Metalli D, Spinelli M, Manzoni R, Samalikova M, et al. (2012) Novel RasGRF1-derived Tat-fused peptides inhibiting Ras-dependent proliferation and migration in mouse and human cancer cells. Biotechnology advances 30: 233-243.

13. Bossu P, Vanoni M, Wanke V, Cesaroni MP, Tropea F, et al. (2000) A dominant negative RAS-specific guanine nucleotide exchange factor reverses neoplastic phenotype in K-ras transformed mouse fibroblasts. Oncogene 19: 2147-2154.

14. Chiaradonna F, Sacco E, Manzoni R, Giorgio M, Vanoni M, et al. (2006) Ras-dependent carbon metabolism and transformation in mouse fibroblasts. Oncogene 25: 5391-5404.

15. Gaglio D, Soldati C, Vanoni M, Alberghina L, Chiaradonna F (2009) Glutamine deprivation induces abortive s-phase rescued by deoxyribonucleotides in k-ras transformed fibroblasts. PloS one 4: e4715.

16. Eagle H, Oyama VI, Levy M, Horton CL, Fleischman R (1956) The growth response of mammalian cells in tissue culture to L-glutamine and L-glutamic acid. The Journal of biological chemistry 218: 607-616.

17. Tardito S, Oudin A, Ahmed SU, Fack F, Keunen O, et al. (2015) Glutamine synthetase activity fuels nucleotide biosynthesis and supports growth of glutamine-restricted glioblastoma. Nature cell biology 17: 1556-1568.

18. Gaglio D, Valtorta S, Ripamonti M, Bonanomi M, Damiani C, et al. (2016) Divergent in vitro/in vivo responses to drug treatments of highly aggressive NIH-Ras cancer cells: a PET imaging and metabolomics-mass-spectrometry study. Oncotarget.

19. Son J, Lyssiotis CA, Ying H, Wang X, Hua S, et al. (2013) Glutamine supports pancreatic cancer growth through a KRAS-regulated metabolic pathway. Nature 496: 101-105.

20. Lu SC (2009) Regulation of glutathione synthesis. Molecular aspects of medicine 30: 42-59.

21. Gaglio D, Metallo CM, Gameiro PA, Hiller K, Danna LS, et al. (2011) Oncogenic K-Ras decouples glucose and glutamine metabolism to support cancer cell growth. Molecular systems biology 7: 523.

22. Damiani C, Colombo R, Gaglio D, Mastroianni F, Pescini D, et al. (2017) A metabolic core model elucidates how enhanced utilization of glucose and glutamine, with enhanced glutamine-dependent lactate production, promotes cancer cell growth: The WarburQ effect. PLoS Computational Biology 13(9): e1005758.

23. Rahman I, Kode A, Biswas SK (2006) Assay for quantitative determination of glutathione and glutathione disulfide levels using enzymatic recycling method. Nature protocols 1: 3159-3165.

24. Csibi A, Fendt SM, Li C, Poulogiannis G, Choo AY, et al. (2013) The mTORC1 pathway stimulates glutamine metabolism and cell proliferation by repressing SIRT4. Cell 153: 840-854.

25. Duvel K, Yecies JL, Menon S, Raman P, Lipovsky AI, et al. (2010) Activation of a metabolic gene regulatory network downstream of mTOR complex 1. Molecular cell 39: 171-183.

26. Peterson TR, Sengupta SS, Harris TE, Carmack AE, Kang SA, et al. (2011) mTOR complex 1 regulates lipin 1 localization to control the SREBP pathway. Cell 146: 408-420.26.

27. Alberghina L and Gaglio D (2014) Redox control of glutamine utilization in cancer. Cell Death and Disease 5,e1561.

28. Bradford MM (1976) A rapid and sensitive method for the quantitation of microgram quantities of protein utilizing the principle of protein-dye binding. Analytical biochemistry 72: 248-254.

29. Taylor SJ, Shalloway D (1996) Cell cycle-dependent activation of Ras. Current biology : CB 6: 1621-1627.

30. Patil KR, Nielsen J (2005) Uncovering transcriptional regulation of metabolism by using metabolic network topology. Proceedings of the National Academy of Sciences of the United States of America 102: 2685-2689.

31. Swainston N, Smallbone K, Hefzi H, Dobson PD, Brewer J, et al. (2016) Recon 2.2: from reconstruction to model of human metabolism. Metabolomics : Official journal of the Metabolomic Society 12: 109.

32. Musharraf SG, Mazhar S, Choudhary MI, Rizi N, Atta ur R (2015) Plasma metabolite profiling and chemometric analyses of lung cancer along with three controls through gas chromatography-mass spectrometry. Scientific reports 5: 8607.

33. Fendt SM, Bell EL, Keibler MA, Davidson SM, Wirth GJ, et al. (2013) Metformin decreases glucose oxidation and increases the dependency of prostate cancer cells on reductive glutamine metabolism. Cancer research 73: 4429-4438.

34. Young JD, Walther JL, Antoniewicz MR, Yoo H, Stephanopoulos G (2008) An elementary metabolite unit (EMU) based method of isotopically nonstationary flux analysis. Biotechnology and bioengineering 99: 686-699.

35. Fernandez CA, Des Rosiers C, Previs SF, David F, Brunengraber H (1996) Correction of ^{13}C mass isotopomer distributions for natural stable isotope abundance. Journal of mass spectrometry : JMS 31: 255-262.

36. Buescher JM, Antoniewicz MR, Boros LG, Burgess SC, Brunengraber H, et al. (2015) A roadmap for interpreting (^{13})C metabolite labelling patterns from cells. Current opinion in biotechnology 34: 189-201.

37. Mardinoglu A, Agren R, Kampf C, Asplund A, Nookaew I, et al. (2013) Integration of clinical data with a genome-scale metabolic model of the human adipocyte. Mol Syst Biol 9: 649.

38. Thiele I, Swainston N, Fleming RM, Hoppe A, Sahoo S, et al. (2013) A community-driven global reconstruction of human metabolism. Nat Biotechnol 31: 419-425.

39. De Martino D, Capuani F, Mori M, De Martino A, Marinari E (2013) Counting and correcting thermodynamically infeasible flux cycles in genome-scale metabolic networks. Metabolites 3: 946-966.

40. Schellenberger J, Que R, Fleming RM, Thiele I, Orth JD, et al. (2011) Quantitative prediction of cellular metabolism with constraint-based models: the COBRA Toolbox v2.0. Nat Protoc 6: 1290-1307.

6. GENERAL DISCUSSION

Cancer is a 16th century disease now posing as a 21st century epidemic which urgently requires futuristic solutions. Even though massive cancer genome projects have greatly expanded our knowledge about cancer, we still are far from finding a reliable and effective therapy for treatment of cancer patients. The evolution of cancer cells under therapeutic pressure rendering the ability to evade drug effects has been a real bottle neck for cancer researchers in their efforts to develop better and efficacious therapy. Inter and intra tumour genomic/epigenomic heterogeneity further adds to this complexity in clinical practice (Stanta and Bonin, 2018). Despite this vast genomic heterogeneity among tumours, majority of the cancers invoke similar metabolic pathways to survive and maintain their proliferative nature (Coller, 2014). This feature of cancer cells has boggled scientist and hence, has sparked the renewed interest in understanding cellular metabolism for cancer therapeutics.

Through recent scientific efforts, it has become clearly evident the vast influence metabolic rewiring plays in driving tumorigenesis of cancer cells, and also in rendering the ability to evade therapeutic pressure. Thus, a systems level investigation of cancer metabolism should be of utmost importance in our current and future medical regime in devising a therapeutic strategy for the treatment of cancer patients. Understanding the metabolic demands of cancer cells would help us in developing much more better and efficacious therapy customized based on the patient's predicted pharmacodynamics response.

Metabolic therapy have experienced failures in the past because of lack of clear understanding about metabolic rewiring engaged by cancer cells, as upon targeting with one metabolic inhibitor, cancer cells can still rewire their metabolism and switch to alternate mechanism for their survival. Thus in chapter 1, we highlighted the role of two inhibitors targeting glucose and glutamine metabolism. We dissected the role of these inhibitors on the proliferation and growth of lung and colon cancer cell lines individually as well as a combination therapy. Not only had we identified the metabolic differences between K-ras driven lung and colon cancer but also the differences in metabolic response to inhibition of one or the other pathway. Targeting the most predominantly used metabolic pathways identified by cancer cells i.e glucose or glutamine metabolism, we showed that tumour growth can be strictly inhibited *in-vitro* as well *in-vivo* using a combinatorial approach. Though targeting by just BKM120 or CB-839 do show interesting results in restricting cancer proliferation, cancer cells are still able to survive by switching their metabolism to the alternate source. Thus, restricting cancer metabolic rewiring by targeting at two vital chokepoints could be a promising approach in treatment of K-ras driven cancers as it renders cancer cells constricted in terms of their options to switch metabolic pathways required to sustain growth.

This study also highlighted alternative mechanism activated by cancer cells in order to sustain survival by means of PPP, amino sugar and nucleotide metabolism, which further contributes in

expanding our current understanding about cancer cell metabolism. Drug toxicity has always been a concern when developing a chemotherapeutic strategy, but here we showed that combinatorial treatment of cancer cells with metabolic inhibitors BKM120 and CB-839 showed minimal to no toxicity when tested in mice further substantiating its relevance to be used in clinical setting.

Metabolomics approach can not only be used to understand oncogenic influence on tumorigenesis, but also understand the influence of drug treatment and eventual development of drug resistance, which is a major challenge today in cancer therapeutics. Chapter 2 sheds light in the metabolic rewiring engaged by cancer cells in order to survive and become resistant to endocrine therapeutic drugs vastly used in treatment of ER+ breast cancer.

Using metabolomics, fluxomics and computational modelling approach we showcased the drug dependent differential metabolic rewiring of pathways in development of resistance to endocrine therapeutic drugs. Glutamine metabolism was found as a focal regulatory pathway which seemed to rescue cancer cells upon drug treatment and eventually leading development into resistant phenotype. Systems level investigation of the metabolism revealed vast differences in metabolism of resistant and sensitive cell lines, and helped identify putative targets which could be exploited for use against resistant tumours.

We identified reductive carboxylation of glutamine as a key mechanism in resistant cell lines which allowed for increased lipid and cholesterol synthesis driving growth and proliferation of resistant cells.

The use of metformin has been highly debatable as an adjuvant to cancer therapy (Camacho et al., 2015). But it is very important to understand the metabolic phenotype of cancer cells in order for metformin to be efficacious in clinical setting. We showcased that aromatase inhibitor resistance lead to increased OXPHOS and increased mitochondrial function thus making it a suitable target for treatment via metformin. Upon treatment with metformin, we observed remarkable results in inhibiting cancer cell proliferation and growth of AI resistant cells. Thus understanding of metabolic phenotype makes choosing appropriate adjuvants for cancer therapy more relevant and easier.

Finally, in chapter 3 we dived into exploiting the role of glutamine and its contribution in growth and proliferation of cancer cells. Glutamine being the most abundant amino acid in human serum plays an important role not only as a nitrogen source, but also as a carbon source fuelling TCA cycle. To assess the importance of glutamine in growth of K-Ras transformed NIH3T3 cell lines we substituted glutamine with its constituents, aKG and ammonium, provided as NEAA. Our results confirm the role of glutamine in supporting the Warburg effect in hyperglycolytic cancer cells. Growth in AKG+NEAA induces a large metabolic rearrangement that includes decreased accumulation of lipids – linked to a drop

in AKG reverse carboxylation - and NADPH, a decrease in fermentation and up-regulation of respiration (reverse Warburg effect). These rearrangements lead to a slow growth phenotype. The major role of metabolic rewiring in the ensuing slow growth of NIH-RAS cell in AKG+NEA medium was confirmed by FBA computational experiments.

So through the three chapters of the thesis, we not only highlighted the role metabolism in fuelling growth and proliferation of cancer cells, but also on how cancer metabolic rewiring aids in driving resistance to ET, while also shedding light on the role of glutamine in cancer metabolism. We showed how targeting metabolic chokepoints can prevent cancer metabolic rewiring, and how proper understanding of cancer metabolism is crucial for formulating a treatment strategy along with determining the proper choice of adjuvants.

Though further investigations are needed to properly understand the relevance and harness the full potential of these findings in the treatment of cancer patients, this thesis does contribute towards expanding our current understanding about cancer cell metabolism in order to design personalised therapies of tomorrow.

7. ACKNOWLEDGEMENTS

I am extremely thankful, foremost to Prof. Marco Vanoni, for giving me this great opportunity to further my career as a PhD student in his laboratory. Through these three years, I was allowed to pursue openly and freely my scientific interests and I am highly grateful for this. During these three years, he has been very supportive and helped inculcate in me the scientific curiosity required to be a good researcher.

I am very grateful to Prof. Lilia Alberghina, who has been my supervisor for the project and has always pushed me towards being a better scientist. She has kept me motivated with her ideas and her visions about science for the community.

I would like to thank Dr. Daniela Gaglio who taught me a lot about mass spectrometry and metabolomics, and this project would not have been possible without her technical guidance and mentoring.

I am very thankful to all the members of Epipredict.eu consortium, especially Dr. Pernette Verschure, Prof. Hans V. Westerhoff, Prof. Stefan Weimann, & Dr. Luca Magnani for their constant guidance.

A huge thanks to the lab members of the SYSBIO.IT family. Marcella Bonanomi, Elisabetta Napodano, Genesio Di Muro, Guiseppina Votta, Gloria Campioni, & Nicole Righi

Finally I would like to thank all my friends, and specially my parents for being with me through thick and thin.

8. REFERENCES

Albert, M., and Helin, K. (2010). Histone methyltransferases in cancer. Semin. Cell Dev. Biol. *21*, 209–220.

Almac, E., and Ince, C. (2007). The impact of storage on red cell function in blood transfusion. Best Pract. Res. Clin. Anaesthesiol. *21*, 195–208.

Antoniewicz, M.R. (2018). A guide to 13C metabolic flux analysis for the cancer biologist. Exp. Mol. Med. *50*, 19.

Antoniewicz, M.R., Kelleher, J.K., and Stephanopoulos, G. (2007). Elementary metabolite units (EMU): A novel framework for modeling isotopic distributions. Metab. Eng. *9*, 68–86.

Auslander, N., Yizhak, K., Weinstock, A., Budhu, A., Tang, W., Wang, X.W., Ambs, S., and Ruppin, E. (2016). A joint analysis of transcriptomic and metabolomic data uncovers enhanced enzyme-metabolite coupling in breast cancer. Sci. Rep. *6*, 29662.

Avery, O.T. (1944). STUDIES ON THE CHEMICAL NATURE OF THE SUBSTANCE INDUCING TRANSFORMATION OF PNEUMOCOCCAL TYPES: INDUCTION OF TRANSFORMATION BY A DESOXYRIBONUCLEIC ACID FRACTION ISOLATED FROM PNEUMOCOCCUS TYPE III. J. Exp. Med. *79*, 137–158.

Baker, S.G., and Kramer, B.S. (2007). Paradoxes in carcinogenesis: New opportunities for research directions. BMC Cancer *7*, 151.

Ballantyne, C.M., Davidson, M.H., MacDougall, D.E., Bays, H.E., DiCarlo, L.A., Rosenberg, N.L., Margulies, J., and Newton, R.S. (2013). Efficacy and Safety of a Novel Dual Modulator of Adenosine Triphosphate-Citrate Lyase and Adenosine Monophosphate-Activated Protein Kinase in Patients With Hypercholesterolemia. J. Am. Coll. Cardiol. *62*, 1154–1162.

Baysal, B.E. (2000). Mutations in SDHD, a Mitochondrial Complex II Gene, in Hereditary Paraganglioma. Science (80-.). *287*, 848–851.

Benz, M.R., Herrmann, K., Walter, F., Garon, E.B., Reckamp, K.L., Figlin, R.,

Phelps, M.E., Weber, W.A., Czernin, J., and Allen-Auerbach, M.S. (2011). 18F-FDG PET/CT for Monitoring Treatment Responses to the Epidermal Growth Factor Receptor Inhibitor Erlotinib. J. Nucl. Med. *52*, 1684–1689.

Berwick, D.C., Hers, I., Heesom, K.J., Moule, S.K., and Tavaré, J.M. (2002). The Identification of ATP-citrate Lyase as a Protein Kinase B (Akt) Substrate in Primary Adipocytes. J. Biol. Chem. *277*, 33895–33900.

Bister, K., and Duesberg, P.H. (1979). Structure and specific sequences of avian erythroblastosis virus RNA: Evidence for multiple classes of transforming genes among avian tumor viruses. Proc. Natl. Acad. Sci. *76*, 5023–5027.

Bjarnadottir, O., Romero, Q., Bendahl, P.-O., Jirström, K., Rydén, L., Loman, N., Uhlén, M., Johannesson, H., Rose, C., Grabau, D., et al. (2013). Targeting HMG-CoA reductase with statins in a window-of-opportunity breast cancer trial. Breast Cancer Res. Treat. *138*, 499–508.

Bonuccelli, G., Whitaker-Menezes, D., Castello-Cros, R., Pavlides, S., Pestell, R.G., Fatatis, A., Witkiewicz, A.K., Vander Heiden, M.G., Migneco, G., Chiavarina, B., et al. (2010). The reverse Warburg Effect: Glycolysis inhibitors prevent the tumor promoting effects of caveolin-1 deficient cancer associated fibroblasts. Cell Cycle *9*, 1960–1971.

Boroughs, L.K., and DeBerardinis, R.J. (2015). Metabolic pathways promoting cancer cell survival and growth. Nat. Cell Biol. *17*, 351–359.

Brunk, E., Sahoo, S., Zielinski, D.C., Altunkaya, A., Dräger, A., Mih, N., Gatto, F., Nilsson, A., Preciat Gonzalez, G.A., Aurich, M.K., et al. (2018). Recon3D enables a three-dimensional view of gene variation in human metabolism. Nat. Biotechnol. *36*, 272–281.

Cairns, R.A., Harris, I.S., and Mak, T.W. (2011). Regulation of cancer cell metabolism. Nat. Rev. Cancer *11*, 85–95.

Camacho, L., Dasgupta, A., and Jiralerspong, S. (2015). Metformin in breast cancer - an evolving mystery. Breast Cancer Res. *17*, 88.

Cantor, J.R., and Sabatini, D.M. (2012). Cancer Cell Metabolism: One Hallmark, Many Faces. Cancer Discov. *2*, 881–898.

Chang, H.W. (1997). Transformation of Chicken Cells by the Gene Encoding the Catalytic Subunit of PI 3-Kinase. Science (80-.). *276*, 1848–1850.

Chu, Q.S.-C., Sangha, R., Spratlin, J., J. Vos, L., Mackey, J.R., McEwan, A.J.B., Venner, P., and Michelakis, E.D. (2015). A phase I open-labeled, single-arm, dose-escalation, study of dichloroacetate (DCA) in patients with advanced solid tumors. Invest. New Drugs *33*, 603–610.

Coller, H.A. (2014). Is Cancer a Metabolic Disease? Am. J. Pathol. *184*, 4–17.

Comerford, S.A., Huang, Z., Du, X., Wang, Y., Cai, L., Witkiewicz, A.K., Walters, H., Tantawy, M.N., Fu, A., Manning, H.C., et al. (2014). Acetate Dependence of Tumors. Cell *159*, 1591–1602.

Cori, C.F., and G.T.Cori (1925). The carbohydrate metabolism of tumors. II. Changes in the sugar, lactic acid, and co-combining power of blood passing through a tumor. J. Biol. Chem. *65*, 397–405.

Damiani, C., Colombo, R., Gaglio, D., Mastroianni, F., Pescini, D., Westerhoff, H.V., Mauri, G., Vanoni, M., and Alberghina, L. (2017). A metabolic core model elucidates how enhanced utilization of glucose and glutamine, with enhanced glutamine-dependent lactate production, promotes cancer cell growth: The WarburQ effect. PLOS Comput. Biol. *13*, e1005758.

DeBerardinis, R.J. (2011). Serine Metabolism: Some Tumors Take the Road Less Traveled. Cell Metab. *14*, 285–286.

DeBerardinis, R.J., Mancuso, A., Daikhin, E., Nissim, I., Yudkoff, M., Wehrli, S., and Thompson, C.B. (2007). Beyond aerobic glycolysis: Transformed cells can engage in glutamine metabolism that exceeds the requirement for protein and nucleotide synthesis. Proc. Natl. Acad. Sci. *104*, 19345–19350.

DeWaal, D., Nogueira, V., Terry, A.R., Patra, K.C., Jeon, S.-M., Guzman, G., Au, J., Long, C.P., Antoniewicz, M.R., and Hay, N. (2018). Author Correction:

Hexokinase-2 depletion inhibits glycolysis and induces oxidative phosphorylation in hepatocellular carcinoma and sensitizes to metformin. Nat. Commun. *9*, 2539.

Diaz-Moralli, S., Aguilar, E., Marin, S., Coy, J.F., Dewerchin, M., Antoniewicz, M.R., Meca-Cortés, O., Notebaert, L., Ghesquière, B., Eelen, G., et al. (2016). A key role for transketolase-like 1 in tumor metabolic reprogramming. Oncotarget *7*, 51875–51897.

Doonan, F., Groeger, G., and Cotter, T.G. (2012). Preventing retinal apoptosis — Is there a common therapeutic theme? Exp. Cell Res. *318*, 1278–1284.

Duesberg, P.H., Bister, K., and Vogt, P.K. (1977). The RNA of avian acute leukemia virus MC29. Proc. Natl. Acad. Sci. *74*, 4320–4324.

Dunn, W.B., Bailey, N.J.C., and Johnson, H.E. (2005). Measuring the metabolome: current analytical technologies. Analyst *130*, 606.

Eagle, H. (2007). American Association for the Advancement of Science. In Hawley's Condensed Chemical Dictionary, (Hoboken, NJ, USA: John Wiley & Sons, Inc.), p. 501–14.

Esteller, M. (2000). Promoter Hypermethylation and BRCA1 Inactivation in Sporadic Breast and Ovarian Tumors. J. Natl. Cancer Inst. *92*, 564–569.

Etchegaray, J.-P., and Mostoslavsky, R. (2016). Interplay between Metabolism and Epigenetics: A Nuclear Adaptation to Environmental Changes. Mol. Cell *62*, 695–711.

Fantin, V.R., St-Pierre, J., and Leder, P. (2006). Attenuation of LDH-A expression uncovers a link between glycolysis, mitochondrial physiology, and tumor maintenance. Cancer Cell *9*, 425–434.

FARBER, S., CUTLER, E.C., HAWKINS, J.W., HARRISON, J.H., PEIRCE, E.C., and LENZ, G.G. (1947). The Action of Pteroylglutamic Conjugates on Man. Science (80-.). *106*, 619–621.

Feinberg, A.P., and Vogelstein, B. (1983). Hypomethylation distinguishes

genes of some human cancers from their normal counterparts. Nature *301*, 89–92.

Fernandez, H.R., Gadre, S.M., Tan, M., Graham, G.T., Mosaoa, R., Ongkeko, M.S., Kim, K.A., Riggins, R.B., Parasido, E., Petrini, I., et al. (2018). The mitochondrial citrate carrier, SLC25A1, drives stemness and therapy resistance in non-small cell lung cancer. Cell Death Differ. *25*, 1239–1258.

Finkel, T. (2011). Signal transduction by reactive oxygen species. J. Cell Biol. *194*, 7–15.

Fojo, T., and Parkinson, D.R. (2010). Biologically Targeted Cancer Therapy and Marginal Benefits: Are We Making Too Much of Too Little or Are We Achieving Too Little by Giving Too Much? Clin. Cancer Res. *16*, 5972–5980.

Gao, P., Tchernyshyov, I., Chang, T.-C., Lee, Y.-S., Kita, K., Ochi, T., Zeller, K.I., De Marzo, A.M., Van Eyk, J.E., Mendell, J.T., et al. (2009). c-Myc suppression of miR-23a/b enhances mitochondrial glutaminase expression and glutamine metabolism. Nature *458*, 762–765.

Gibbs, W.W. (2003). Untangling the roots of cancer. Sci. Am. *289*, 56–65.

Greger, V., Passarge, E., H�pping, W., Messmer, E., and Horsthemke, B. (1989). Epigenetic changes may contribute to the formation and spontaneous regression of retinoblastoma. Hum. Genet. *83*, 155–158.

Griffiths, W.J., Koal, T., Wang, Y., Kohl, M., Enot, D.P., and Deigner, H.-P. (2010). Targeted Metabolomics for Biomarker Discovery. Angew. Chemie Int. Ed. *49*, 5426–5445.

GUPPY, M., GREINER, E., and BRAND, K. (1993). The role of the Crabtree effect and an endogenous fuel in the energy metabolism of resting and proliferating thymocytes. Eur. J. Biochem. *212*, 95–99.

Gutierrez, M.J., Rosenberg, N.L., MacDougall, D.E., Hanselman, J.C., Margulies, J.R., Strange, P., Milad, M.A., McBride, S.J., and Newton, R.S. (2014). Efficacy and Safety of ETC-1002, a Novel Investigational Low-Density

Lipoprotein-Cholesterol–Lowering Therapy for the Treatment of Patients With Hypercholesterolemia and Type 2 Diabetes Mellitus. Arterioscler. Thromb. Vasc. Biol. *34*, 676–683.

Hanahan, D., and Weinberg, R.A. (2000). The hallmarks of cancer. Cell *100*, 57–70.

Hatada, I. (2010). The Epigenomics of Cancer. In An Omics Perspective on Cancer Research, (Dordrecht: Springer Netherlands), pp. 51–67.

Hershey, A.D. (1952). INDEPENDENT FUNCTIONS OF VIRAL PROTEIN AND NUCLEIC ACID IN GROWTH OF BACTERIOPHAGE. J. Gen. Physiol. *36*, 39–56.

Iagaru, A., Mittra, E., Yaghoubi, S.S., Dick, D.W., Quon, A., Goris, M.L., and Gambhir, S.S. (2009). Novel Strategy for a Cocktail 18F-Fluoride and 18F-FDG PET/CT Scan for Evaluation of Malignancy: Results of the Pilot-Phase Study. J. Nucl. Med. *50*, 501–505.

Jones, P.A., and Baylin, S.B. (2002). The fundamental role of epigenetic events in cancer. Nat. Rev. Genet. *3*, 415–428.

Jones, S., Anagnostou, V., Lytle, K., Parpart-Li, S., Nesselbush, M., Riley, D.R., Shukla, M., Chesnick, B., Kadan, M., Papp, E., et al. (2015). Personalized genomic analyses for cancer mutation discovery and interpretation. Sci. Transl. Med. *7*, 283ra53-283ra53.

Knudson, A.G. (1971). Mutation and cancer: statistical study of retinoblastoma. Proc. Natl. Acad. Sci. U. S. A. *68*, 820–823.

Kroemer, G., and Pouyssegur, J. (2008). Tumor Cell Metabolism: Cancer's Achilles' Heel. Cancer Cell *13*, 472–482.

Lai, I.-L., Chou, C.-C., Lai, P.-T., Fang, C.-S., Shirley, L.A., Yan, R., Mo, X., Bloomston, M., Kulp, S.K., Bekaii-Saab, T., et al. (2014). Targeting the Warburg effect with a novel glucose transporter inhibitor to overcome gemcitabine resistance in pancreatic cancer cells. Carcinogenesis *35*, 2203–

2213.

Lai, M.M.C., Hu, S.S.F., and Vogt, P.K. (1979). Avian erythroblastosis virus: transformation-specific sequences form a contiguous segment of 3.25 kb located in the middle of the 6-kb genome. Virology *97*, 366–377.

Lam, C.-W., and Law, C.-Y. (2014). Untargeted Mass Spectrometry-Based Metabolomic Profiling of Pleural Effusions: Fatty Acids as Novel Cancer Biomarkers for Malignant Pleural Effusions. J. Proteome Res. *13*, 4040–4046.

LANE, D.P., and CRAWFORD, L. V. (1979). T antigen is bound to a host protein in SY40-transformed cells. Nature *278*, 261–263.

Lewis, N.E., and Abdel-Haleem, A.M. (2013). The evolution of genome-scale models of cancer metabolism. Front. Physiol. *4*, doi: 10.3389/fphys.2013.00237.

Li, J.J., Wang, H., Tino, J.A., Robl, J.A., Herpin, T.F., Lawrence, R.M., Biller, S., Jamil, H., Ponticiello, R., Chen, L., et al. (2007). 2-Hydroxy-N-arylbenzenesulfonamides as ATP-citrate lyase inhibitors. Bioorg. Med. Chem. Lett. *17*, 3208–3211.

Loeb, L.A., Loeb, K.R., and Anderson, J.P. (2003). Multiple mutations and cancer. Proc. Natl. Acad. Sci. *100*, 776–781.

López-López, Á., López-Gonzálvez, Á., Barker-Tejeda, T.C., and Barbas, C. (2018). A review of validated biomarkers obtained through metabolomics. Expert Rev. Mol. Diagn. *18*, 557–575.

Lu, C., and Thompson, C.B. (2012). Metabolic Regulation of Epigenetics. Cell Metab. *16*, 9–17.

Makinoshima, H., Takita, M., Saruwatari, K., Umemura, S., Obata, Y., Ishii, G., Matsumoto, S., Sugiyama, E., Ochiai, A., Abe, R., et al. (2015). Signaling through the Phosphatidylinositol 3-Kinase (PI3K)/Mammalian Target of Rapamycin (mTOR) Axis Is Responsible for Aerobic Glycolysis mediated by Glucose Transporter in Epidermal Growth Factor Receptor (EGFR)-mutated

Lung Adenocarcinoma. J. Biol. Chem. *290*, 17495–17504.

Mannava, S., Grachtchouk, V., Wheeler, L.J., Im, M., Zhuang, D., Slavina, E.G., Mathews, C.K., Shewach, D.S., and Nikiforov, M.A. (2008). Direct role of nucleotide metabolism in C-MYC-dependent proliferation of melanoma cells. Cell Cycle *7*, 2392–2400.

Marjon, K., Cameron, M.J., Quang, P., Clasquin, M.F., Mandley, E., Kunii, K., McVay, M., Choe, S., Kernytsky, A., Gross, S., et al. (2016). MTAP Deletions in Cancer Create Vulnerability to Targeting of the MAT2A/PRMT5/RIOK1 Axis. Cell Rep. *15*, 574–587.

de Mas, I.M., Aguilar, E., Jayaraman, A., Polat, I.H., Martín-Bernabé, A., Bharat, R., Foguet, C., Milà, E., Papp, B., Centelles, J.J., et al. (2014). Cancer cell metabolism as new targets for novel designed therapies. Future Med. Chem. *6*, 1791–1810.

Mashima, T., Seimiya, H., and Tsuruo, T. (2009). De novo fatty-acid synthesis and related pathways as molecular targets for cancer therapy. Br. J. Cancer *100*, 1369–1372.

Mashimo, T., Pichumani, K., Vemireddy, V., Hatanpaa, K.J., Singh, D.K., Sirasanagandla, S., Nannepaga, S., Piccirillo, S.G., Kovacs, Z., Foong, C., et al. (2014). Acetate Is a Bioenergetic Substrate for Human Glioblastoma and Brain Metastases. Cell *159*, 1603–1614.

Mentch, S.J., Mehrmohamadi, M., Huang, L., Liu, X., Gupta, D., Mattocks, D., Gómez Padilla, P., Ables, G., Bamman, M.M., Thalacker-Mercer, A.E., et al. (2015). Histone Methylation Dynamics and Gene Regulation Occur through the Sensing of One-Carbon Metabolism. Cell Metab. *22*, 861–873.

Metallo, C.M., Gameiro, P.A., Bell, E.L., Mattaini, K.R., Yang, J., Hiller, K., Jewell, C.M., Johnson, Z.R., Irvine, D.J., Guarente, L., et al. (2012). Reductive glutamine metabolism by IDH1 mediates lipogenesis under hypoxia. Nature *481*, 380–384.

van der Mijn, J.C., Panka, D.J., Geissler, A.K., Verheul, H.M., and Mier, J.W. (2016). Novel drugs that target the metabolic reprogramming in renal cell cancer. Cancer Metab. *4*, 14.

Mullen, A.R., Wheaton, W.W., Jin, E.S., Chen, P.H., Sullivan, L.B., Cheng, T., Yang, Y., Linehan, W.M., Chandel, N.S., and Deberardinis, R.J. (2012). Reductive carboxylation supports growth in tumour cells with defective mitochondria. Nature *481*, 385–8.

Müller, J. (1838). Ueber den feinern Bau und die Formen der krankhaften Geschwülste. Reimer *178*, 209–216.

Nguyen, V.T.M., Barozzi, I., Faronato, M., Lombardo, Y., Steel, J.H., Patel, N., Darbre, P., Castellano, L., Győrffy, B., Woodley, L., et al. (2015). Differential epigenetic reprogramming in response to specific endocrine therapies promotes cholesterol biosynthesis and cellular invasion. Nat. Commun. *6*, 10044.

Özcan, E., and Çakır, T. (2016). Reconstructed Metabolic Network Models Predict Flux-Level Metabolic Reprogramming in Glioblastoma. Front. Neurosci. *10*, 156.

Patra, K.C., and Hay, N. (2014). The pentose phosphate pathway and cancer. Trends Biochem. Sci. *39*, 347–354.

Peyrot, W.J., Van der Auwera, S., Milaneschi, Y., Dolan, C. V., Madden, P.A.F., Sullivan, P.F., Strohmaier, J., Ripke, S., Rietschel, M., Nivard, M.G., et al. (2018). Does Childhood Trauma Moderate Polygenic Risk for Depression? A Meta-analysis of 5765 Subjects From the Psychiatric Genomics Consortium. Biol. Psychiatry *84*, 138–147.

Pinton, P., Giorgi, C., and Pandolfi, P.P. (2011). The role of PML in the control of apoptotic cell fate: a new key player at ER–mitochondria sites. Cell Death Differ. *18*, 1450–1456.

Porstmann, T., Griffiths, B., Chung, Y.-L., Delpuech, O., Griffiths, J.R., Downward, J., and Schulze, A. (2005). PKB/Akt induces transcription of

enzymes involved in cholesterol and fatty acid biosynthesis via activation of SREBP. Oncogene *24*, 6465–6481.

Pylayeva-Gupta, Y., Grabocka, E., and Bar-Sagi, D. (2011). RAS oncogenes: weaving a tumorigenic web. Nat. Rev. Cancer *11*, 761–774.

Rosell, R., Perez-Roca, L., Sanchez, J.J., Cobo, M., Moran, T., Chaib, I., Provencio, M., Domine, M., Sala, M.A., Jimenez, U., et al. (2009). Customized Treatment in Non-Small-Cell Lung Cancer Based on EGFR Mutations and BRCA1 mRNA Expression. PLoS One *4*, e5133.

Ryšlavá, H., Doubnerová, V., Kavan, D., and Vaněk, O. (2013). Effect of posttranslational modifications on enzyme function and assembly. J. Proteomics *92*, 80–109.

Sauer, L.A., Stayman, J.W., and Dauchy, R.T. (1982). Amino acid, glucose, and lactic acid utilization in vivo by rat tumors. Cancer Res. *42*, 4090–4097.

Schmidt, C.W. (2004). Metabolomics: What's happening downstream of DNA. Environ. Health Perspect. *112*, A410-5.

Schulze, A., and Harris, A.L. (2012). How cancer metabolism is tuned for proliferation and vulnerable to disruption. Nature *491*, 364–373.

Seligson, D.B., Horvath, S., McBrian, M.A., Mah, V., Yu, H., Tze, S., Wang, Q., Chia, D., Goodglick, L., and Kurdistani, S.K. (2009). Global Levels of Histone Modifications Predict Prognosis in Different Cancers. Am. J. Pathol. *174*, 1619–1628.

Shackleton, M., Quintana, E., Fearon, E.R., and Morrison, S.J. (2009). Heterogeneity in Cancer: Cancer Stem Cells versus Clonal Evolution. Cell *138*, 822–829.

Shah, S., Carriveau, W.J., Li, J., Campbell, S.L., Kopinski, P.K., Lim, H.-W., Daurio, N., Trefely, S., Won, K.-J., Wallace, D.C., et al. (2016). Targeting ACLY sensitizes castration-resistant prostate cancer cells to AR antagonism by impinging on an ACLY-AMPK-AR feedback mechanism. Oncotarget *7*,

43713–43730.

Shih, T.Y., Weeks, M.O., Young, H.A., and Scolnick, E.M. (1979). Identification of a sarcoma virus-coded phosphoprotein in nonproducer cells transformed by Kirsten or Harvey murine sarcoma virus. Virology *96*, 64–79.

Sonnenschein, C., and Soto, A.M. (2000). Somatic mutation theory of carcinogenesis: Why it should be dropped and replaced. Mol. Carcinog. *29*, 205–211.

Sosa, V., Moliné, T., Somoza, R., Paciucci, R., Kondoh, H., and LLeonart, M.E. (2013). Oxidative stress and cancer: An overview. Ageing Res. Rev. *12*, 376–390.

Soto, A.M., and Sonnenschein, C. (2004). The somatic mutation theory of cancer: growing problems with the paradigm? BioEssays *26*, 1097–1107.

Stanta, G., and Bonin, S. (2018). Overview on Clinical Relevance of Intra-Tumor Heterogeneity. Front. Med. *5*, doi: 10.3389/fmed.2018.00085.

Swietach, P., Vaughan-Jones, R.D., and Harris, A.L. (2007). Regulation of tumor pH and the role of carbonic anhydrase 9. Cancer Metastasis Rev. *26*, 299–310.

Thiele, I., Swainston, N., Fleming, R.M.T., Hoppe, A., Sahoo, S., Aurich, M.K., Haraldsdottir, H., Mo, M.L., Rolfsson, O., Stobbe, M.D., et al. (2013). A community-driven global reconstruction of human metabolism. Nat. Biotechnol. *31*, 419–425.

Tomlinson, I.P.M., Alam, N.A., Rowan, A.J., Barclay, E., Jaeger, E.E.M., Kelsell, D., Leigh, I., Gorman, P., Lamlum, H., Rahman, S., et al. (2002). Germline mutations in FH predispose to dominantly inherited uterine fibroids, skin leiomyomata and papillary renal cell cancer. Nat. Genet. *30*, 406–410.

Vogelstein, B., and Kinzler, K.W. (1993). The multistep nature of cancer. Trends Genet. *9*, 138–141.

Vyas, S., Zaganjor, E., and Haigis, M.C. (2016). Mitochondria and Cancer. Cell

166, 555–566.

Wang, Q., Hardie, R.-A., Hoy, A.J., van Geldermalsen, M., Gao, D., Fazli, L., Sadowski, M.C., Balaban, S., Schreuder, M., Nagarajah, R., et al. (2015). Targeting ASCT2-mediated glutamine uptake blocks prostate cancer growth and tumour development. J. Pathol. *236*, 278–289.

Warburg, O. (1956). On the Origin of Cancer Cells. Science (80-.). *123*, 309–314.

Warburg, O., Wind, F., and Negelein, E. (1924). Über den Stoffwechsel der Tumoren (Original German article). Biochem. Z. *6*, 309–344.

Ward, P.S., and Thompson, C.B. (2012). Metabolic Reprogramming: A Cancer Hallmark Even Warburg Did Not Anticipate. Cancer Cell *21*, 297–308.

Wassermann, A., Keysser, F., and Wassermann, M. (1911). Beiträge zum Problem: Geschwülste von der Blutbahn aus therapeutisch zu beeinflussen. DMW - Dtsch. Medizinische Wochenschrift *37*, 2389–2391.

Watson, J. D., & Crick, F.H.C. (1953). A structure for deoxyribose nucleic acid. Nature *171*, 737–738.

Wellen, K.E., Hatzivassiliou, G., Sachdeva, U.M., Bui, T. V., Cross, J.R., and Thompson, C.B. (2009). ATP-Citrate Lyase Links Cellular Metabolism to Histone Acetylation. Science (80-.). *324*, 1076–1080.

Wise, D.R., and Thompson, C.B. (2010). Glutamine addiction: a new therapeutic target in cancer. Trends Biochem. Sci. *35*, 427–433.

Wise, D.R., DeBerardinis, R.J., Mancuso, A., Sayed, N., Zhang, X.-Y., Pfeiffer, H.K., Nissim, I., Daikhin, E., Yudkoff, M., McMahon, S.B., et al. (2008). Myc regulates a transcriptional program that stimulates mitochondrial glutaminolysis and leads to glutamine addiction. Proc. Natl. Acad. Sci. *105*, 18782–18787.

Xiao, M., Yang, H., Xu, W., Ma, S., Lin, H., Zhu, H., Liu, L., Liu, Y., Yang, C., Xu, Y., et al. (2012). Inhibition of -KG-dependent histone and DNA

demethylases by fumarate and succinate that are accumulated in mutations of FH and SDH tumor suppressors. Genes Dev. *26*, 1326–1338.

Xu, X., Meng, Y., Li, L., Xu, P., Wang, J., Li, Z., and Bian, J. (2018). Overview of the Development of Glutaminase Inhibitors: Achievements and Future Directions. J. Med. Chem. acs.jmedchem.8b00961.

Yang, M., and Vousden, K.H. (2016). Serine and one-carbon metabolism in cancer. Nat. Rev. Cancer *16*, 650–662.

Zaugg, K., Yao, Y., Reilly, P.T., Kannan, K., Kiarash, R., Mason, J., Huang, P., Sawyer, S.K., Fuerth, B., Faubert, B., et al. (2011). Carnitine palmitoyltransferase 1C promotes cell survival and tumor growth under conditions of metabolic stress. Genes Dev. *25*, 1041–1051.

Zhou, W., Liotta, L.A., and Petricoin, E.F. (2012). Cancer metabolism: What we can learn from proteomic analysis by mass spectrometry. Cancer Genomics and Proteomics *9*, 373–81.

Zhu, W., Ye, L., Zhang, J., Yu, P., Wang, H., Ye, Z., and Tian, J. (2016). PFK15, a Small Molecule Inhibitor of PFKFB3, Induces Cell Cycle Arrest, Apoptosis and Inhibits Invasion in Gastric Cancer. PLoS One *11*, e0163768.